THE HENRYK NIEWODNICZAŃSKI
INSTITUTE OF NUCLEAR PHYSICS
POLISH ACADEMY OF SCIENCES

Studies of Multi-Parton Interactions in Diffractive Processes with the ATLAS Forward Proton Detectors

Krzysztof Cieśla

Supervisor:
Prof. Dr. hab. Janusz J. Chwastowski

Co-supervisor:
Dr. Rafał Staszewski

Kraków, 2021

Abstract

This thesis is devoted to the study of the effects of Multi-Parton Interactions in diffractive events observed in proton-proton interactions at the Large Hadron Collider. Intact protons originating from such events were tagged and measured by dedicated forward detectors of the ATLAS experiment at the LHC – the AFP detectors. These detectors are installed in the LHC tunnel about 210 m from the interaction point. The analysis was performed using the data sample, corresponding to the integrated luminosity of 56 nb^{-1}, of proton-proton collisions at the centre-of-mass energy of $\sqrt{s} = 13$ TeV. These data were collected in 2017 in a dedicated run with low instantaneous luminosity. The presented study is the first attempt to analyse the MPI effects in a sample enhanced with diffractive processes.

The measured MPI sensitive observables are: the mean charged track multiplicity, the mean of the sum of the charged particle track transverse momenta, and the mean charged track transverse momentum. The observables were constructed using charged particle tracks with the absolute pseudorapidity up to 2.5 and with the transverse momentum greater than 500 MeV. In addition, the presence of the leading track, the charged particle track with the transverse momentum above 1 GeV, and a diffractively scattered proton with the relative energy loss between 3.5% and 8% were required.

The measurements were performed in three regions of the azimuthal angle defined with respect to the leading track. These regions have different sensitivity to MPI. Two types of background were estimated and their contributions were subtracted statistically from the experimental distributions. The results were corrected for the detector effects – the track and vertex reconstruction efficiencies and the AFP trigger inefficiency. Predictions of the Pythia 8 A2 single diffractive Monte Carlo were compared to the experimental results and it was found that they fail to reproduce the data. Tuning of the Pythia 8 single diffractive Monte Carlo parameters was attempted and the resulting model provides a much better description of the experimental data.

Streszczenie

Niniejsza rozprawa doktorska poświęcona jest pomiarowi efektów oddziaływań wielopartonowych występujących w przypadkach dyfrakcyjnych w zderzeniach proton-proton na akceleratorze LHC. Jedną z sygnatur takich oddziaływań jest obecność nietkniętego protonu, zwanego protonem dyfrakcyjnym, który może być zmierzony przez detektory do przodu. Przykładem takich detektorów, będących częścią eksperymentu ATLAS, są detektory AFP. Analiza przeprowadzona w niniejszej pracy opiera się na danych o scałkowanej świetlności wynoszącej około 56 nb^{-1}, pochodzących z oddziaływań proton-proton przy energii zderzenia w układzie środka masy wynoszącej 13 TeV. Dane te zostały zebrane w 2017 roku w trakcie specjalnych okresów zbierania danych, w których akcelerator pracował z niską świetlnością chwilową. Warto podkreślić, że to jest pierwsza analiza mająca na celu pomiar efektów oddziaływań wielopartonowych w przypadkach dyfrakcyjnych.

W pracy analizowano rozkłady wrażliwe na efekty oddziaływań wielopartonowych: średniej krotności naładowanych śladów, sumy pędów poprzeczych naładowanych śladów i średni pęd poprzeczny naładowanych śladów. Obserwable te oparto o naładowane ślady, których absolutna wartość pseudorapidity jest mniejsza niż 2,5 oraz i których pęd poprzeczny jest większy niż 500 MeV. Ponadto wymagana była obecność naładowanego śladu, sładu wiodącego, którego pęd poprzeczny przekracza 1 GeV, oraz dyfrakcyjnego protonu, którego względna stata energii wynosi pomiędzy 3,5 i 8%.

Pomiar został przeprowadzony w trzech obszarach kąta azymutalnego wyznaczanego względem śladu wiodącego. Obszary te charakteryzują się różną czułością na efekty oddziaływań wielopartonowych. Otrzymane rozkłady badanych obserwabli zostały poprawione na efekty związane z wydajnością rekonstrukcji wierzchołka i śladu oraz wydajnością trygera AFP. Oszacowane zostały również przyczynki dwóch rodzajów tła. Przewidywania modelu Monte Carlo, Pythia 8 A2, dla oddziaływań pojedynczej dysocjacji dyfrakyjnej, zostrały skonfrontowane z wynikami pomiarów. Okazało się, że model ten nie potrafi opisać mierzonych zależności. Przeprowadzono próbę justowania parametrów modelu Pythia 8 A2 dla oddziaływań pojedynczej dysocjacji dyfrakyjnej, w wyniku której otrzymano wersję modelu dostarczającą znacznie lepszy opis danych doświadczalnych.

Contents

Preface **5**

1 Introduction **9**
1.1 Standard Model . . . 9
1.2 QCD – an overview . . . 10
1.3 Overview of hadron-hadron collisions . . . 15
1.4 Multiple Parton Interaction . . . 18
1.5 Diffractive processes . . . 20
1.6 Pythia event generator . . . 23

2 Experimental apparatus **27**
2.1 Large Hadron Collider . . . 27
2.2 ATLAS . . . 29
2.2.1 ATLAS Inner Detector . . . 31
2.2.2 MBTS . . . 32
2.2.3 ATLAS Forward Proton . . . 32
2.2.4 Trigger and Data Acquisition systems . . . 34

3 Forward proton reconstruction **37**
3.1 AFP geometrical acceptance . . . 37
3.2 Alignment of the AFP detectors . . . 38
3.3 Cluster reconstruction . . . 40
3.4 Track reconstruction . . . 40
3.4.1 Track finding algorithm . . . 41
3.4.2 Reconstruction of the track parameters . . . 41
3.5 Proton reconstruction . . . 41
3.5.1 Optics and transport simulation . . . 41
3.5.2 Proton kinematics reconstruction . . . 42
3.6 Fast AFP simulation . . . 43

4 Data analysis **45**
4.1 Data preparation . . . 46
4.1.1 Initial data selection . . . 47
4.1.2 Final data selection . . . 48
4.2 Efficiencies . . . 50
4.2.1 Track reconstruction . . . 50
4.2.2 Vertex reconstruction . . . 53
4.2.3 AFP trigger . . . 53

4.2.4 Corrections . . . 55
4.3 Background . . . 56
4.3.1 Non-diffractive background . . . 56
4.3.2 Combinatorial model uncertainties . . . 60
4.3.3 Corrections for the MBTS inefficiency . . . 60
4.3.4 Merged vertex background . . . 62

5 Results **65**
5.1 Charged particle multiplicity and transverse momentum distributions . . . 65
5.2 Angular distributions of $\langle n_{trk} \rangle$ and $\langle \Sigma p_T \rangle$ . . . 66
5.3 The p_T^{lead} dependence of $\langle n_{trk} \rangle$ and $\langle \Sigma p_T \rangle$ . . . 67
5.4 n_{trk} and Σp_T densities in transverse min/max/diff regions . . . 69
5.5 Mean transverse momentum in transverse, transMin and transMax regions . . . 72
5.6 Summary of measurements . . . 72

6 Monte Carlo tuning **75**
6.1 Pythia parameters . . . 75
6.2 Parameter minimisation . . . 81
6.2.1 One-dimensional minimisation . . . 82
6.2.2 Correlations between parameters . . . 85
6.3 Multi-parmeter fit . . . 85

7 Summary and conclusions **91**

A Additional information **93**

Preface

Precise tests of the Standard Model or searches for new phenomena at hadron colliders require not only a good understanding of the primary short-distanced scatterings, but also of the accompanying interactions of the rest of the proton-proton system, named the Underlying Event (UE). The largest contribution to the UE activity is due to the Initial- and Final-State Radiation and Multi-Parton Interactions. The accurate description of these phenomena by the phenomenological and theoretical models implemented in the Monte Carlo generators are of great importance for the LHC physics programme.

Diffractive processes constitute a significant fraction of inelastic interactions in proton-proton collisions. An exchange of a colour-singlet object in such a process may result in two main features of diffractive events. One is the presence of a region devoid of any particle – the large (pseudo)rapidity gap. The other signature is the presence of an intact forward proton scattered at a very small angle. In the case of an experiment at the colliding beams accelerator, the gap is observed in the central detector. The registration of the forward emitted proton(s) requires a dedicated experimental set-up. Typically, such detectors constitute a system located along the beam line at large distances from the interaction point. The measurement of the forward scattered proton(s) exploits the machine magnetic lattice and to position the detectors in the immediate vicinity of a beam the Roman Pot or the Hamburg beam pipe technique is utilised. A modern experimental set-up of Forward Detectors may contain the tracking and timing detectors delivering the trigger and allowing reconstruction of the proton kinematics as well as the background discrimination. The physics programme of forward detectors at the LHC ranges from precise measurements of the elastic scattering, resulting elastic and total cross-sections or precise determination of the machine luminosity, through the analysis of soft and hard diffractive dissociation, to the investigations of the photon-photon interactions and the searches of the Beyond Standard Model effects.

In this thesis, the proton-proton collision data taken with the ATLAS detector at the centre-of-mass energy of $\sqrt{s} = 13$ TeV were studied. In particular, special emphasis was put on the study of single diffractive processes and in particular, on the effects of the Multi-Parton Interactions in such interactions. As a signature of the single diffractive process the presence of the intact forward scattered proton in the ATLAS Forward Proton detector was requested. The observables used in the present analysis were constructed using information on the charged particle tracks delivered by the ATLAS tracking system. The present studies constitute the first measurement of the Multi-Parton Interactions in diffractive processes. The obtained results, corrected for various experimental effects, can be confronted with predictions of phenomenological or theoretical models. In this thesis, predictions of the Pythia 8 Monte Carlo model of single diffractive dissociation are confronted with the data. Moreover, results of the performed measurements constitute the base for the tuning of the models and the obtained results of such a procedure are presented.

The author of this thesis took an active part in all stages of the analysis starting from the beam tests of the experimental apparatus, through the data taking, commissioning, and software development to the analysis of the MPI effects. It is clear that parts of the mentioned tasks were done in collaboration with responsible teams. However, the implementation of the reconstruction of the forward proton kinematics based on the AFP delivered data is the author's original achievement. It is to be used by all analyses involving the AFP data.

The author of this thesis is an ATLAS author and hence he signs all ATLAS Collaboration publications since December 2018. Below, a list of publications with the author's significant contribution is given:

- ATLAS Collaboration (K. Cieśla), Observation and Measurement of Forward Proton Scattering in Association with Lepton Pairs Produced via the Photon Fusion Mechanism at ATLAS, Phys. Rev. Lett. **125** (2020) 261801,
- ATLAS Collaboration (K. Cieśla), Charged Particle Multiplicity Distribution in Single Diffractive Processes Tagged with the AFP, in preparation,
- K. Cieśla et al., On the Centrality Determination with Forward Proton Detectors, Ukr. J. Phys. **64** (2019) 7, 554,
- K. Cieśla et al., Detecting Nuclear Debris with the Forward Proton Detectors at the LHC, Photonics Applications in Astronomy, Communications, Industry, and High-Energy Physics Experiments 2019, Proc.SPIE vol.11176
- R. Staszewski, K. Cieśla, J.J. Chwastowski, Forward proton detectors in heavy ion physics, Acta Physica Polonica **B 50** (2019) 1229,
- J. Lange (K. Cieśla) et al., Beam tests of an integrated prototype of the ATLAS Forward Proton detector, JINST **11 09** P09005 (2016),
- Nozka, L. (K. Cieśla) et al., Construction of the optical part of a time-of-flight detector prototype for the AFP detector", Opt. Express **24** (2016) 27951.
- K. Cieśla and R. Staszewski, Flexibility of LHC Optics for Forward Proton Measurements, Acta Phys. Polon. **B 47** (2016) 1633.

The first two publications are devoted to the study of diffractive dissociation and photon-photon interactions with the help of the AFP detectors. The others discuss potential application of the AFP in ion-ion physics and the tests of the apparatus. Some of the studied topics were also presented during conferences or workshops and the list appended.

- Photon-photon fusion measurements at ATLAS, on behalf of the ATLAS Collaboration, Low-x Meeting 2021, Elba, Italy, 26 September – 1 October 2021,
- Single diffractive charged particle multiplicity with AFP at 13 TeV, ATLAS ARP General Meeting, 7 – 9 October 2020, Geneva, CERN,
- AFP: first physics and performance results, ATLAS Physics Week, Geneva, CERN, 10 – 15 February, 2019,
- On the Centrality Determination with Forward Proton Detectors, New Trends in High-Energy Physics, Odessa, Ukraine, 12 – 18 May 2019,
- Detecting Nuclear Debris with the Forward Proton Detectors at the LHC, XLIV-th IEEE-SPIE Joint Symposium Wilga, Wilga, Poland, 26 May – 2 June 2019,

- Diffractive Analyses, ATLAS Standard Model Workshop, Belgrad, Serbia, 17 – 20 September 2019,
- Status of kinematic reconstruction for forward proton, ATLAS Forward Physics and Detector Workshop, Geneva, CERN, 14 – 15 March 2018.

The thesis is organised as follows. Chapter 1 starts with a brief introduction of the Standard Model – theory describing elementary particles and their interactions. The greatest emphasis is put on the QCD – the quantum field theory of strong interactions. Next, a step-by-step overview of the processes occurring in collision of two hadrons, including the MPI, is presented. Finally, the description of the diffractive processes is provided.

Chapter 2 is dedicated to the experimental apparatus. It starts with the description of the LHC accelerator. The outline of the ATLAS central detector and its subcomponents is provided. This includes the Inner Detector, MBTS, TDAQ and most importantly the AFP detectors – dedicated to the diffractive measurements.

Chapter 3 is devoted to the explanation of the proton reconstruction procedure, beginning with the description of forward proton kinematics and the detector alignment. Next, the description of each reconstruction step is provided. Starting from detector hits, going through clusters and tracks, it finishes with proton reconstruction methods. The simulation of AFP is also presented.

Chapter 4 covers the data analysis. At first, the definition of the signal events and observables is provided. Then, the data samples are introduced together with the description of the event and track selection. Finally, the corrections to the measured observables are explained, including the detector efficiencies and the background subtraction.

Chapter 5 discusses he obtained results concerning the distributions of the UE-sensitive variables. Predictions of the Pythia 8 A2 single diffractive Monte Carlo are compared to the measurements.

Chapter 6 is dedicated to the Monte Carlo tuning study. It starts with the description of the tunable parameters and their impact on the measured observables is discussed. Next, the multi-step tuning procedure is explained and its results are discussed. Finally, a global fit with the chosen parameters is performed and the Monte Carlo predictions derived using the fitted parameters are compared to the experimental data and results obtained with Pythia 8 A2 single diffractive Monte Carlo.

Chapter 1

Introduction

1.1 Standard Model

The presently and widely accepted theory describing elementary particles and interaction between them is called the Standard Model. It includes a description of the electromagnetic, weak and strong interactions. Fundamental particles of the Standard Model are divided into two main subgroups, see Fig. 1.1:

- fermions – the 1/2 spin building blocks of known matter.The fermions are further divided into two groups:
  - six quarks (and six anti-quarks) which are constituents of hadrons: mesons, composed of a quark and anti-quark (e.g., pion, $\pi^+ = u\bar{d}$ – up and anti-down quarks), and baryons, composed of three quarks or three anti-quarks (e.g. proton, $p = uud$ – two up and one down quarks). There are also more exotic particles like tetra- or penta-quarks, composed of two quarks and two anti-quarks or four quarks and one anti-quark, respectively, but their properties are not well established yet [1, 2]. Fermions are bound together by the strong force, due to quarks carrying the colour charge. The quarks are also electrically charged (carrying fractions $|^1/_3|$ or $|^2/_3|$ of the elementary charge) and they can interact electromagnetically, and weakly (e.g. a neutron decay into a proton, electron and neutrino).
  - six leptons (and six anti-leptons), with three of them being electrically charged: electron, muon and taon, and corresponding to them three neutral and nearly massless neutrinos.
- bosons – characterised by integer spins and split into two groups: the gauge bosons (mediating elementary interactions; with a unit spin), and a scalar boson which spin is equal to zero. The gauge boson group consists of:
  - photon γ – a massless and neutral carrier of the electromagnetic force. Photons couple only to charged particles. The theory describing electromagnetic interactions is called Quantum Electrodynamics (QED).
  - gluons g – massless and colour-charged carriers of strong force. Unlike photons, gluons posses the colour charge, thus they can interact with each other, introducing a variety of processes which are absent in QED. The theory describing strong interactions is called Quantum Chromodynamics (QCD).

– weak bosons $W^{\pm}$, Z^0 – massive ($W^{\pm}$ – 80 GeV and Z^0 – 91 GeV) mediating weak interactions, which are responsible for radioactive decays (e.g. neutron decay, $n^0 \rightarrow p^+ + (W^- \rightarrow e^- \bar{\nu}_e)$). The interaction was initially described by Quantum Flavourdynamics, but currently is described better by Electroweak Theory (EWT) which unifies the electromagnetic and weak interactions.

Standard Model foresees the existence of a single scalar boson called the Higgs boson, which is the latest and heaviest (125 GeV) discovered fundamental boson. It is responsible for providing particles with mass via their interaction with the Higgs field.

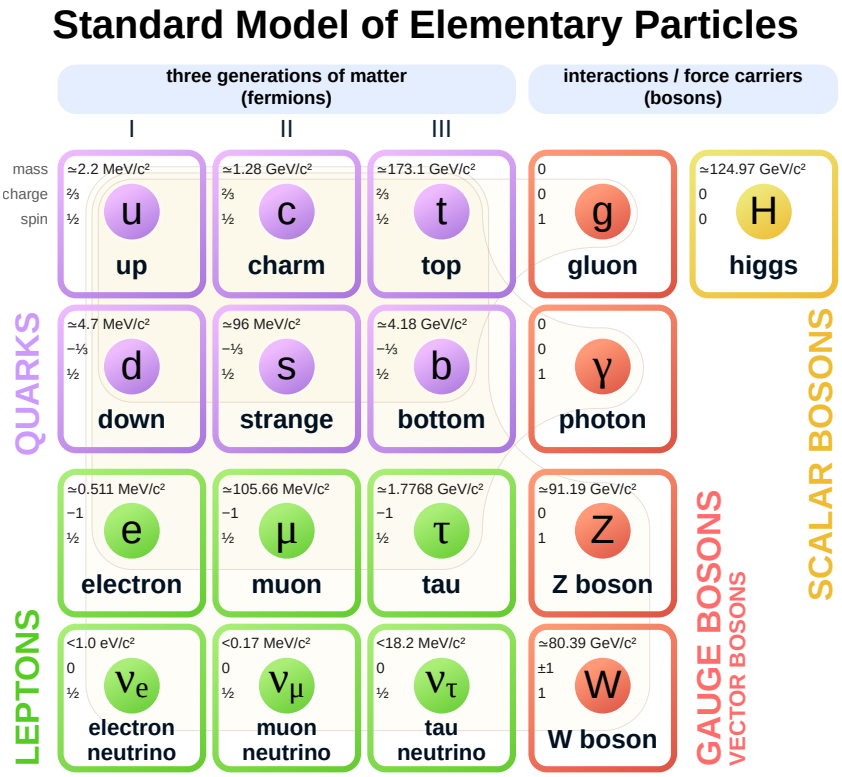

Figure 1.1: Overview of Standard Model particles. [3]

Gravitational interactions are not included into the Standard Model as there is no complete quantum field theory of gravitons, hypothetical spin 2 particles responsible for mediating this interaction. Gravity is currently described by Einstein's General Relativity.

1.2 QCD – an overview

Quantum Chromodynamics (QCD) is a Quantum Field Theory describing the strong interaction between the colour charged particles. QCD is based on the $SU(3)$ gauge symmetry group with three colour charges and eight interaction mediators known as gluons. Figure 1.2 shows the Feynman diagrams of the fundamental couplings for both QED and QCD.

In case of QED, an electrically charged electron radiates a photon mediating electromagnetic interaction. The strength of the interaction is driven by the fine-structure constant α and its value is approximately $^1/_{137}$ and depends very mildly on the energy growing with it.

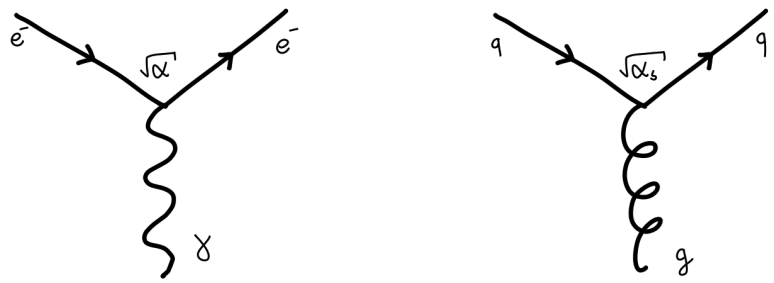

(a) photon radiation (b) gluon radiation

Figure 1.2: Diagrams of the fundamental QED (left) and QCD (right) couplings.

In QCD, the colour-charged quark emits a gluon mediating strong interactions. Here, the running of the coupling constant α_s is of primordial importance. This originates from the fact that the gluons carry the colour charge (colour charge and anti-charge) and, unlike the photons, can interact with each other. Figure 1.3 presents three elementary QCD couplings: the gluon radiation, three- and four- gluon self-coupling. The consequences of this are phenomena called the colour confinement and asymptotic freedom.

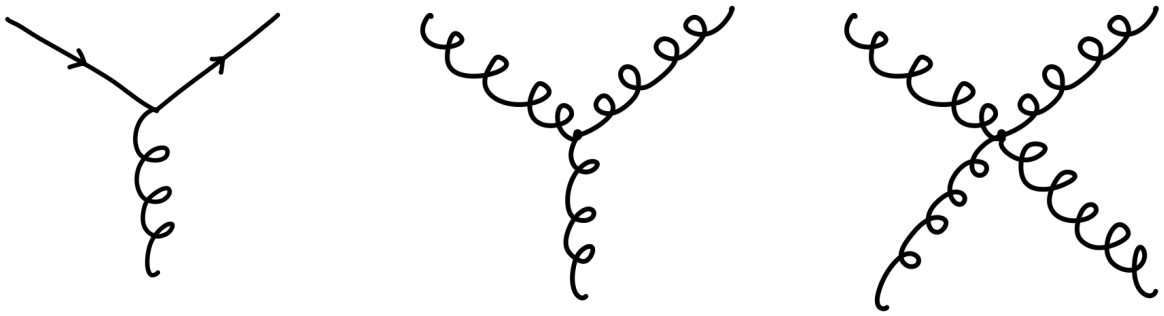

(a) gluon radiation (b) gluon self-coupling

Figure 1.3: Diagrams of all the fundamental QCD couplings. Force carrier self-interaction is present only in QCD.

The concepts of the quantum fluctuations, screening and anti-screening play a very important role in QCD. The quantum fluctuations are represented by a cloud of virtual quark–anti-quark pairs around a quark. In diagrams, the virtual pairs are depicted as closed loops. This phenomenon is present for both QED and QCD, and an example of the related graphs is presented in Figure 1.4.

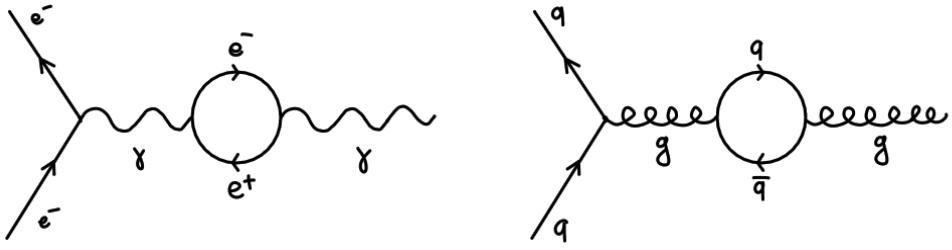

Figure 1.4: Screening.

The additional virtual pairs polarise the vacuum around the charge: virtual particles of unlike charge are attracted to the charge while those with the same charge are repelled. The net effect is a partial cancellation or *screening* of the charge causing the effective charge of a particle to decrease asymptotically to some value with increasing distance. In the calculations, additional loops are taken into account using the perturbative approach. In case of QCD, due to the gluon self-interaction, the quantum fluctuations include also gluon loops, see Figure 1.5.

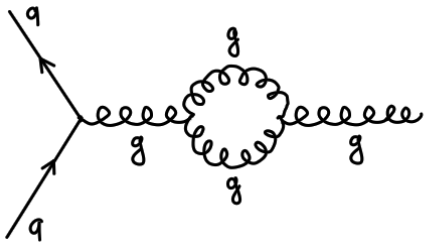

Figure 1.5: Anti-screening.

In case of QCD, due to the gluon self-interaction, the quantum fluctuations include also gluon loops, see Figure 1.5. There is no equivalent of such a phenomenon in QED. The effect is opposite to the screening, therefore it is called *anti-screening*, since gluons carry both the colour charge and anti-charge. This modifies the colour field properties and leads also to its amplification. When the anti-screening dominates, the effective charge increases with increasing distance. In QCD, the anti-screening dominates and the *running coupling constant* behaves as:

$$\alpha_s(Q^2) = \frac{1}{\beta_0 \ln(\frac{Q^2}{\Lambda^2}))}, \tag{1.1}$$

where β_0 is a constant first computed by Politzer [4], Gross and Wilczek [5], Q^2 is the energy scale and Λ is called *the lambda QCD* or the QCD scale and its value is around 200 MeV.

Figure 1.6 presents the relation between the energy scale and the strong coupling constant value. At high energy scales, the value of the coupling constant is $\alpha_s \ll 1$. Hence, the higher order contributions in perturbative calculations are small and the perturbation methods deliver accurate results. This regime is called the **asymptotic freedom**. At small Q^2 values or large distances, the value of the strong coupling constant becomes large which invalidates the use of perturbative methods in this region. This is the so-called non-perturbative region requiring dedicated methods to perform meaningful calculations.

Colour confinement:
Experimental observations show no evidence of free quarks. Only systems of bound quarks are observed in the form of the colour neutral (colour singlet) hadrons.

The mechanism of the colour confinement can be illustrated by considering the potential between two quarks, which behaves as:

$$V_{QCD}(r) = -\frac{4}{3}\frac{\alpha_s}{r} + kr, \tag{1.2}$$

where k denotes a constant equal to 1 GeV/fm. For small distances between the quarks the first term dominates. The quarks behave as almost free particles (the asymptotic freedom).

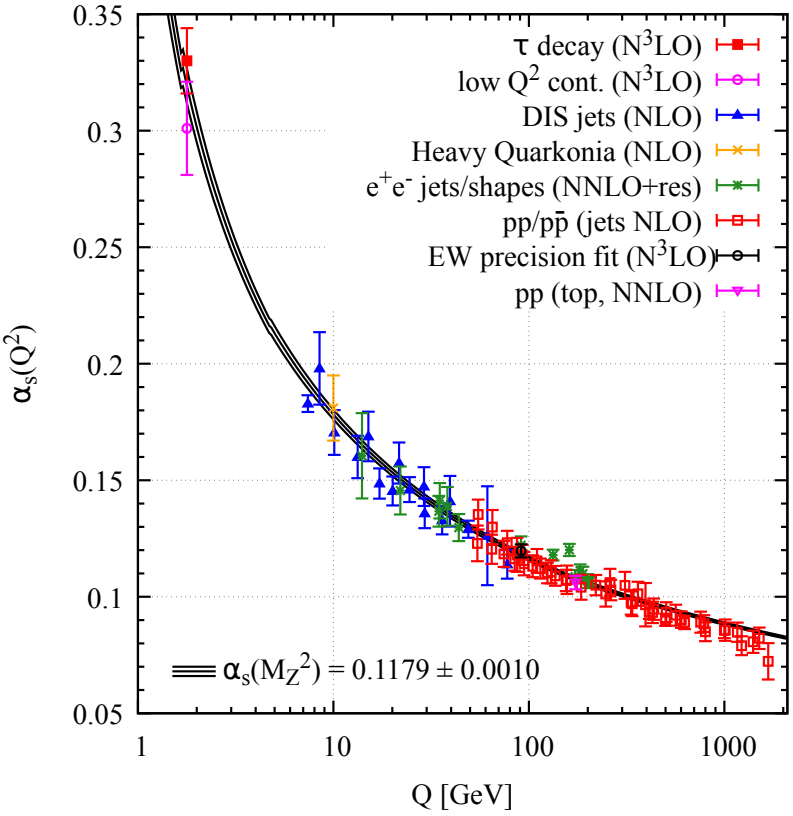

Figure 1.6: Relation between energy scale and value of coupling constant. From [6]

However, with increasing distance between the quarks the second term takes over. The potential rises to the point where the binding energy between the quarks exceeds the mass of a quark pair. To minimise the system potential energy the colour field collapses and creates a new quark–anti-quark pair. The process is illustrated in Figure 1.7.

The colour confinement is profoundly related to the gluon self-interactions. Colour charged particles: quarks and gluons are confined inside the QCD potential in colour-neutral hadrons.

Deep inelastic scattering and parton distribution functions: The evidence of the partonic structure of hadrons was provided by experiments dedicated to the lepton–hadron scattering, to the study of the deep inelastic scattering (DIS) process. In this process, in the vast majority of cases, a lepton emits a virtual photon (with virtuality Q^2) which interacts with a quark carrying a fraction x of the proton momentum. A diagram of a DIS process mediated by a virtual photon is presented in Figure 1.8.

The experimental data deliver information allowing construction of a function describing the observation probability of a parton (in a proton) with a given x, at the scale Q^2 – the parton distribution functions (PDF). Examples of the proton PDF are shown in Figure 1.9 for two Q^2 values. Since a proton consists of two up and one down valence quarks, the probability of finding an up quark is roughly double of finding a down quark. The probability of finding gluons increases with decreasing value of x. However, it is also possible to find heavier quarks and also anti-quarks. This shows that protons consist not only of the valence quarks, but also a sea of quarks, anti-quarks and gluons.

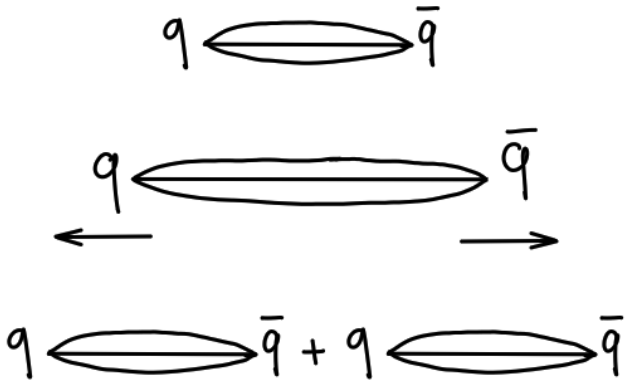

Figure 1.7: Quark separation. When the binding energy between the quarks exceeds the mass of a quark pair, the field collapses creating a new quark anti-quark pair.

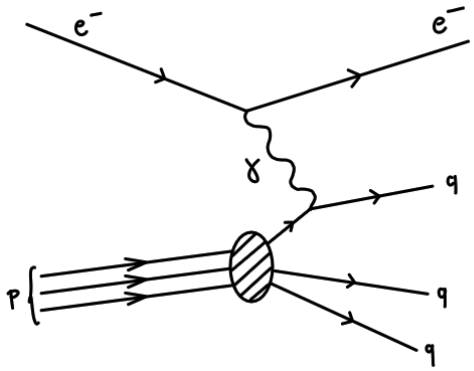

Figure 1.8: Diagram of deep inelastic scattering.

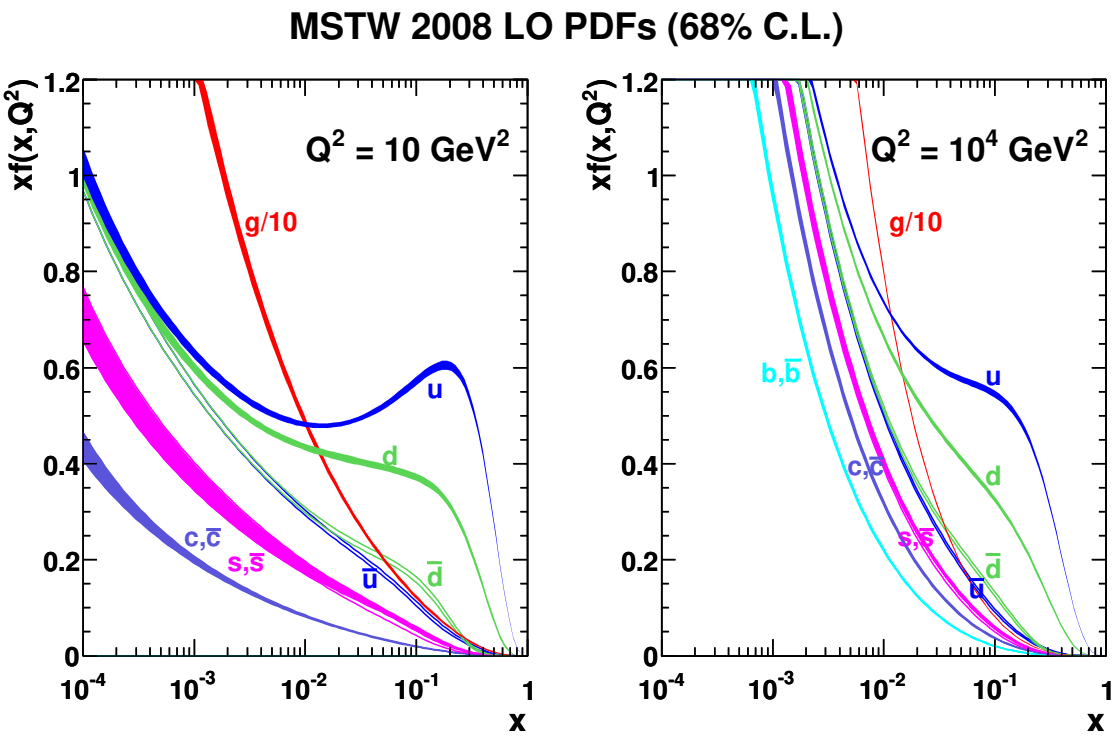

Figure 1.9: MSTW2008LO Parton Distribution Function. From [7]

1.3 Overview of hadron-hadron collisions

The proton structure is very rich and complex. It consists of the valence and the sea quarks and gluons which all are called partons. Therefore, collisions of high-energy protons can lead to very complex processes, which have to be reflected by the phenomenological and theoretical models including those exploiting the Monte Carlo methods.

Figures 1.10 through 1.13 show schematic illustrations of a hard proton-proton collision and accompanying processes:

- **Hard scattering**: Initially there are two high-energy protons approaching each other (Figure 1.10a). A single parton from the first proton interacts with a single parton of the second proton (Figure 1.10b). This particular example shows a $gq \rightarrow gq$ process which can be described using perturnative QCD (pQCD).

  However, the hard scattering is not the only process to occur in a collision of two protons. There are many additional interactions involving the initial and final particles, and interactions between spectator partons, which are collectively termed as the Underlying Event (UE). The UE is often defined also as "all interactions besides the hard scattering". The three most significant UE processes are the Initial- and Final-state radiation (ISR and FSR) and Multiple Parton Interaction (MPI).

- **Initial-** and **Final-state radiation**: Both initial and final state consists of high energy and colour or electrically charged particles. Such particles can radiate new particles such as gluons ($q \rightarrow qg$) or photons ($q \rightarrow q\gamma$). These processes are shown in Figure 1.11. Additional branching and emissions can cause parton cascades (parton showers). Depending on the emission source they are referred to as Initial- or Final-state radiation.

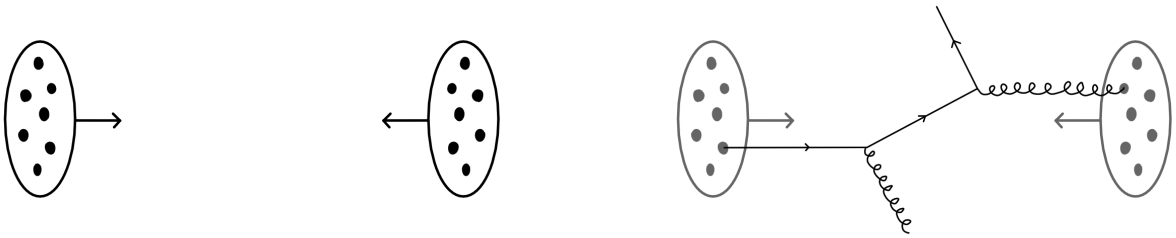

(a) Initial state.

(b) Hard scattering.

Figure 1.10: Schematic view of a proton-proton collision. **Left**: Initial state. Two protons moving towards each other. Each proton is composed of many partons (black dots). **Right**: Hard scattering. Two partons, one from each proton, interact with each other producing new particles: $gq \to gq$.

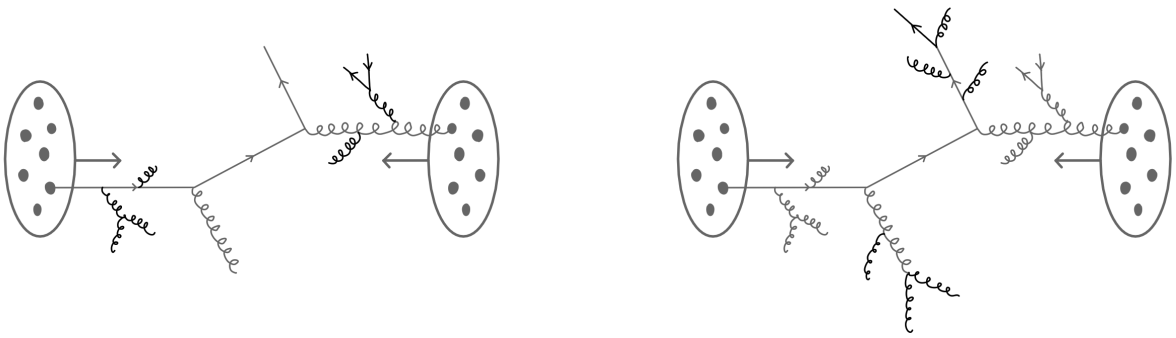

(a) Initial-state radiation.

(b) Final-state radiation.

Figure 1.11: Schematic view of a proton-proton collision. Emissions from the initial (left) and final (right) state. Radiated particles may branch and emit other particles causing parton showers.

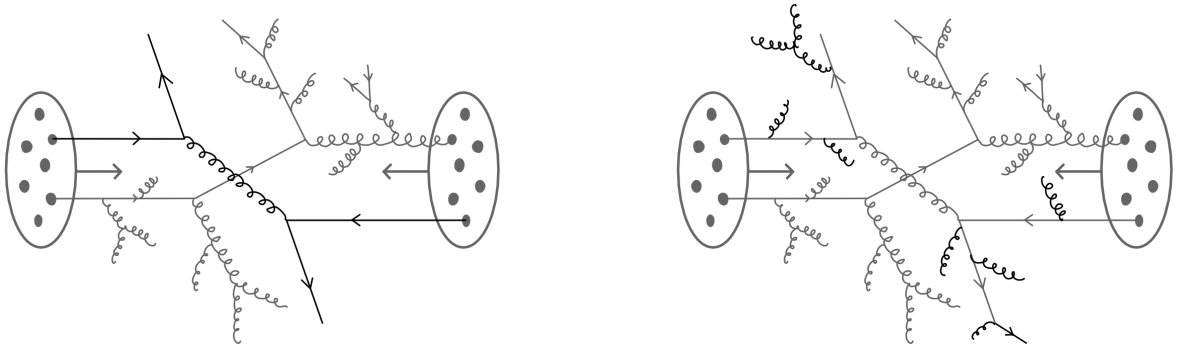

(a) Multiple Parton Interaction.

(b) MPI with ISR and FSR.

Figure 1.12: Schematic view of a proton-proton collision. An additional pair of partons may interact with each other producing new particles (left). The initial and final state radiation can occur in addition to the MPI (right).

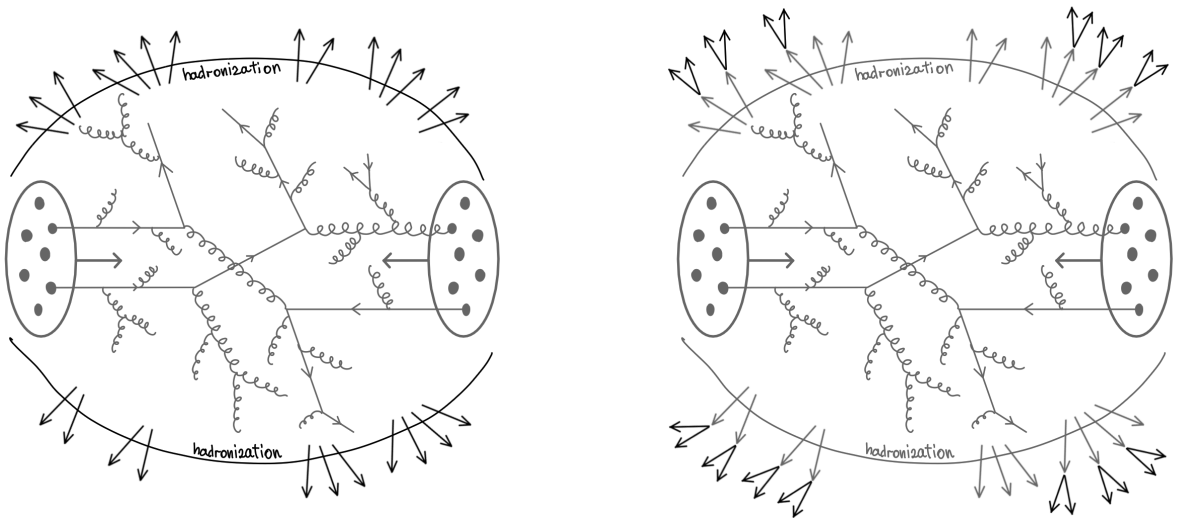

(a) Hadronization.

(b) Decay of unstable hadrons.

Figure 1.13: Schematic view of a proton-proton collision. Recombination of colour-charged quarks and gluons into colour-neutral hadrons (left). Unstable hadrons decay into new particles (right).

- **Multiple Parton Interaction**: Since hadrons have a complex partonic structure therefore during the hadron-hadron collision more than one pair of partons may interact (cf. Fig. 1.12). This phenomenon is referred to as Multiple Parton Interaction (MPI). MPIs provide a significant contribution to the event activity and are necessary for a proper description of the measured final state. MPIs are described in more detail in Section 1.4.

- **Hadronisation**: At this point of proton-proton interaction the produced particles consist mostly of the colour charged quarks and gluons. Since the final state particles can only be colour singlets then quarks and gluons have to recombine (see Fig. 1.13a). The hadrons emerging from hadronisation may further decay into lighter particles (Figure 1.13b).

1.4 Multiple Parton Interaction

To illustrate the importance of the MPI, Figure 1.14 shows predictions of the Pythia 8 Monte Carlo [8] with and without the MPI are compared to the ATLAS measurement of the charged particles multiplicity distributions at the centre-of-mass collision energy of $\sqrt{s} = 7$ TeV. If the MPIs are not included the Monte Carlo does not describe the data. The shapes of the distributions largely differ. The impact of the parton showers originating from ISR and FSR is much smaller than that of the MPIs. Therefore, Multiple Parton Interactions are essential for a proper description and reproduction of the data features.

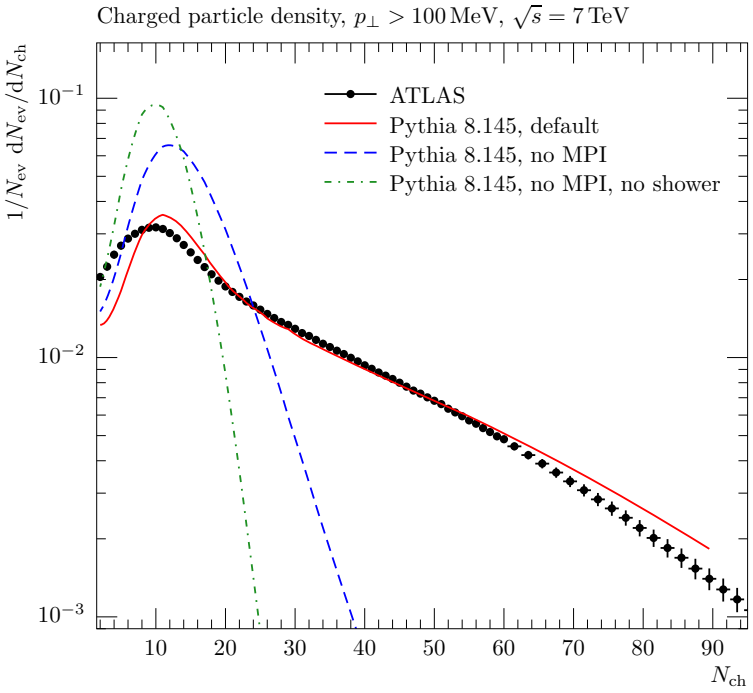

Figure 1.14: Comparison of charged particle multiplicities between ATLAS data at $\sqrt{s} = 7$ TeV [9] and various Monte Carlo models with and without MPI. [10]

A mechanism of the MPI phenomenon implemented in Pythia was presented by Sjöstrand and van Zijl in [11]. One can consider the differential cross-section for $2 \to 2$ hard QCD process as a function of p_T^2:

$$\frac{d\sigma_{hard}}{dp_T^2} = \sum_{i,j,k} \iiint dx_1 dx_2 d\hat{t} f_i^1(x_1, Q^2) f_j^2(x_2, Q^2) \frac{d\hat{\sigma}_{ij}^k}{dp_T^2} \delta(p_T^2 - \frac{\hat{t}\hat{u}}{\hat{s}}), \tag{1.3}$$

where $\hat{\sigma}_{ij}^k$ is the cross-section for process k possible between partons i and j. The parton distribution functions $f_i^a(x, Q^2)$ give the probability of finding parton i carrying a fraction x of the momentum of the incoming hadron a, probed at the scale Q^2. The Mandelstam variables $\hat{s}$, $\hat{t}$, $\hat{u}$ are related to the momenta of the incoming (p_1 and p_2) and outgoing (p_3 and p_4) particles by:

$$\begin{aligned} \hat{s} &= (p_1 + p_2)^2 = (p_3 + p_4)^2, \\ \hat{t} &= (p_1 - p_3)^2 = (p_4 - p_2)^2, \\ \hat{u} &= (p_1 - p_4)^2 = (p_3 - p_2)^2. \end{aligned} \tag{1.4}$$

For massless partons, the Mandelstam variables are related by:

$$\begin{aligned} \hat{s} + \hat{t} + \hat{u} &= 0, \\ \hat{s} &= x_1 x_2 s, \end{aligned} \tag{1.5}$$

where s is the centre-of-mass hadron-hadron collision energy squared. The cross-section for $2 \to 2$ QCD processes is dominated by the t-channel gluon exchange: $qq \to qq$, $gq \to gq$ and $gg \to gg$. Using Equation 1.3 for interactions where $\hat{t} \ll \hat{s}$, the approximation

$$Q^2 = p_T^2 = \frac{\hat{t}\hat{u}}{\hat{s}} \approx \hat{t}$$

can be considered. Hence, the differential cross-section can be expressed as:

$$\frac{d\sigma_{hard}}{dp_T^2} \approx \iint dx_1 dx_2 F(x_1, p_T^2) F(x_2, p_T^2) \frac{d\hat{\sigma}}{dp_T^2}, \tag{1.6}$$

where F is the averaged PDF and:

$$\frac{d\hat{\sigma}}{dp_T^2} = \frac{8\pi\alpha_s^2(p_T^2)}{9p_T^4}. \tag{1.7}$$

Neglecting the integrals over x_1, x_2 and for constant α_s, the integrated cross-section above some p_{Tmin} is:

$$\sigma_{hard}(p_{Tmin}) = \int_{p_{Tmin}^2}^{s/4} \frac{d\sigma}{dp_T^2} dp_T^2 \propto \frac{1}{p_{Tmin}^2}. \tag{1.8}$$

In the limit $p_{Tmin} \to 0$, the integrated cross-section diverges, exceeding the total cross-section for hadron-hadron interaction for p_{Tmin} of the order of few GeV. Figure 1.15 shows the comparison of the integrated and total cross-sections obtained for the Tevatron and LHC energies.

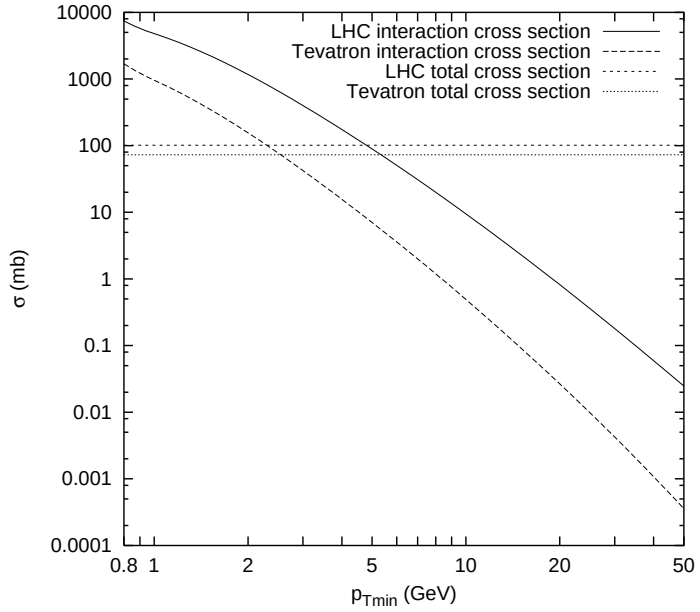

Figure 1.15: Comparison of the integrated and total cross-sections for the Tevatron (1.8 TeV) and the LHC (14 TeV) collision energies. [12]

This problem can be solved by recognising that σ_{hard} is the parton-parton and not the hadron-hadron cross-section. One should observe that a single event containing two parton–parton interactions counts twice in the parton-level cross-section calculations but only once in the case of the hadron-level cross-section. Therefore, the ratio of these two numbers is the measure of the average number of interactions per hadron-hadron collision:

$$\frac{\sigma_{hard}(p_{Tmin})}{\sigma_{tot}} = \langle n \rangle (p_{Tmin}). \tag{1.9}$$

For an in depth explanation a reader is referred to [11–15].

1.5 Diffractive processes

When two high-energy protons collide, at least one parton from the first proton interacts with another one from the second proton. Typically, such an interaction leads to a colour flow between the protons leaving them in a non-singlet colour state. Since only the colour neutral particles exist in nature, the protons excited in an interaction break and their remnants recombine into the streams of hadrons – the proton remnants. This class of events is called non-diffractive and an example of such a process is shown in Figure 1.16a.

However, it is possible for one or both protons to stay intact after a collision. This is possible if the interaction is mediated by a colour singlet exchange. One possibility is the electromagnetic process mediated by a photon. Figure 1.16b shows an example of such a process – the exclusive (photo)production of a lepton pair. The exclusivity condition means that all final state particles can be measured in an experiment.

The other possibility is offered by an exchange of a colour singlet object, which is a system

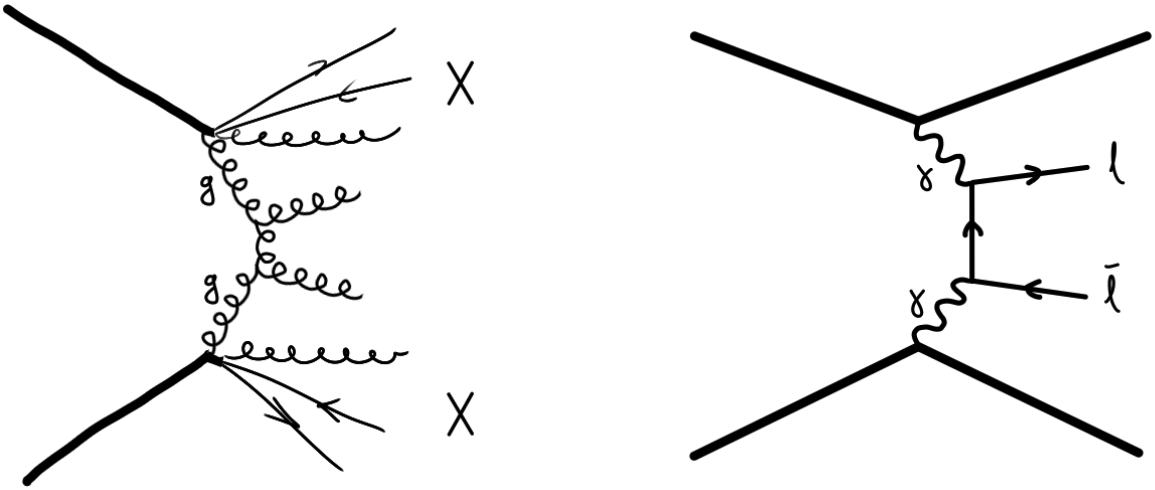

(a) Non-diffractive jet production. (b) Exclusive production of a lepton pair.

Figure 1.16: The Feynman diagrams of the non-diffractive dijet production (right) and the exclusive production of a lepton pair.

of more than a single gluon. The most notable examples are a pomeron and an odderon. The first one is responsible for the increase of the cross-section with $\sqrt{s}$ and the second one is an odd charge parity partner of the pomeron. Such interactions are well described by the Regge theory [16–18]. In QCD, these two objects are represented, at the lowest order, by a colour-singlet ensemble of two or three gluons, respectively. The simplest process involving the pomeron exchange is the elastic scattering, see Figure 1.17a, where the pomeron is indicated as two parallel lines.

In the elastic process, both protons survive the interaction with their energy unchanged. However, due to the exchange of a pomeron, their transverse momentum changes. Typically, the protons scatter at very small angles, which requires a dedicated apparatus to register them. In the case when the energy transfer does occur, one or both protons may dissociate into a system of particles carrying the quantum numbers of a proton. This group of processes is called single or double diffractive dissociation (or single and double diffraction), respectively. Another possibility is that two pomerons emitted by the protons interact with each other producing some central state – the central diffraction process. Single or double diffractive dissociation can occur simultaneously with central diffraction. Figure 1.17 presents examples of diffractive processes.

An exchange of a colour singlet profoundly impacts the final state of an interaction. Namely, it leads to a region devoid of particles – the (pseudo)rapidity gap. This feature is used to distinguish diffractive processes. This is illustrated in Figures 1.18 and 1.19, which provide a comparison between non-diffractive and diffractive processes. Each figure presents a part of a Feynman diagram of a process in question (left) and a schematic distribution of the final state particles in the (pseudo)rapidity space (right). For the non-diffractive process (Figure 1.18) the initial proton emits a parton participating in a hard collision producing a central system. This causes the proton breakup, as its colour charge is no longer neutral. In the right plot there are two marked areas, one corresponds to the central system near the (pseudo)rapidity value of zero, and the other, located further away from zero, is populated by the remnants. Those two regions may overlap, making the distinguishing of the final state particle origin ambiguous.

In a diffractive process (Figure 1.19) a pomeron is emitted by the incoming proton. This allows

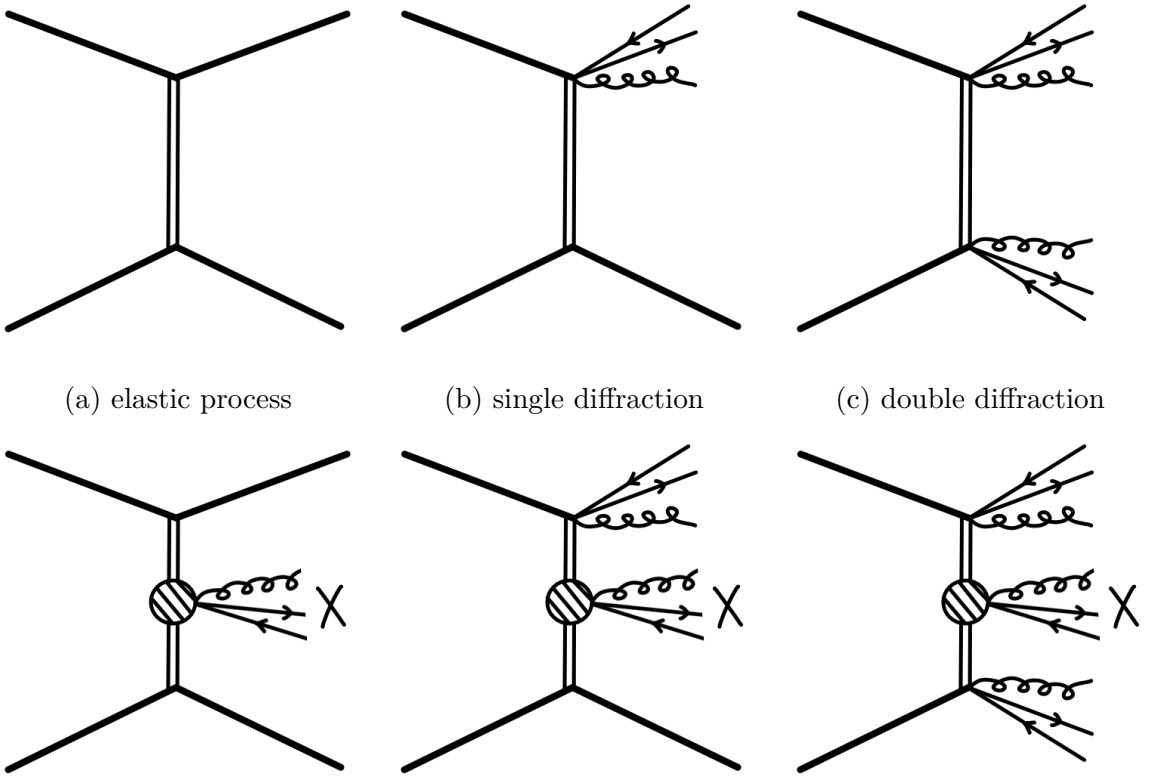

(a) elastic process (b) single diffraction (c) double diffraction

(d) central diffraction (e) central single diffraction (f) central double diffraction

Figure 1.17: Examples of elastic and diffractive processes. All of them involve the exchange of a pomeron, represented by two parallel lines. In elastic process (a) both protons survive and only the momentum transfer occurs between them. In single (b) and double (c) diffractive processes, the energy transfer occurs, which may lead to a dissociation of one or both protons. In central diffraction (d) the emitted pomerons interact with each other producing some central state X. It is also possible for one (e) or both (f) protons to dissociate in such process.

the proton to stay intact. The emitted pomeron becomes the source of the hard parton and recombines into pomeron remnants. The plot on the right shows areas populated by particles originating from the mentioned sources. Similarly to the non-diffractive case, there are central-state particles produced near rapidity zero and possibly overlapping with them those belonging to the pomeron remnant(s). There is also a large rapidity gap where no particles are produced and next to it there is a region populated by the intact forward proton.

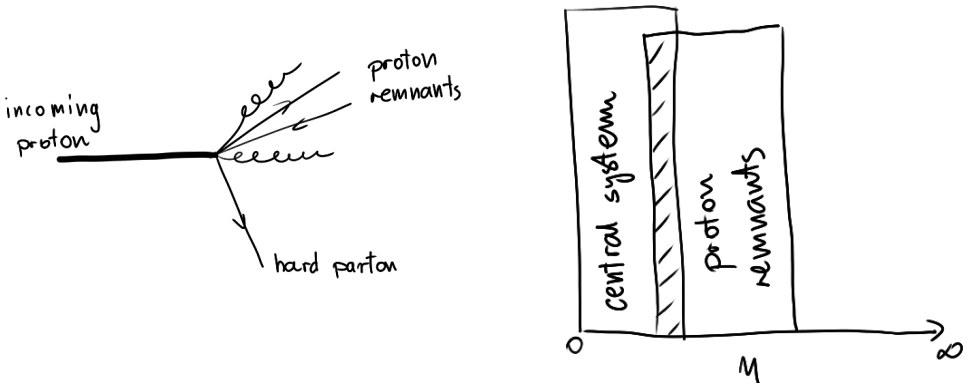

Figure 1.18: Partial diagram of the non-diffractive process (left). The incoming proton emits a hard parton, which participates in production of some central state. Proton breaks into a stream of particles (proton remnants). The plot (right) shows approximate regions in (pseudo)rapidity y/η space, where particles will be detected.

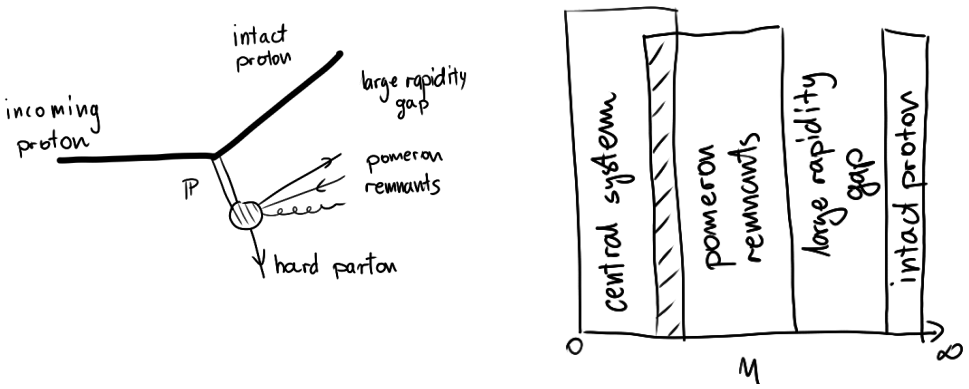

Figure 1.19: Partial diagram of the central diffractive process (left). the incoming proton emits a pomeron participating in central system production via hard parton. The rest of the pomeron recombines into stream of particles (pomeron remnants). Proton survives the interaction and is scattered at very low angle. The right plot shows approximate regions in pseudorapidity η space, where particles will be detected. Also the gap devoid of particles is presented.

1.6 Pythia event generator

The Pythia Monte Carlo plays an important role in many various studies in particle physics. At its basic form the model accommodates the leading order pQCD and successfully describes

the data at this level. It includes the Lund String Fragmentation mechanism [19]. It is also able to simulate the Underlying Event which mechanism was sketched in Sec. 1.4.

In Pythia, the total, elastic and inelastic cross-sections are obtained from the Regge fits to data. Currently, this is described by Donnachie and Landshoff [20] parameterisation providing:

$$\sigma_{tot}^{pp}(s) = (21.70 s^{0.0808} + 56.08 s^{0.4525}) \;\; mb, \tag{1.10}$$

where s in pp collision centre-of-mass energy squared, and the first and second term correspond to the pomeron and reggeon contributions, respectively. The elastic cross-section is given by:

$$\sigma_{el}^{pp}(s) = \frac{(\sigma_{tot}^{pp})^2}{16\pi B_{el}^{pp}(s)}, \tag{1.11}$$

where $B_{el}^{pp}(s) = 5 + 4s^{0.0808}$ is the pp elastic slope. In consequence the inelastic cross-section reads:

$$\sigma_{in}^{pp}(s) = \sigma_{tot}^{pp}(s) - \sigma_{el}^{pp}(s). \tag{1.12}$$

The inelastic cross-section can be broken into single diffractive (SD), double diffractive (DD), central diffractive (CD) and non-diffractive cross-sections. For single and double diffraction the parameterisation is given by Schuler and Sjöstrand [21]:

$$\frac{d\sigma_{SD}^{pp\to pX}(s)}{dt dM_X^2} = \frac{g_{3\mathbb{P}}}{16\pi}\frac{\beta_{p\mathbb{P}}^3}{M_X^2} F_{SD}(M_X) \exp(B_{SD}^{pX} t), \tag{1.13}$$

$$\frac{d\sigma_{DD}^{pp}(s)}{dt dM_1^2 dM_2^2} = \frac{g_{3\mathbb{P}}^2}{16\pi}\frac{\beta_{p\mathbb{P}}^2}{M_1^2 M_2^2} F_{DD}(M_1, M_2) \exp(B_{DD} t), \tag{1.14}$$

where M_X, M_1, M_2 are diffractive masses, $g_{3\mathbb{P}}$, $\beta_{p\mathbb{P}}$ are pomeron couplings, B_{SD}^{pX}, B_{DD} are diffractive slopes and F_{SD}, F_{DD} are the low-mass resonance-region enhancement and high-mass kinematical-limit suppression factors.

$$\sigma_{CD}(s) = \sigma_{CD}(s_{ref}) \left(\frac{\ln(0.06 \; s/s_0)}{\ln(0.06 \; s_{ref}/s_0)} \right)^{3/2}, \tag{1.15}$$

where $\sigma_{CD}(s_{ref})$ is reference CD cross-section at centre-of-mass energy of $\sqrt{s_{ref}} = 2$ TeV and $\sqrt{s_0} = 1$ GeV.

$$\frac{d\sigma_{CD}^{pp}(s)}{dt_1 dt_2 d\xi_1 d\xi_2} \propto \frac{1}{\xi_1 \xi_2} \exp(B_{SD}^{pX} t_1) \exp(B_{SD}^{Xp} t_2), \tag{1.16}$$

where ξ_1, ξ_2 are the fraction of the proton energy carried by the pomeron and related to the diffractive mass as $M_{CD} = \sqrt{\xi_1 \xi_2 s}$.

$$\sigma_{ND}^{pp}(s) = \sigma_{in}^{pp}(s) - \int \left(d\sigma_{SD}^{pp\to pX} + d\sigma_{SD}^{pp\to Xp} + d\sigma_{DD}^{pp} + d\sigma_{CD}(s) \right). \tag{1.17}$$

Non-diffractive event class is considered as a "norm", therefore is the most developed.

In single, double and central diffractive models, a pomeron is viewed as a glueball-like hadronic state. The pomeron flux defines the mass spectrum of the produced diffractive system. The internal structure is simulated as for the non-diffractive processes i.e., as a collision of a proton and a pomeron with partonic structures described by the respective parton distribution functions. The low-mass diffractive systems ($M_x < 10$ GeV) are assumed to exhibit no perturbative effects, thus are represented as non-perturbative hadronising strings, respecting the quantum numbers of the diffractively excited hadrons. In case of high-mass systems, the ISR and FSR effects are fully included and the additional Multi-Parton Interactions within the proton-pomeron system are allowed.

The generation of diffractive processes in Pythia is steered by a set of parameters which importance for the present studies is discussed in chapter 6.

Chapter 2

Experimental apparatus

2.1 Large Hadron Collider

The Large Hadron Collider (LHC) [22] is the world's largest and highest energy particle collider. It is situated at the European Organisation for Nuclear Research (CERN) near Geneva, Switzerland. It belongs to the CERN accelerator complex (Figure 2.1). It is located in a 27 km long tunnel where two beams, of protons or heavy ions, are accelerated and brought to collision at certain Interaction Points (IP).

The LHC beams are divided into bunches to match the time structure of the machine. A bunch contains about 10^{11} protons with a nominal energy of 6.5 TeV. The bunches collide at the rate of 40 MHz. However, for the accelerator safety and experimental reasons only 2808 out of 3564 bunches may be filled with particles. Various values of the centre-of-mass collision, $\sqrt{s}$, energy were achieved. The present work uses the data gathered in runs at $\sqrt{s} = 13$ TeV.

One of the most important parameters of a collider, besides the collision energy, is the instantaneous luminosity defined as:

$$L = \frac{N_a N_b f}{4\pi\sigma_x\sigma_y}, \tag{2.1}$$

where N_a and N_b are the numbers of protons in a bunch, $f = 11.245$ kHz is the LHC revolution frequency and σ_x and σ_y are the RMS sizes of the beams in the horizontal and vertical direction, respectively. This formula assumes a uniform population of bunches. The luminosity is also related to the rate of events of a given process, dN/dt, with the cross-section, σ, by

$$\frac{dN}{dt} = L \cdot \sigma. \tag{2.2}$$

The LHC was designed to achieve the instantaneous luminosity of $L = 10^{34}$ cm$^{-2}\cdot$ s^{-1} and in 2018 a peak value of $L = 2.1 \cdot 10^{34}$ cm$^{-2}\cdot$ s^{-1} was reached. The integrated luminosity is the luminosity delivered within a period of time:

$$L_{int} = \int L \cdot dt. \tag{2.3}$$

The integrated luminosity informs about amount of the collected data and is given in inverse barns.

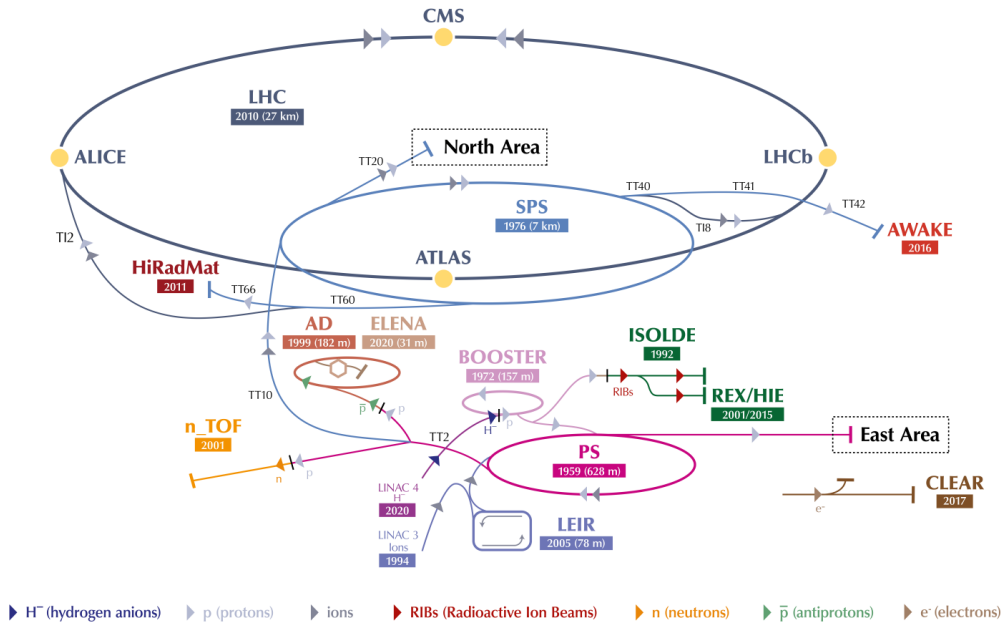

Figure 2.1: CERN accelerator complex. From [23].

Both beams undergo a complicated process of creation, bunching and acceleration before they are brought to a collision. It starts at the source of protons – a hydrogen bottle – goes through the Linac, Booster, PS, SPS accelerators. Eventually the bunches are injected into the LHC rings. At the LHC the beams are accelerated from 450 GeV to 6.5 TeV and after declaring the "*Stable beams*" conditions the experiments start to collect the data.

The beams are kept on their orbits by a system of superconducting and warm magnets. The optical properties of the beams are controlled by about 400 quadrupole magnets and the particles are accelerated using 8 radio frequency cavities per beam. An important part of the accelerator safety is the system of collimators protecting the machine and the experiments. The settings of the machine elements is called the LHC optics and it includes the parameters describing:

- dipoles: used to change direction of the beams
- quadrupoles: providing focusing/defocusing of the beams and matching of the beams' sizes at the IPs,
- higher-order-pole magnets: used to correct the beam properties,
- collimators: used to trim and shape the beam and to protect magnets and other equipment.

Four main experiments are located at the Interaction Points. These are:

- ATLAS (A Toroidal LHC ApparatuS) [24]: A general-purpose detector located at IP1 (Section 2.2).
- CMS (Compact Muon Solenoid) [25]: A general-purpose detector located at IP5. ATLAS and CMS are designed to crosscheck the measurements of each other.

- ALICE (A Large Ion Collider Experiment) [26]: Specialised detector located at IP8. Dedicated to the measurement of matter at extreme densities, e.g., quark-gluon plasma in heavy ion collisions.
- LHCb (Large Hadron Collider beauty) [27]: Specialised detector located at IP2. Dedicated to the study of the matter-anti-matter asymmetry via the measurement of the CP symmetry violation in the b quark sector.

2.2 ATLAS

ATLAS (A Toroidal LHC ApparatuS) [24] is one of two general-purpose detectors at the LHC. It is used to measure the final states of proton-proton, proton-ion and ion-ion collisions. It is located at the LHC IP1 and is the largest of the LHC experiments with the length of 46 m and 25 m diameter. Figure 2.2 shows the computer-generated image of the ATLAS detector with its major components.

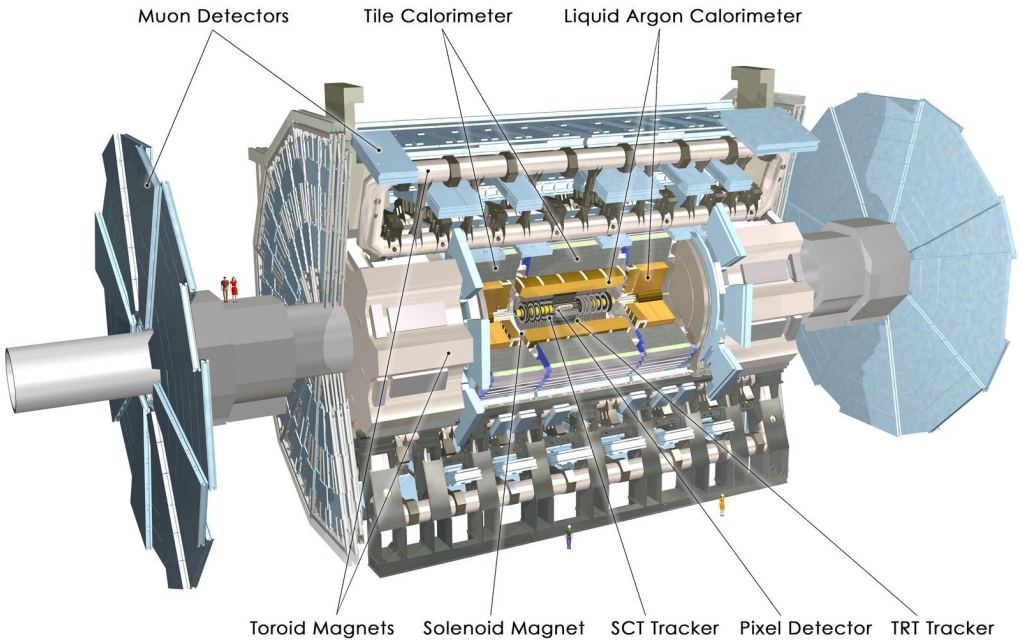

Figure 2.2: Computer generated image of the ATLAS detector. From [28].

ATLAS consists of three main detector systems:

- Inner Detector [29] (InDet) – dedicated to the measurement of charged particle tracks. This part of the ATLAS detector delivered the experimental data used in the following study and will be described in more detail in Section 2.2.1.
- Calorimeters [30] – designed to measure the energies of the final state particles. The system of calorimeters is divided into two distinct parts: electromagnetic (for the measurement of electrons and photons) and hadronic (for hadrons, e.g., protons, pions) calorimeters. Both types are build as sampling calorimenters with alternating active (the signal readout) and passive (particle absorbing) layers.
  - Liqud Argon (LAr) calorimeter [31] is an electromagnetic calorimeter, with liquid argon acting as an active medium and the absorber in the form of lead plates (the

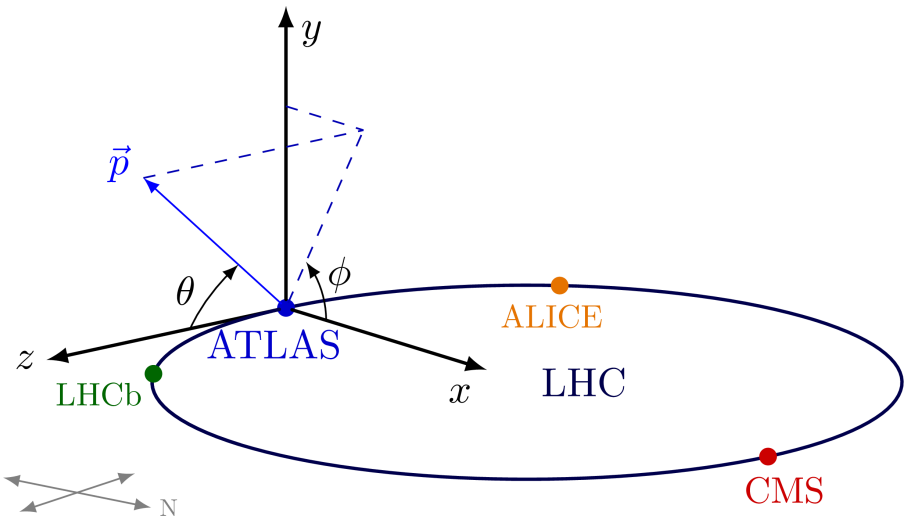

Figure 2.3: The ATLAS coordinate system. From [39]

energy resolution $\Delta E/E = 10\%/\sqrt{E(GeV)} \oplus 0.7\%$),

- Tile Calorimeter (TileCal) [32] – hadron calorimeter, with scintillators used to measure the energy deposited by particles and iron as a passive layers (the energy resolution $\Delta E/E = 52\%/\sqrt{E(GeV)} \oplus 5.7\%$ and $\Delta E/E = 50\%/\sqrt{E(GeV)} \oplus 3\%$ for single hadrons and jets respectively).

- Muon chambers [33] – designed to identify and measure the muon tracks and hence to determine their momenta and energies.

The ATLAS system of magnets [34] aids with the measurements. The solenoid magnet [35] allows determination of the transverse momentum and charge sign of a particle from the measurement of the particle track in the Inner Detector. The ATLAS toroidal magnets [36] support the measurements related to muons.

The *pp* interactions at the LHC create enormous amounts of data. To limit it and to record only interesting events, a system of triggers is used. It consists of a first-level hardware trigger (L1, LVL1 Trigger) [37] with trigger rate of 75 kHz, which feeds into a software trigger (HLT, High Level Trigger) [38] with rate of 2 kHz. More details in Section 2.2.4.

ATLAS Coordinate system:
The ATLAS experiment uses the right-hand coordinate system (cf. Figure 2.3), with z-axis following the beam coming from the LHCb experiment – beam1, x-axis pointing to the centre of the LHC, and y-axis pointing upwards. The origin of the system is the centre of the detector. The side with positive z-values is often called Side A, while the opposite one – Side C, which is in the beam2 direction. Very often the azimuthal angle φ and pseudorapidity η related to polar angle θ by:

$$\eta = -\ln(\tan\frac{\theta}{2}) \tag{2.4}$$

are used.

2.2.1 ATLAS Inner Detector

The main goal of the ATLAS Inner Detector [29] is the measurement and reconstruction of the charged particle tracks. It is located within the 2 T solenoidal magnetic field allowing for the measurement of the transverse momenta and determination of the charge sign of particles that pass through the detector. The Inner Detector is 6.2 m long and 2.1 m in diameter. It is composed of three subsystems: the pixel detector, the semiconductor tracker (SCT) and the transition radiation tracker (TRT). All subsystems are divided into three parts: barrel – cylindrically shaped trackers around the IP, and two end-caps – disk shaped trackers perpendicular to the beam axis placed on both ends of the barrel. Figure 2.4 presents an image of the ATLAS Inner Detector.

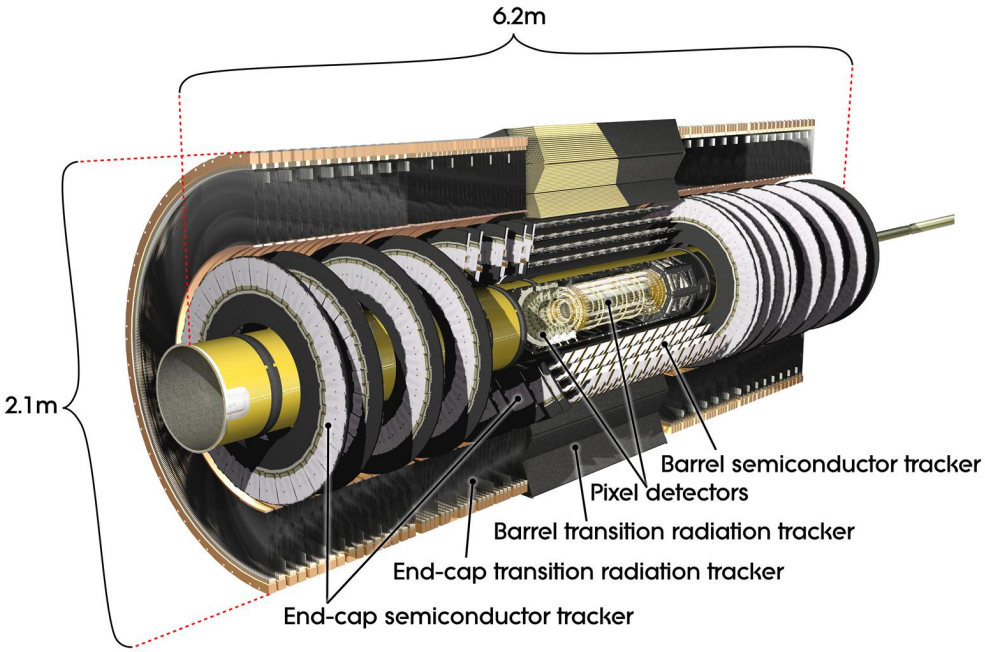

Figure 2.4: Computer generated image of the ATLAS inner detector. From [40]

Pixel Detector:
The pixel detector [41] is the ATLAS innermost tracker. The barrel and end-cap parts contain 92 million identically sized, 50x400 µm^2, silicon pixels. The barrel region has three tracking layers at the radii of 50.5 mm, 88.5 mm and 122.5 mm from the axis and covers the pseudorapidity range of $|\eta| < 1.4$. The end-cap has also three tracking layers at the distance of 495 mm, 580 mm and 650 mm from the detector centre ($z = 0$) and covers the pseudorapidity range of $1.4 < |\eta| < 2.5$. The total area of the active layer is 1.70 m^2. The precision of the track position measurement reaches 10 µm in the transverse and 115 µm in z direction. The main task of the Pixel Detector is a precise determination of the primary and secondary vertices, which is crucial for B-physics.

Semiconductor Tracker:
The semiconductor tracker [42–44] contains 4088 microstrip sensors. Each SCT module has two 63.56x63.96 mm^2 silicon sensors. The barrel region consists of four layers located at radii ranging from 299 mm to 514 mm. The end-cap modules contain nine active layers located at $|z|$ between 847.5 mm and 2727 mm. The total area of the active layers is 60 m^2. Similarly to the pixel detector, the barrel and end-caps cover the pseudorapidity range of $|\eta| < 1.4$ and

$1.4 < |\eta| < 2.5$, respectively. The precision of the track position measurement reaches 17 µm in the transverse and 580 µm in the z direction. The SCT main goal is to deliver information exploited by a precise tracking procedure.

Transition Radiation Tracker:
The transition radiation tracker [45,46] is the outermost part of the Inner Detector. It consists of total of more than 320 thousand, 4 mm in diameter kapton straws. The straws, serving as drift chambers, are filled with a Xeon-based active gas mixture (some channels use Argon). The length of the straw varies depending on region: for the barrel it is 144 cm with straws parallel to the beam axis, and the end-cap straws are 37 cm long and oriented radially with respect to the z axis. The TRT contains up to 73 layers of straws interleaved with fibres (barrel) and 160 straw planes interleaved with foils (end-cap), which provide transition radiation for electron identification. The barrel TRT is divided into three rings of 32 modules each with necessary support structures. The barrel radial layers are located at r between 559 mm and 1080 mm. The end-cap region consists of 18 disk-shaped segments, placed at $|z|$ ranging between 847.5 mm and 3403 mm. The charged particle tracks with the transverse momentum $p_T > 0.5$ GeV and $|\eta| < 2.0$ cross at least 36 straws, except for the barrel-end-cap transition region ($0.8 < |\eta| < 1.0$), where this number decreases to 22. The precision of the track position measurement reaches 130 µm. The TRT improves the tracking and its transition radiation features are used for the electron identification.

2.2.2 MBTS

Triggering on given types of events may introduce a bias to the recorded data sample. Therefore, there is a need for a trigger which introduces the least bias. In the ATLAS experiment such a trigger is delivered by the Minimum Bias Trigger Scintillators [47].

The MBTS detector is composed of 2 cm thick polistyrene scintillating disks, each divided into sixteen segments, installed symmetrically in the inner side of the end-cap calorimeter at $|z| =$ 3.56 m from ATLAS IP. Each disk is separated into the outer and inner ring covering $2.08 \leq |\eta| \leq 2.76$ and $2.76 < |\eta| < 3.86$ respectively. Light emitted in scintillators is collected by the wavelength-shifting optical fibers and guided to the photomultiplier tubes. PMTs measurements are then read out by the same electronics as the Tile Calorimeter. The Central Trigger Processor (CTP) combines the signal collected from all 32 MBTS segments and provides several trigger items, described in Section 2.2.4.

2.2.3 ATLAS Forward Proton

The ATLAS Forward Proton (AFP) [48] detectors are another sub-system of the ATLAS experiment. The AFP detectors are designed to measure the trajectories of the protons scattered at very low angles. For that reason, they have to be positioned at a significant distance from the collision point at locations where the scattered proton is well separated from the beam. Obviously, the detector positions were selected taking into account the LHC optics. The AFP general scheme is presented in Figure 2.5.

The AFP detector system consists of four stations, two on each side of the ATLAS IP between the fifth and sixth quadrupole magnet. The near and far stations are placed 205 m and 217 m away, respectively. Each station is equipped with four layers of 16.8x20 mm^2 silicon pixel sensors with an array of 80x360 pixels with a common name of the Silicon Tracker (SiT). SiT is capable of a precise measurement of the proton track position in the plane perpendicular to

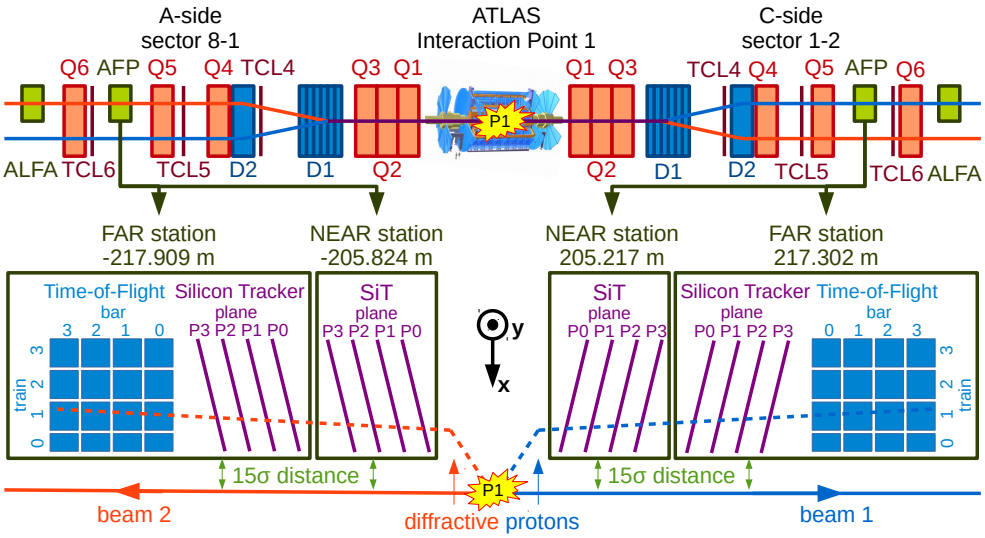

Figure 2.5: ATLAS Forward Proton general overview.

the beam axis. The spacial resolution is 6 µm and 30 µm in x and y direction, respectively [49]. Far stations are additionally equipped with the quartz Time-of-Flight (ToF) detectors. In case protons are registered in both far stations the difference of the ToF timing measurements allows determination of the interaction location, which is useful for the background rejection.Although the efficiency of the ToF detectors in LHC Run 2 was very low (∼5%), the timing resolution reached ∼30 ps [50]. The AFP detectors are capable of moving perpendicular to the beam due to the use of the Roman Pot (RP) technology [48]. This technology allows a precise positioning of the detectors in the immediate vicinity of the beams during the data taking periods and retracting them when the beams are unstable. In addition, the RPs separate the detectors from ultra-high vacuum of the accelerator. Figure 2.6 shows a sketch of the AFP far station.

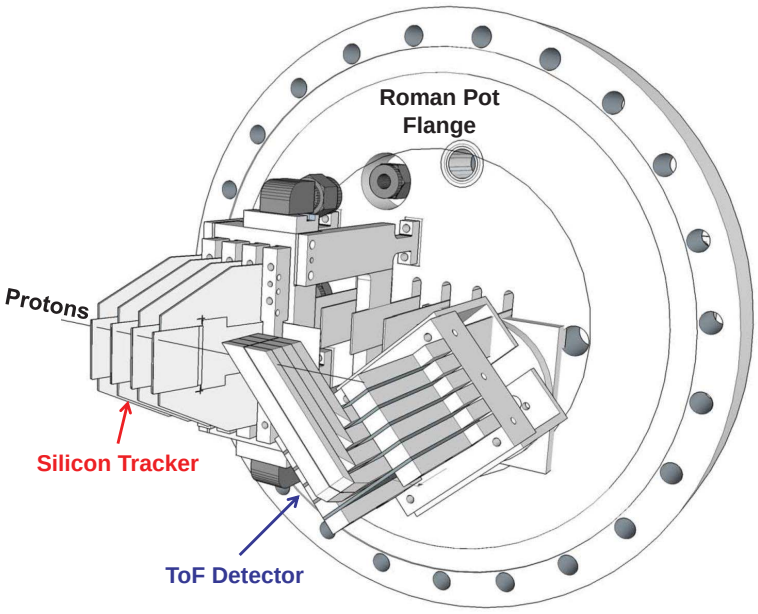

Figure 2.6: The ATLAS Forward Proton far station. From [48].

The AFP detectors can also provide a L1 trigger signal [51] which is based on the SiT. Three

planes out of four are used for the triggering and the trigger signal is generated when two out of these three planes fire. The trigger items provided by the AFP detectors are described in Section 2.2.4.

2.2.4 Trigger and Data Acquisition systems

The Data Acquisition System is used to read out fragmented data from ATLAS subsystems, combine them into full events, and store them for further off-line analysis. The DAQ is separated into two subsystems: Detector Readout and Data Flow. The DAQ system also provides tools for control and monitoring.

The Detector Readout constantly reads raw detector data at the rate of ∼1.7 MB per 25 ns or one bunch-crossing. Such data is buffered in Read Out Drivers (ROD) after L1 trigger decision and passed further into the Data Flow at the rate of ∼160 GB/s.

The Data Flow Readout System receives and buffers fragmented detector data from the RODs via 1800 independent read-out channels. The data are sent to the HLT farm upon request via the Data Collection Network. Atfer the LHC trigger the data rate is reduced to ∼3 GB/s and is stored off-site for further processing

The ATLAS Trigger system performs a two-stage selection process: L1 trigger and High Level Trigger. The triggering decision is based on information delivered by the ATLAS detector components.

LVL1 trigger:
The Level 1 trigger [37] is a purely hardware system. As an input, the L1 trigger uses outputs from the ATLAS subsystems, looks for certain patterns in the received signals and defines the regions of interest (RoI). The list of the L1 triggers is limited to 256 which are defined in the Central Trigger Processor [52]. The LVL1 trigger limits the data acquisition rate from the LHC nominal collision rate of 40 MHz to 100 kHz. Its latency is about 2 µs.

In this analysis, two ALTAS subsystems provide the L1 trigger information:

- MBTS – provides several L1 trigger items, however this analysis uses only one: `L1_MBTS_2` which requires at least two hits on the same MBTS side.
- AFP – this analysis uses the L1 trigger formed as a logical AND of both stations on same side, named as `L1_AFP_A` and `L1_AFP_C` for side A and C respectively. Such trigger items can be combined further as a logical OR forming `L1_AFP_A_OR_C` trigger.

High Level Trigger:
The HLT [38] is a purely software system. Originally it was formed from two subsystems: LVL2 trigger and Event Filter, which were merged into a single system in LHC Run-2. It operates from a large farm of about 40 thousand CPU cores. In around 200 µs per event, it conducts an analysis of RoI provided by the L1 trigger. The trigger rate is reduced from 100 kHz to approximately 1 kHz. The decision whether the event passes is delivered by dedicated algorithms. In about 1/10th of the HLT items an event is accepted unconditionally based on the L1 trigger decision. The remaining events left by the HLT are stored for future processing.

Trigger prescale:
One of the main tasks of the trigger system is the reduction of the amount of data. As mentioned above this is achieved using dedicated algorithms. In addition a mechanism of presecales is available. The prescale defines how often an event with a positive trigger decision

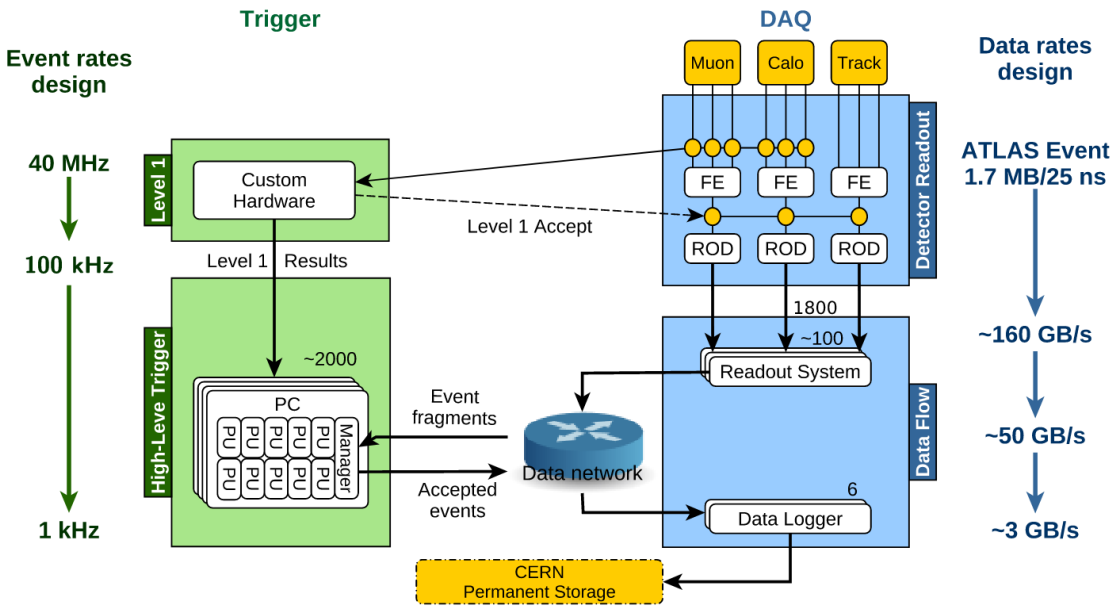

Figure 2.7: The dataflow of the ATLAS TDAQ system. From [53].

can be passed for further processing. This procedure is applied individually to each of the LVL1 and HLT triggers.

The Data Acquisition system form the TDAQ system together with the Trigger system. The data flow of the TDAQ system is presented in Figure 2.7

Analysis triggers:
This analysis uses both L1 and HLT trigger items:

- `HLT_noalg_L1AFP_A_OR_C` – consists of the L1 AFP trigger and no High-Level Trigger algorithm. The trigger is prescaled at the HLT level by 20 and has no prescale at L1.
- `HLT_noalg_L1MBTS_2` – consists of L1 MBTS trigger fired when Minimum Bias Trigger Scintillators detect the activity and no algorithm in the High-Level Trigger. The trigger is prescaled at the HLT level by 10 and at L1 by 150, giving total prescale equal to 1500.
- `HLT_mb_sptrk` – the Minimum Bias Space-track trigger. On the level one it accepts all events and at the HLT level it requires the Inner Detector signal.
- `L1_AFP_A` or `L1_AFP_C` – selects events on the given AFP side. These items are not used for recording any events but their decision is stored and can be used to find which AFP side trigger the `HLT_noalg_L1AFP_A_OR_C`.
- `L1_MBTS_2` – using information about the decision of this item will be used for evaluation of the `HLT_noalg_L1MBTS_2` efficiency.

The combinations of presented triggers are used to derive data samples of various roles in the presented analysis and are described in Section 4.1.

Chapter 3

Forward proton reconstruction

This chapter discusses the reconstruction of forward proton kinematics. It is based on the work of the author and is used in all analyses concerning the AFP data. An essential ingredient is the evaluation of the systematic uncertainties.

Section 3.1 introduces the kinematic variables used in the description of the forward proton and discusses the AFP geometrical acceptance. Section 3.2 describes the alignment of the AFP detectors. The reconstruction of the scattered proton kinematics is a two-step procedure. At the first stage the AFP SiT hits are reconstructed from the low-level detector information. This is done as a part of the off-line reconstruction procedure described in [54]. Next, the reconstructed hits are used in the on-fly reconstruction during the event analysis. This is a multi-step process. At first, the hits are used in the cluster reconstruction (Section 3.3). Next, the track reconstruction procedure is performed (Section 3.4). Finally, the tracks are used in the proton reconstruction (Section 3.5).

3.1 AFP geometrical acceptance

The forward proton can be described using two kinematic variables: its transverse momentum p_T and the relative energy loss ξ defined as:

$$\xi = 1 - \frac{E_{proton}}{E_{beam}}, \tag{3.1}$$

where E_{proton} is the energy of the AFP measured proton and E_{beam} is the nominal energy of the beam. The probability that a proton reaches the AFP detectors is called the geometric acceptance and is a function of the proton p_T, ξ as well as of the detector-beam distance and the LHC optics. It is obtained using Monte Carlo methods and is calculated as the ratio of the number of protons that reach the detector to the total number of protons generated within a given kinematics range. Figure 3.1 shows the acceptance of the Near AFP station on side C, for the nominal LHC optics. One should note that the acceptance depends also on the TCL4 and TCL5 collimators at which some protons my be lost.

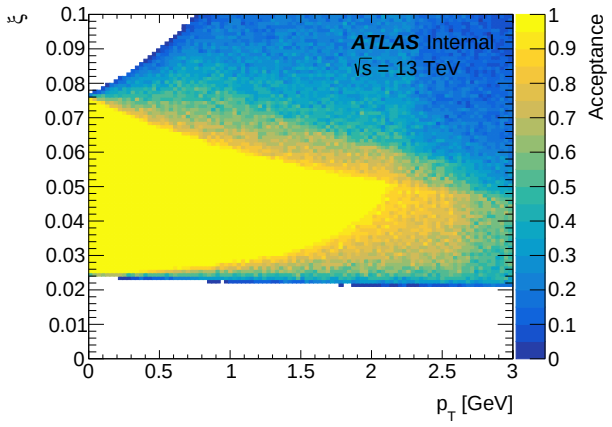

Figure 3.1: The geometric acceptance of the AFP near station for the nominal collision optics as a function of protons transverse momentum p_T and relative energy loss ξ.

3.2 Alignment of the AFP detectors

Proper kinematic reconstruction of the forward proton requires knowledge of the detector position with respect to the centre of the proton beam. In case of the AFP detectors two alignment levels can be singled out. Namely, the inter-plane and global alignments.

Global alignment: The AFP global alignment defines the position of a SiT sensor along the x-axis, e.g., the position of the edge of the sensor. It has three ingredients (see Fig. 3.2):

- $\Delta_{tracker}$ – the distance between the sensor edge and the exterior floor of the Roman Pot. It is assumed to be constant and its value is 500 µm and follows from the experimental set-up construction.

- Δ_{RP} – the distance between the Roman Pot exterior floor and the centre of the beam pipe. This value taken from the step motor readings.

- Δ_{beam} – the position of the centre of the beam with respect to the beam pipe axis. Its value is obtained during the beam-based alignment procedure [55].

Inter-plane alignment: The inter-plane alignment is defined as a displacement and rotation of a SiT plane with respect to the first SiT layer. The alignment method defines three parameters per plane. These are Δx and Δy – being the offsets in the (x, y) plane and α – the angle of rotation around the z-axis.

Systematics:
There are two possible sources of the alignment systematic uncertainty. The first one is related to the local alignment – due to a possible rotation of the detector planes during the SiT package assembly or its insertion into a Roman Pot, a counterclockwise rotation of the planes along beam axis by 4 mrad.

The second one is related to the global alignment, which comes from the uncertainty of the BBA alignment procedure and the corrections obtained in the analysis of the AFP tagged exclusive production of lepton pairs [56]. A ±300 µm shift along the x-axis is considered.

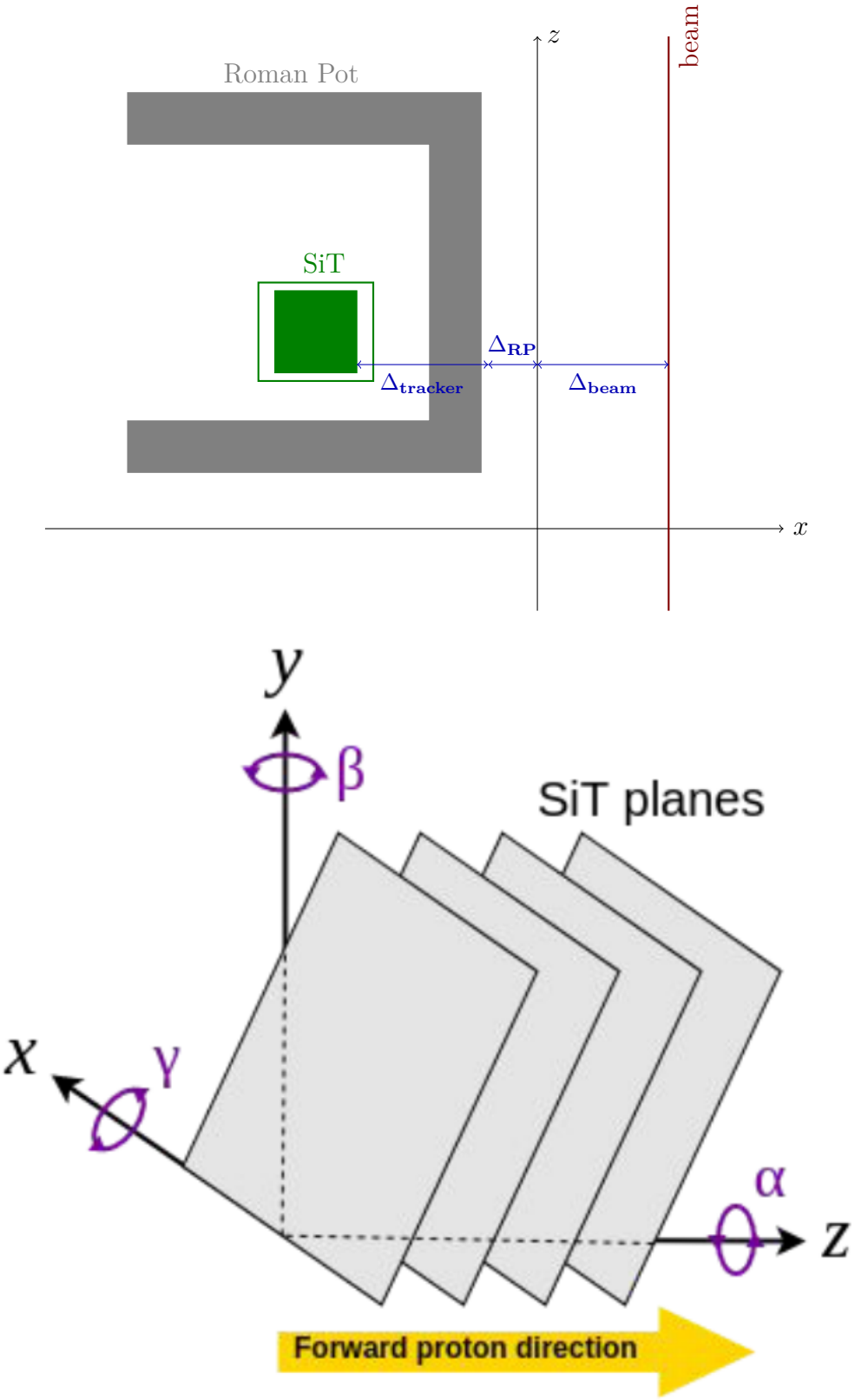

Figure 3.2: Parameters of the AFP global (upper) and inter-plane (lower) alignment.

3.3 Cluster reconstruction

The cluster reconstruction process, called "clusterisation", groups neighbouring pixel hits into a cluster. This operation is performed for each pixel layer of each AFP station independently.

The cluster reconstruction process starts with a first free, i.e. not associated with any cluster, pixel hit which is taken as the cluster seed. Next, a search for all pixels neighbouring the seed is performed along the seed (pixel) long edge, i.e. in the x-direction. If a neighbouring pixel is found it is added to a cluster. The procedure is repeated until there are no more neighbouring pixels. Eventually, the cluster position is calculated as the deposited charge-weighted average position of the centres of the associated pixels. It should be noted that the cluster position is calculated with respect to the edge of the sensor. This is corrected by applying the inter-plane alignment.

Taking into account the pixel layer geometry it is expected that the number of hits belonging to a cluster is between one and three [49]. This can be checked by inspecting the hit multiplicity distributions for few chosen SiT layers presented in Fig. 3.3. As expected in majority cases a cluster contains 1 to 3 pixels. However, it is possible to form a cluster consisting of a large number of pixels. Such clusters may be due to particle showering in the detector or the Roman Pot material.

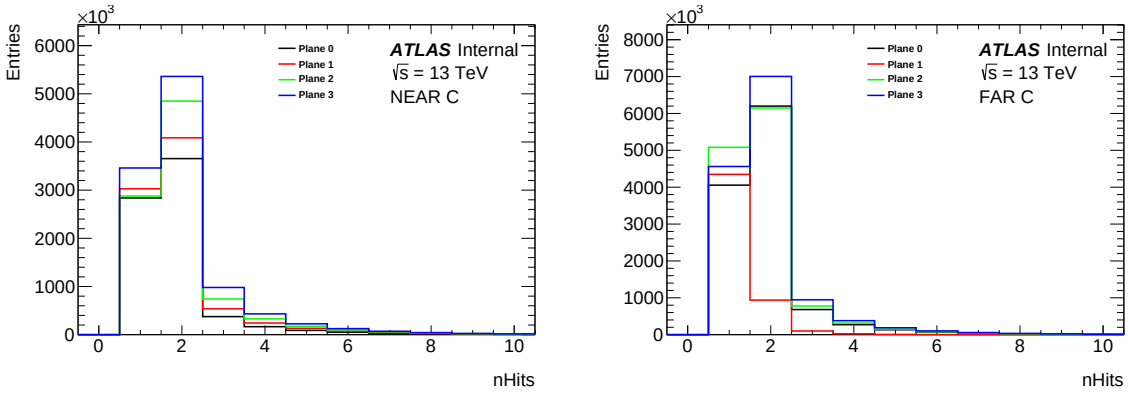

Figure 3.3: Hit multiplicity in cluster for near (left) and far (right) station on side C.

Systematics:
To estimate systematic uncertainty on the alignment parameters another neighbourhood of a cluster seed is considered. Namely, a search for neighbouring pixels is performed in both directions i.e. along both x and y axes. Obviously, this influences the cluster position along y. However, this change is rather minor and partially included in the track reconstruction algorithm.

3.4 Track reconstruction

The track reconstruction process is divided into two steps:

- track finding algorithm searching for the track candidates,
- reconstruction of the track properties, discarding low quality ones and calculating parameters of the accepted track candidates.

This procedure is applied independently for each AFP station.

3.4.1 Track finding algorithm

The procedure of finding track candidates is similar to the clustering algorithm. However, it creates clusters of clusters. These super-clusters are formed from the clusters belonging to all SiT layers of a given station if the distance between their centres in the (x, y) plane does not exceed 0.5 mm. Such super-clusters, called now the track candidates, are passed to the parameters reconstruction algorithm. The reason of the effectiveness of such a simple algorithm is the fact that the measured protons are almost parallel to the beam.

Systematics:
This procedure experiences similar systematics as the clustering algorithm. It is possible to create a track candidate consisting of dozens of clusters if a particle shower was formed or multiple proton tracks were registered within the detector. Therefore, the maximum distance between the cluster centres can be set to 1 mm, in order to estimate such effects.

3.4.2 Reconstruction of the track parameters

At first, the signature of track candidates is checked. Each candidate is required to have associated clusters in at least two different layers of the SiT. Next, the candidate positions and slopes in the x and y directions are calculated applying linear regression to the centres of the clusters. One should observe that the track positions are calculated with respect to the edge of the first pixel sensor. This is corrected by applying the global alignment (see Section 3.2).

Systematics:
To study the systematic effects one can use a different cluster-layer requirement. The track candidates are required to have exactly one cluster per a pixel layer and at least two clusters in total. Additionally, the minimum number of layers with identified associated clusters can be changed from two to three[1].

3.5 Proton reconstruction

Properties of the protons registered by the AFP are found using the reconstructed tracks. The procedure requires the knowledge of both the used machine optics and the detector alignment.

3.5.1 Optics and transport simulation

In the reconstruction procedure, information about the LHC optics is held in a form of the proton transport parametrisation proposed in [57]. The parameterisation is based on the proton transport calculations performed using specialised codes (e.g. MAD-X [58]). It allows calculation of the scattered proton trajectory position and slopes at a given distance from the IP. In the present case the location of the near AFP station was chosen. An extrapolation of the proton trajectory to the location of the far station is straightforward since no LHC magnetic elements are present between the two stations. Each parameterisation has the following form:

$$\begin{aligned} \alpha_{AFP} = {} & A_\alpha(\xi) + B_\alpha(\xi)x_0 + C_\alpha(\xi)y_0 + D_\alpha(\xi)z_0 \\ & + E_\alpha(\xi)x_0^{'} + F_\alpha(\xi)y_0^{'} + G_\alpha(\xi)z_0x_0^{'} + H_\alpha(\xi)z_0y_0^{'} \end{aligned} \tag{3.2}$$

[1]In fact, the requirement of only two planes is a consequence of the technical problems experienced by one of the Silicon Trackers on the A-side during the considered data taking period.

where α is either the horizontal or vertical proton position or slope (x_{AFP}, y_{AFP}, x'_{AFP}, y'_{AFP}, respectively), $A_\alpha \cdots H_\alpha$ are various order polynomials in ξ, (x_0, y_0, z_0) denote the initial position of a proton (the interaction vertex coordinates) and (x'_0, y'_0) are the initial slopes of the scattered proton trajectory.

From the proton transport simulations, it follows that the x_{AFP} and x'_{AFP} do not depend on y_0 and y'_0. This reflects a negligible role of the sextupole and higher order magnetic fields in the LHC optics between the ATLAS IP and the AFP stations. Taking the above into account, the polynomials C_y, F_y, H_y or B_x, E_x, G_x can be set to zero in calculation of the horizontal and vertical components, respectively, leading to:

$$x_{AFP} = A_x(\xi) + B_x(\xi)x_0 + D_x(\xi)z_0 + E_x(\xi)x'_0 + G_x(\xi)z_0x'_0, \tag{3.3}$$

$$y_{AFP} = A_y(\xi) + C_y(\xi)y_0 + D_y(\xi)z_0 + F_y(\xi)y'_0 + H_y(\xi)z_0y'_0. \tag{3.4}$$

The parameterisation file [59] stores the coefficients of the polynomials, as well as their orders, the distance for which the parameterisation was calculated, the crossing angles, etc.

Systematics:
For the systematic checks, two additional parameterisation files were prepared. They were obtained assuming a modification of the beam initial angle in the horizontal direction by ±50 µrad, which reflects the optics uncertainty.

3.5.2 Proton kinematics reconstruction

The proton kinematics reconstruction is performed for each side independently. The first step is to find a pair of tracks, one in the NEAR and one in the FAR station. The distance between these tracks, projected onto the (x, y)-plane can not exceed 2 mm. This requirement follows from the expected low angles of the signal protons and discriminates most of the pairs left by different protons hitting the stations. It is possible for a single track to be matched with more than one track in the other station. In such a case additional protons may be reconstructed. Another possibility is the proton kinematics reconstruction using only a single station, but then only information about the proton relative energy loss can be retrieved. This option is not used in the present analysis.

There are two possible reconstruction methods: "analytical" – uses parameterisation directly and "minimization" – uses either parameterisation or transport software by minimizing χ^2 function.

Analytical method:
This method uses parameterisation equations. Starting from Equation 3.3 for the horizontal position and slope components:

$$\begin{cases} x_{AFP} &= A_x(\xi) + B_x(\xi)x_0 + D_x(\xi)z_0 + E_x(\xi)x'_0 + G_x(\xi)z_0x'_0 \\ x'_{AFP} &= A_{x'}(\xi) + B_{x'}(\xi)x_0 + D_{x'}(\xi)z_0 + E_{x'}(\xi)x'_0 + G_{x'}(\xi)z_0x'_0, \end{cases} \tag{3.5}$$

where x_{AFP} and x'_{AFP} are the horizontal position and slopes[2] calculated from the reconstructed

[2]Experimentally it is measured as $(x_{FAR} - x_{NEAR})/d$, where d is the distance between the stations.

tracks, x_0 and z_0 are the coordinates of the interaction vertex position, ξ and $x_0^{'}$ are the unknown relative energy loss of a proton and its slope at the IP.

From Eqs. 3.5 one can derive $x_0^{'}$:

$$\begin{cases} x_0^{'} & = \dfrac{x_{AFP} - A_x(\xi) - B_x(\xi)x_0 - D_x(\xi)z_0}{E_x(\xi) + G_x(\xi)z_0} \\ x_0^{'} & = \dfrac{x_{AFP}^{'} - A_{x'}(\xi) - B_{x'}(\xi)x_0 - D_{x'}(\xi)z_0}{E_{x'}(\xi) + G_{x'}(\xi)z_0} \end{cases} \tag{3.6}$$

and then subtracting one equation from the other one gets:

$$\begin{aligned} &(x_{AFP} - A_x(\xi) - B_x(\xi)x_0 - D_x(\xi)z_0)(E_{x'}(\xi) + G_{x'}(\xi)z_0) - \\ &(x_{AFP}^{'} - A_{x'}(\xi) - B_{x'}(\xi)x_0 - D_{x'}(\xi)z_0)(E_x(\xi) + G_x(\xi)z_0) = 0. \end{aligned} \tag{3.7}$$

Next, this equation is solved for the relative energy loss ξ using the bisection method. The resulting ξ value can be inserted into Eq. 3.6 to obtain the initial horizontal (and vertical) slopes. Eventually, the proton four-momentum is calculated using ξ, $x_0^{'}$ and $y_0^{'}$ values.

Systematics:
Track pair selection may be stricter by changing the maximum distance to 1 mm.

3.6 Fast AFP simulation

An experimental analysis typically involves the use of Monte Carlo simulated events which have undergone a full simulation of the detector apparatus. However, in the case of the AFP detectors, full simulation is impractical and fast AFP simulation is used.

This procedure is performed for ATLAS fully simulated Monte Carlo samples containing information about the truth level (interaction final state level) particles. For each final state proton with sufficient energy to have a chance of reaching AFP (with ξ smaller than 0.3), the scattered proton momentum is smeared with the angular spread of the beams and its transport through the LHC lattice is simulated. If a particle hits the detector, the Gaussian smearing of the position with experimental spatial resolutions is applied. Next, the simulated data undergo the same reconstruction chain as the real ones, however, starting from the reconstructed track level.

Figure 3.4 shows a correlation between the true and reconstructed values of the relative energy loss ξ. As can be seen from the figure those two values are very strongly correlated, which confirms the correctness of the reconstruction procedure.

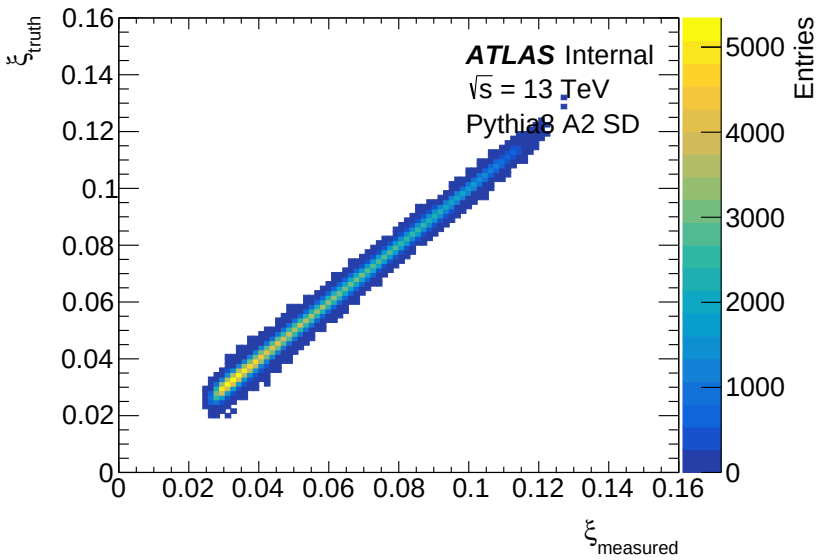

Figure 3.4: Correlation of the true and reconstructed value of the relative energy loss ξ.

Chapter 4

Data analysis

The goal of the present analysis is to study the MPI phenomenon in diffractive events. The first step is the measurement of UE-sensitive observables in events with a forward proton measured in the AFP detectors. Following the previous UE analyses performed within ATLAS, these observables are based on charged particle tracks registered by the ATLAS ID. The analysis uses data collected during a special LHC run at $\sqrt{s} = 13$ TeV (ATLAS run nr. 336505) with a very low average number of interactions per bunch crossing, $\mu \sim 0.04$.

The measurement is performed for three distinct regions. The discussed regions are defined with respect to the direction of the track with the highest transverse momentum (the leading track) considering the difference of the azimuthal angles:

$$\Delta\varphi = \varphi_{leading} - \varphi_{track}.$$

The regions are defined as:

- $|\Delta\varphi| < 60°$– towards,
- $60° < |\Delta\varphi| < 120°$– transverse,
- $|\Delta\varphi| > 120°$– away.

This is illustrated in Figure 4.1. The three regions have different sensitivities to the effects of the UE, with the towards and away regions being the least sensitive because of the activity of the leading and recoiling jet respectively, leaving transverse region the most sensitive. Additionally, the transverse region is split further into more and less active sides named transMax and transMin regions respectively. The transMin region is relatively insensitive to wide-angle emmisions from the hard process. The difference between transMax and transMin, named as transDiff, represents the effects of the hard process contribution to the transverse region.

The variables of interest are:

- mean number of charged tracks per unit of $\eta\varphi$, $\langle n_{trk}/\delta\eta\delta\varphi\rangle$,
- mean p_T sum of charged tracks per unit of $\eta\varphi$, $\langle \Sigma p_T/\delta\eta\delta\varphi\rangle$,
- mean per-event average p_T of charged particles, $\langle$mean $p_T\rangle$.

Section 4.1 describes the event and track selection criteria and sample types used in the present analysis. The collected data needs to be corrected for the detector inefficiencies. Data correction

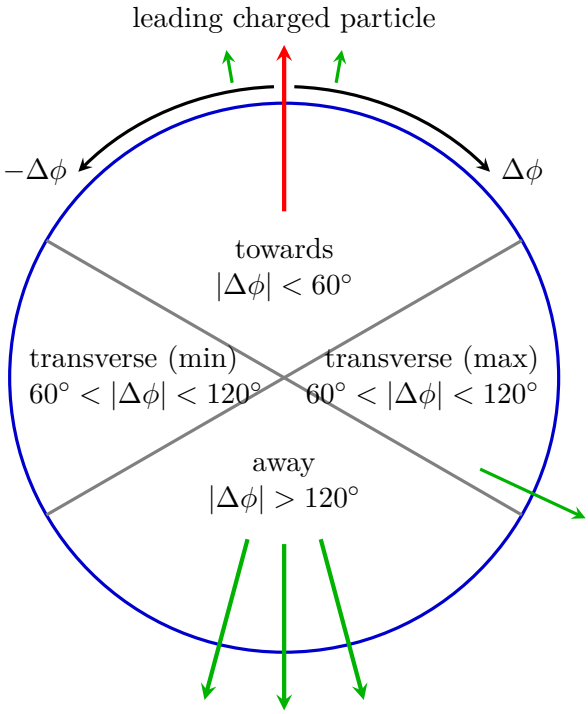

Figure 4.1: Definition of regions in the azimuthal angle space with respect to the leading charged particle track.

procedure is described in Section 4.2. The corrections include the ones related to the central detector: track (Section 4.2.1) and vertex (Section 4.2.2) reconstruction efficiencies, and the AFP trigger efficiency (Section 4.2.3). The dominant background is due to the non-diffractive processes and its estimation is described in Section 4.3. Also, the background related to the vertex reconstruction algorithm is discussed.

4.1 Data preparation

The experimental data selection procedure is divided into two steps:

1. Pre-selection is build around the main trigger for a given sample. The aim is to reduce the sample size by changing the data format. This is essentially only a technical step, performed to reduce the computing resources needed for the rest of the analysis. It includes most of the track selection – Section 4.1.1.

2. Final selection. Performed during the proper analysis and exploiting the auxiliary triggers – Section 4.1.2.

Datasets: In this analysis, two main types of data samples are used:

- The experimental data from the ATLAS dataset labelled as `data17_13TeV.00336505.physics_MinBias.merge.AOD.f935_m1992`.
  This sample was used to derive all analysed datasets referred to with a generic name "Data".

- The Monte Carlo samples from the datasets:
  `mc15_13TeV.361204.Pythia8_A2_MSTW2008LO_SD_minbias.merge.AOD`.

e3639_s2601_s2132_r6616_r6264/,
mc15_13TeV.361203.Pythia8_A2_MSTW2008LO_ND_minbias.merge.AOD.
e3639_s2601_s2132_r6616_r6264/.
The MC samples were generated using Pythia 8 A2 tune [60] with MSTW2008LO PDF set [7]. These samples contain single diffractive dissociation (SD) or non-diffractive (ND) events. The ND sample is used only for the track efficiency calculations (Section 4.2.1).

Data formats: Two different data formats are used in the analysis:

- xAOD (Analysis Object Data) – the default data storing format for both the experimental and Monte Carlo data used by the ATLAS Collaboration. It contains a reduced sized output of the physics quantities from the reconstruction. This includes the Inner Detector tracks and the AFP hits but also many more physics objects which are not used in the present analysis. To work with the xAOD data samples the use of a dedicated ATLAS framework – Athena [61] – is required. Such data were used as an input in the pre-selection.
- ntuple – the ROOT format [62]. Such files can be easily analysed without the need for installation of the Athena framework.

4.1.1 Initial data selection

The initial selection was performed within the Athena framework using the xAOD sample. The purpose of this step was the event and track selection and storing the data required at the next analysis steps in the ntuple data format. This drastically reduced the size of the sample and allowed the use of a dedicated code enabling a faster processing of the data during the analysis development.

Event selection: The events were selected in a two-step procedure. At first, an event was required to belong to the stable data taking period of the run and with constant trigger prescales. Such a period is defined requiring that the proton beams are stable and the detectors are able to record the physics data. From the ATLAS detector point of view, such a period is divided in the so-called *lumiblocks* lasting for about 60 second. For the analysed run the considered lumiblock range is 248–453. At the second step the trigger conditions were checked. In the present analysis, three main triggers were used to obtain three different event samples:

- `HLT_noalg_L1AFP_A_OR_C` (prescale = 20):
  The samples derived from this one are the main signal sample, but also are used to estimate one of the background types, corrections to the background model and reconstruction efficiencies.
- `HLT_noalg_L1MBTS_2` (prescale = 1500):
  The samples derived from this one are the main background samples.
- `HLT_mb_sptrk` (prescale = 5):
  The samples derived from this one are used as corrections to the background model.

Later, the sample will be checked for the response of the auxiliary L1 triggers: `L1_AFP_C`, `L1_AFP_A`, `L1_MBTS_2`. At this point this information is not needed and is stored for use in the next selection step. Numbers of events in the selected samples are presented in Table 4.1. For the Monte Carlo events, since they do not include lumiblocks or triggers, the initial event selection is omitted.

Table 4.1: The number of events selected by each trigger.

Trigger	Number of events
HLT_noalg_L1AFP_A_OR_C	6 383 128
HLT_noalg_L1MBTS_2	4 147 731
HLT_mb_sptrk	420 887

Track selection: The tracks were required to fulfil the standard ATLAS selection criteria [63]:

- transverse momentum, $p_T > 500$ MeV,
- pseudorapidity, $|\eta| < 2.5$,
- transverse impact parameter, $|d_0| < 1.5$ mm,
- at least one hit in the ATLAS Pixel detector,
- at least six hits in the SCT detector.

Results concerning the track selection procedure are presented in Appendix A and Table A.1. Typically, the ATLAS track selection also includes a cut on the longitudinal impact parameter $z_0 \cdot \sin\theta$. This condition was not applied here in order to preserve the tracks not associated with the interaction vertex for later steps of the analysis.

In case of the Monte Carlo samples, the selection follows the same path as for the reconstructed tracks (detector level). However, MC sample contains also the truth-level information about the produced particles. The selection of these particles was similar to the track selection: only the charged and stable particles were considered and they had to pass the same kinematic cuts on the transverse momentum and the pseudorapidity of the tracks. The stable particles are defined with lifetime is either infinite or large enough to not decay within the detector (e.g. neutron).

4.1.2 Final data selection

This selection step is performed during the proper analysis. The event selection steps are listed below.

- auxiliary trigger selection[1],
- 1 or 2 interaction vertices[1],
- 1 proton on a triggered side of the AFP with the relative energy loss $\xi \in [0.035, 0.080]$[1],
- at least one charged track,
- at most 50 tracks – higher multiplicities are dominated by background.
- leading track transverse momentum $p_T^{lead} > 1$ GeV.

The first three steps of the selection procedure depend on the actually processed sample and on the aim of the resulting sample. See Fig. 4.2 for the overview of the sample selection. The auxiliary trigger selection uses the Level 1 trigger response. One sample was prepared demanding the presence of exactly two reconstructed vertices and was used for the related

[1]The selection details depend on the future sample purpose.

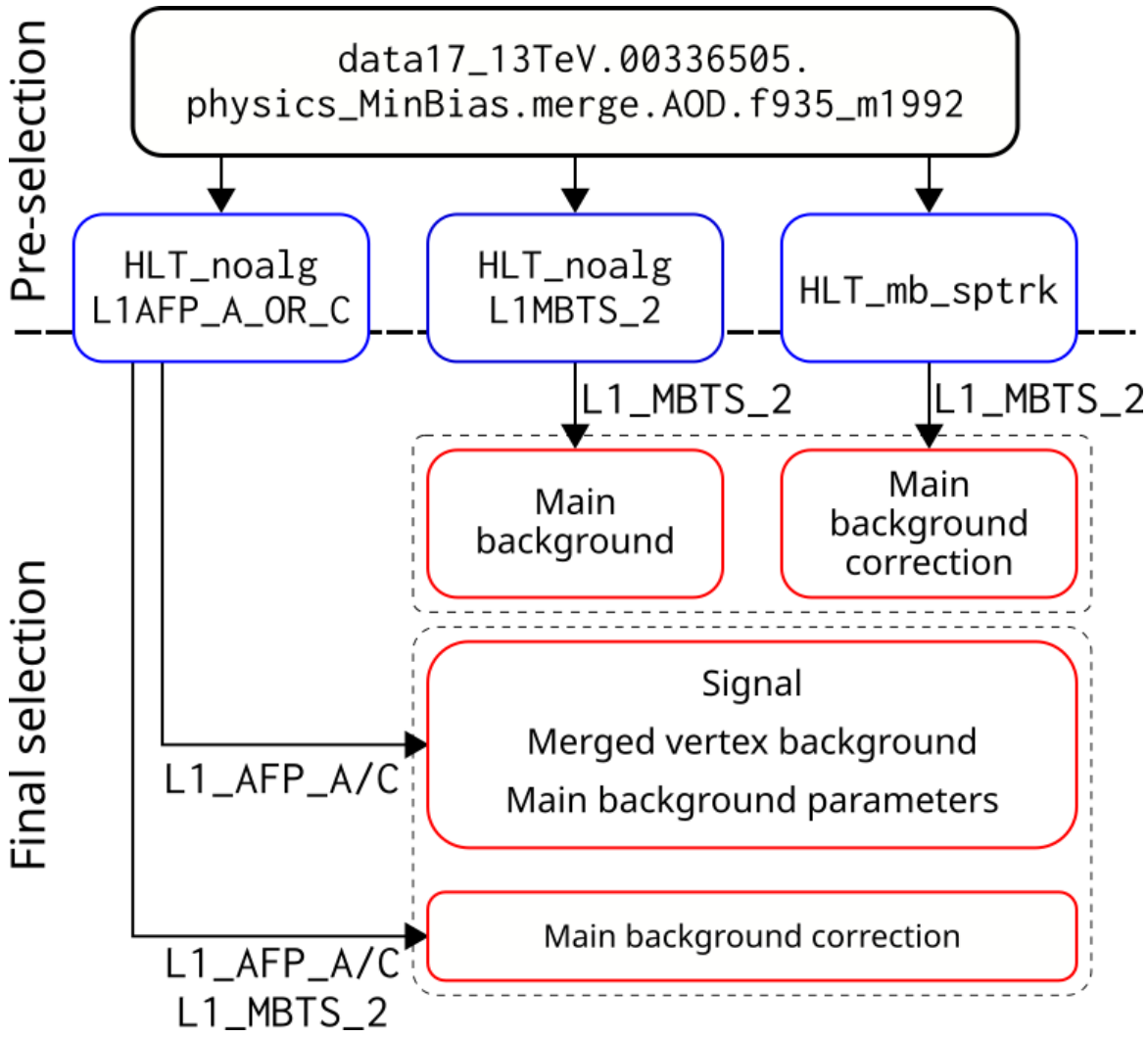

Figure 4.2: Diagram representing the trigger selection for each data sample used in the analysis. Samples mentioned in blue boxes are the results of the pre-selection for the High-Level trigger. The sub-samples in red boxes are derived at the final selection step after the checks of auxiliary triggers, the event and tracks selection.

background studies. For all other samples the presence of exactly one reconstructed vertex is required. The upper limit on the number of tracks was not present in the non-diffractive analysis, however in the previous AFP analysis [64] it was found that for tracks multiplicities $n_{trk} > 50$, the background dominates the sample.

`HLT_noalg_L1AFP_A_OR_C` samples:
From this sample eight (four for each side) different sub-samples are obtained, including:

- **The signal sample** contains the experimental data used for the main measurement. It is also used in the background correction procedure. The trigger selection includes the checks of the `L1_AFP_A` or `L1_AFP_C` trigger bits. Such sample is referred to as "AfpA" or "AfpC". Table A.2 shows results of the selection for the AfpC sample. The cuts with the strongest impact are those concerning: the trigger and vertex selection, the proton energy, and p_T^{lead}.

- **Merged vertex background sample** is derived to estimate one of the background

sources. For the details of the correction procedure consult Section 4.3.4. The trigger selection involves either the `L1_AFP_A` or `L1_AFP_C` trigger bits. This sample is the only one which requires the presence of two reconstructed vertices in an event. The sample is referred to as "MergedVertexBkgA" or "MergedVertexBkgC".

- **Background parameter sample** is constructed to calculate parameters of the combinatorial background model. The selection criteria are following those used to derive the AfpA or AfpC samples except for the upper limit of the track multiplicity and the leading track transverse momentum (see Sec. 4.3.1). This sample is referred to as "BkgParametersA" or "BkgParametersC".
- **Background correction sample** contains events that pass the selection criteria of the AfpA or AfpC samples and an additional requirement of the `L1_MBTS_2` trigger (Sec. 4.3.1). This sample is referred to as "AfpMbtsA" or "AfpMbtsC".

`HLT_noalg_L1MBTS_2` sample:
It is a source of the experimental data used to construct the main background sample which is central to the calculation of the parameters of the combinatorial background model (Sec. 4.3.1). The selection requirements are similar to those applied to select the Afp samples with the replacement of the L1 AFP triggers by the `L1_MBTS_2` trigger. Since in this sample the AFP is not of concern the presence of the scattered proton is not demanded. The sample is referred to as "Mbts".

`HLT_mb_sptrk` sample:
From this sample two new samples are obtained and both are used to devise the corrections to the combinatorial background model (Sec. 4.3.1). The first sample has no additional requirements on the trigger, so it relies exclusively on the `HLT_mb_sptrk` trigger. It is referred to as "Sptrk". The second sample embeds an additional requirement on the L1 MBTS trigger: `L1_MBTS_2` and is referred to as "SptrkMbts". Both samples do not require the presence of the scattered proton.

The Monte Carlo generated data can be treated in two ways. In the case of the fully simulated Monte Carlo, the resulting data have to undergo a path identical to that of the experimental data except for the AFP trigger requirement. For the truth level Monte Carlo, the analysis is similar to that of the data samples, but instead of tracks, the particles are used. This sample is compared to the unfolded data.

4.2 Efficiencies

In order to compare the measured distributions and the Monte Carlo model predictions at the particle level, the observables need to be corrected for the detector inefficiencies. These include the tracking (Sec. 4.2.1), vertexing (Sec. 4.2.2) and AFP trigger (Sec. 4.2.3) and are discussed below.

4.2.1 Track reconstruction

Few factors contribute to the track reconstruction efficiency: the track reconstruction inefficiency, fraction of fake tracks, the out-of-kinematic-range tracks and the charged strange baryon fractions. All these contributions are calculated using the Pythia 8 A2 non-diffractive events. The reason behind the use of non-diffractive sample is that the detector reconstruction efficien-

cies are process independent and in case of non-diffractive sample the number of tracks passing the track and vertex selection criteria is much greater, thus resulting in more precise efficiency calculation.

Track reconstruction efficiency

$$\epsilon_{trk}(\eta, p_T) = \frac{N_{reco}^{matched}(\eta, p_T)}{N_{gen}(\eta, p_T)} \tag{4.1}$$

is defined as the ratio of the number of charged particles with matched [65] reconstructed tracks, $N_{reco}^{matched}$, to the charged particle multiplicity, N_{gen}, in a given η or p_T range. All particles are required to pass the selection criteria (Sec. 4.1.1). The track reconstruction efficiency distribution is presented in Figure 4.3 (left).

For the centrally produced tracks the reconstruction efficiency is close to 95%. It decreases to $\sim 70\%$ with $|\eta|$ increasing to 2.5. The track reconstruction efficiency slowly grows with p_T from 74% to 88% with p_T increasing from 500 MeV to 30 GeV. However, one should note that the shape of the p_T distribution results in larger uncertainties on $\epsilon_{trk}(\eta, p_T)$ for large p_T-values.

Fraction of fake tracks

$$f_{fake}(\eta, p_T) = \frac{N_{reco}^{not-matched}(\eta, p_T)}{N_{reco}^{all}(\eta, p_T)} \tag{4.2}$$

where $N_{reco}^{not-matched}(\eta, p_T)$ is the number of reconstructed tracks in a given η, p_T interval without a matched particle, and $N_{reco}^{all}(\eta, p_T)$ is the total number of the reconstructed tracks. Again, all tracks have to pass the selection criteria of Section 4.1.1. The fake track fraction distribution is presented in Figure 4.3 (middle). This fraction turns out to be less than 1‰ for tracks with transverse momentum $p_T < 3$ GeV and it practically vanishes for larger p_T.

Fraction of out-of-kinematic-range tracks is defined as:

$$f_{out}(\eta, p_T) = \frac{N_{reco}^{out-of-range}(\eta, p_T)}{N_{reco}^{all}(\eta, p_T)} \tag{4.3}$$

where $N_{reco}^{out-of-range}(\eta, p_T)$ is the number of tracks reconstructed within the η and p_T acceptances, but originating from regions outside the fiducial volume, and $N_{reco}^{all}(\eta, p_T)$ is the total number of reconstructed tracks in the selected η and p_T range. All tracks have to pass the selection criteria described in Sect. 4.1.1. The distribution of out-of-kinematic-range track fraction is presented in Figure 4.3 (right).

For tracks which are close to kinematic cuts ($p_T \approx 500$ MeV or $|\eta| \approx 2.5$), this fraction reaches ∼10-15%. Further away from the kinematic cuts this factor quickly drops to less than 1%.

Fraction of charged strange baryons

$$f_{sb}(\eta, p_T) = \frac{N_{reco}^{sb}(\eta, p_T)}{N_{reco}^{all}(\eta, p_T)} \tag{4.4}$$

is defined as the ratio of the number of reconstructed tracks with matched charged strange baryon, $N_{reco}^{sb}(\eta, p_T)$, to the total number of reconstructed tracks, $N_{reco}^{all}(\eta, p_T)$, as a function of the track transverse momentum p_T. All tracks need to pass the selection criteria mentioned in Section 4.1.1. The charged strange baryon fraction distribution is presented in Figure 4.4. For very low p_T values, the fraction is close to zero and it increases up to 2.5% for p_T reaching 20 GeV.

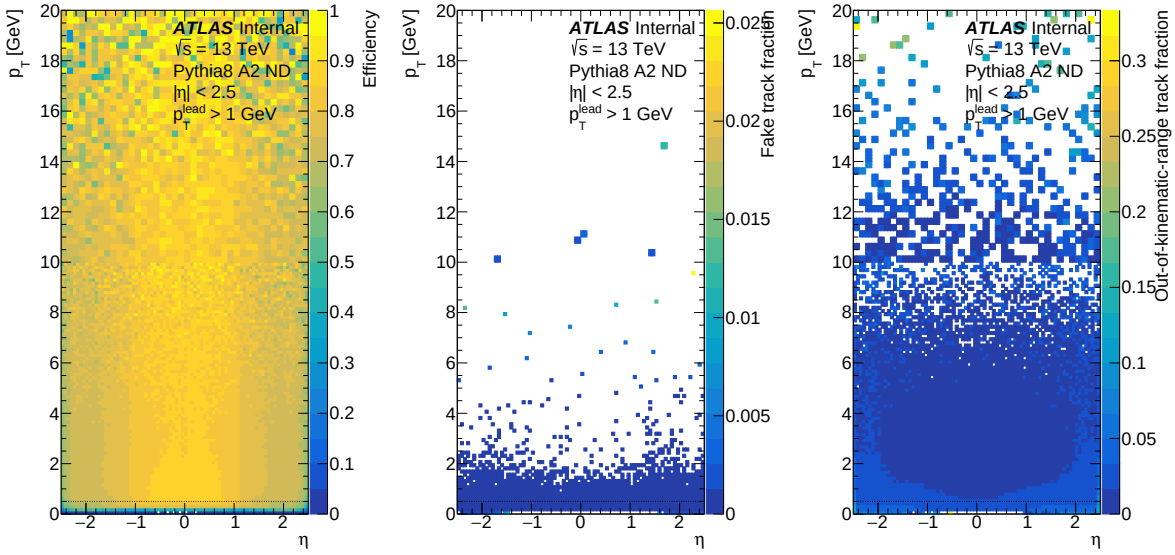

Figure 4.3: The track reconstruction efficiency (left), the fake track fraction (middle) and the out-of-kinematic-range track fraction (right) as a function of pseudorapidity η and transverse momentum p_T. The black dotted line marks kinematic cut on $p_T > 500$ MeV. All distributions start below the cut on p_T, as introducing it here would falsely cause a drop of the low-p_T track efficiency. Note varying binning in different kinematic ranges due to lower statistics for higher p_T values.

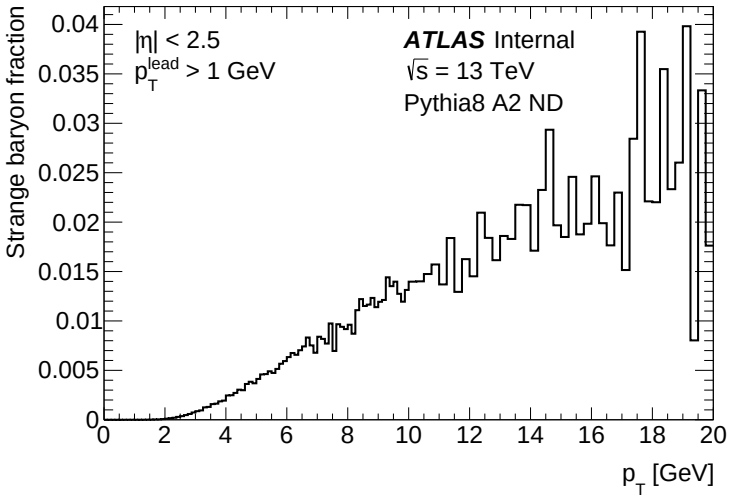

Figure 4.4: The fraction of the charged strange baryons as a function of the particle p_T.

4.2.2 Vertex reconstruction

The vertex reconstruction efficiency is calculated as the ratio of the number of events with at least one reconstructed track and exactly one reconstructed vertex to the number of events with at least one track and zero or one vertex.

$$\epsilon_{vtx}(n_{sel}) = \frac{N_{evt}^{n_{sel}>=1 \wedge n_{vtx}=1}}{N_{evt}^{n_{sel}>=1 \wedge n_{vtx}\in\{0,1\}}} \tag{4.5}$$

It is plotted as a function of the track multiplicity in Figure 4.5. Calculations were done using the MBTS-triggered data sample and with slightly relaxed selection criteria. It was estimated neglecting the cut on the longitudinal impact parameter. It is initially around 90% for a single reconstructed track and quickly rises to 100% if there are two and more reconstructed tracks in an event.

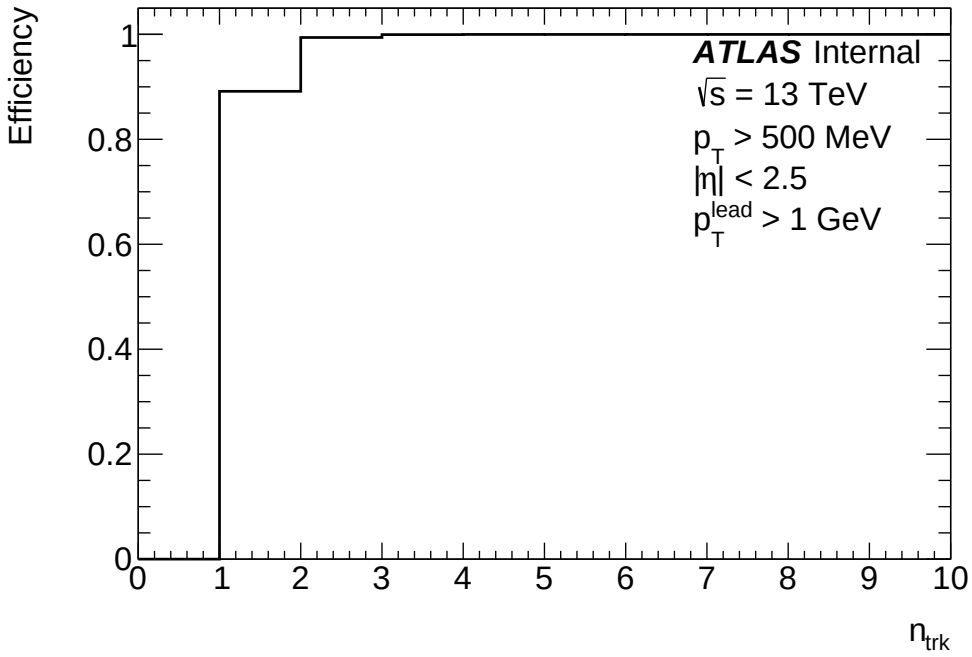

Figure 4.5: The vertex reconstruction efficiency as a function of the multiplicity of the reconstructed tracks.

4.2.3 AFP trigger

The efficiency of the AFP triggers: `L1_AFP_A` and `L1_AFP_C`, was determined by comparing the number of events triggered by various central detector triggers with and without coincidence with the AFP triggers, while requiring a reconstructed proton to be present on a given detector side. Figure 4.6 shows the number of events triggered only by central triggers while Figure 4.7 shows the coincidence of the central and AFP triggers for both ATLAS sides as a function of relative energy loss, ξ, of the reconstructed proton.

If only the central detector triggers are demanded then similar numbers of events registered on both AFP sides are observed. As expected, the additional requirement of the AFP trigger decreases these numbers. However, there is a large asymmetry – a much lower number of

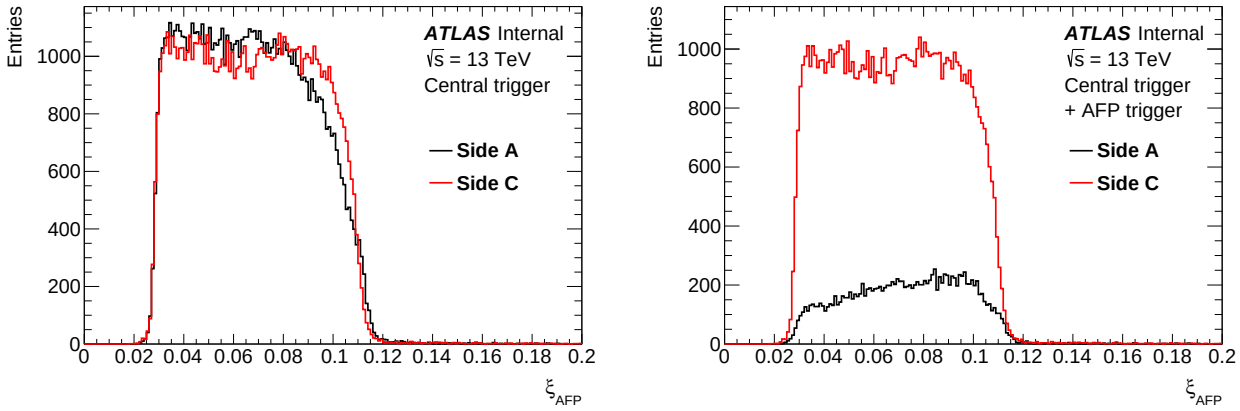

Figure 4.6: The number of events with reconstructed forward proton as a function of its relative energy loss ξ for side A (left) and C (right) triggered by probing triggers (see text).

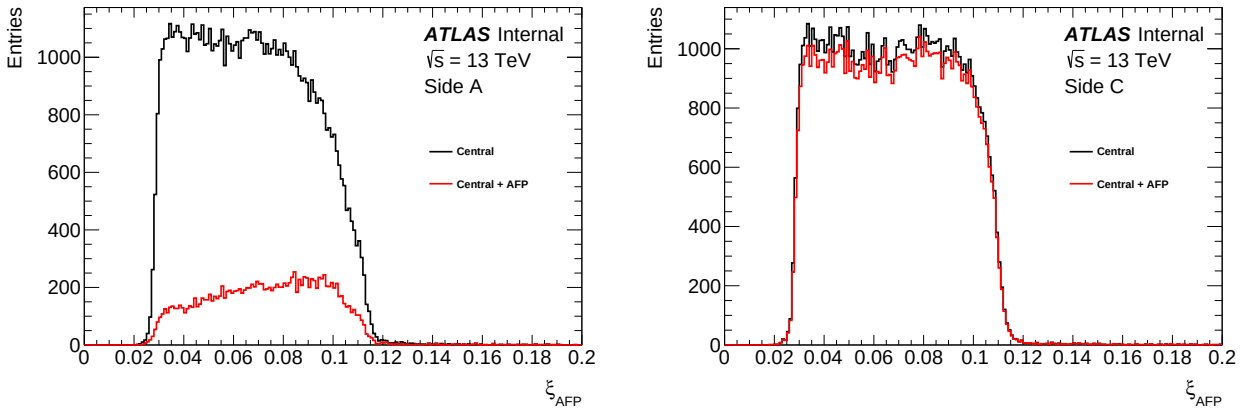

Figure 4.7: The number of events with reconstructed forward proton as a function of its relative energy loss ξ for side A (left) and C (right) triggered by probing triggers and the AFP L1 trigger (A or C). Note much lower number of events on side A compared to Fig. 4.6

events passes the side A selection than the side C one. This can be quantified by calculating the efficiency of the AFP triggers, see Figure 4.8.

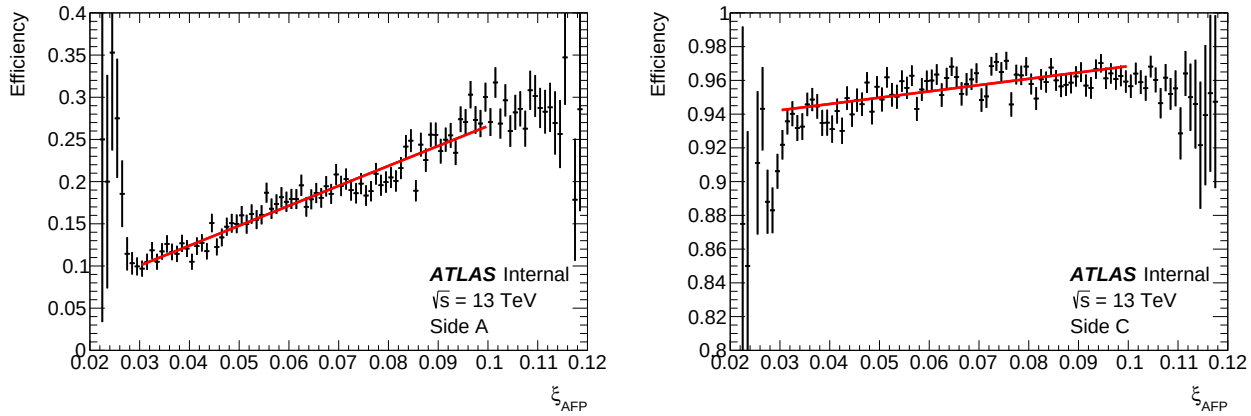

Figure 4.8: The AFP trigger efficiency as a function of the proton relative energy loss ξ for side A (left) and C (right).

The C side efficiency is close to 90% and weakly ξ dependent. For the side A, the efficiency is much lower and varies from 10% to about 30% with ξ increasing from 0.03 to 0.11. This can be a consequence of technical problems with two SiT planes in the A Far station which happen to be selected as ones providing the L1 trigger signal.

The efficiencies on both sides were fitted with a linear function in the considered ξ range:

$$\epsilon^{s}_{AFP}(\xi) = a_s \xi + b_s, \tag{4.6}$$

where s denotes either A or C side. The resulting values of the a and b parameters for both sides are listed in Table 4.2.

Table 4.2: Parameters of the fit to the AFP trigger efficiency.

Side	Parameter a	Parameter b
A	2.363(71)	0.0296(44)
C	0.373(40)	0.9311(28)

4.2.4 Corrections

Per-event efficiency: The effect of the event loss due to inefficiencies of the AFP trigger and the vertex reconstruction were corrected by applying the weight defined as:

$$w_{ev}(n_{sel}, \xi) = \frac{1}{\epsilon_{vtx}(n_{sel})} \cdot \frac{1}{\epsilon_{AFP}(\xi)}, \tag{4.7}$$

where ϵ_{vtx} and ϵ_{AFP} are the vertex reconstruction and the AFP trigger efficiencies, respectively, n_{sel} is the multiplicity of the selected tracks without the vertex requirement and ξ is the relative energy loss of the measured proton.

Per-track efficiency: To correct for inefficiencies related to the track reconstruction the distributions of the selected tracks were weighted by

$$w_{trk}(\eta, p_T) = \frac{1}{\epsilon_{trk}(\eta, p_T)} \cdot (1 - f_{fake}(\eta, p_T) - f_{out}(\eta, p_T) - f_{sb}(p_T)), \tag{4.8}$$

where ϵ_{trk} is the track reconstruction efficiency and f_{fake}, f_{out} and f_{sb} are fractions of the fake, out-of-kinematic-range tracks and the strange baryon, respectively.

The track weight was used in the construction of the $\Sigma\ p_T$ and $\Delta\varphi$ distributions, and also of the mean p_T in an event, determined by calculating the weighted average:

$$\langle p_T \rangle = \frac{\Sigma_{i \in tracks}\ p_T^i w_{trk}^i}{\Sigma_{i \in tracks}\ w_{trk}^i}. \tag{4.9}$$

4.3 Background

Samples of events, which passed the selection criteria, contain in addition to the signal, also an admixture of background events. A typical procedure to correct for the background effects is to subtract statistically the background distribution from the signal one.

4.3.1 Non-diffractive background

In this analysis the two main experimental sources of information are used:

- the central detector – providing the reconstructed vertex and tracks,
- the forward detectors – providing the reconstructed forward protons.

When these two signatures originate from a single proton-proton interaction, such an event is considered a signal event. However, if these two signatures are due to two different interactions – one providing only the tracks and vertex in the central detector and the other providing only a proton in the forward detectors, such an event is considered a background one. Figure 4.9 shows graphical representations of the signal and background events.

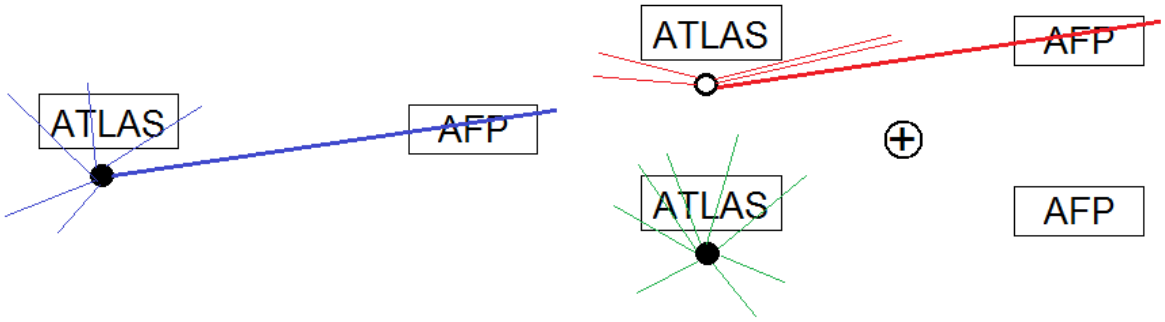

Figure 4.9: Representation of the signal (left) and background (right) events. The signal event – observation of a signal in both the central (tracks and vertex) and forward (proton) detectors originating from a single interaction. The background event – a coincidence of two different interactions, one providing the tracks and vertex in the central detector and the other delivering a proton in the forward detectors.

Using two experimental signatures one can derive three types of measurable classes of processes:

- non-diffractive-like – containing only a vertex without a forward proton,

- single-diffractive-like – a vertex and a forward proton,
- halo-like – only a forward proton.

Calculations of the probabilities of such processes and the number of interactions per bunch crossing allow an estimation of the background contribution. There are four parameters describing the combinatorial background model:

- average number of interactions per bunch crossing (pile-up) – μ,
- probability of non-diffractive-like interaction – p_{nd},
- probability of single-diffractive-like interaction – p_{sd},
- probability of halo-like interaction – p_{halo},

with

$$p_{nd} + p_{sd} + p_{halo} = 1. \tag{4.10}$$

Since events may consist of several processes, it is possible to express the probability of the observation of an event of a certain type by using the above probabilities. Assuming that the probability of a given number of interactions per bunch crossing can be expressed using Poisson distribution:

$$P_{\mu}(n) = e^{-\mu} \cdot \frac{\mu^n}{n!}. \tag{4.11}$$

Probabilities of events with a single reconstructed forward proton and either zero, one, or two reconstructed vertices can be expressed as:

$$P_{AFP+0vtx} = e^{-\mu} \cdot \mu \cdot p_{halo} \tag{4.12}$$

$$P_{AFP+1vtx} = e^{-\mu} \cdot \mu \cdot p_{sd} + e^{-\mu} \cdot \mu^2 \cdot p_{halo} \cdot p_{nd} \tag{4.13}$$

$$P_{AFP+2vtx} = e^{-\mu} \cdot \mu^2 \cdot p_{sd} \cdot p_{nd} + e^{-\mu} \cdot \mu^3 \cdot p_{halo} \cdot p_{nd}^2, \tag{4.14}$$

with an additional constraint on the pile-up:

$$\mu_{MB} = \mu(p_{sd} + p_{nd}), \tag{4.15}$$

where μ_{MB} denotes the pile-up value delivered by the central detector. The probabilities of events are calculated using numbers of the collected events scaled by the AFP trigger prescale to the total number of bunch crossing occured in a given time. The uncertainties were calculated as the square root of the number of events and appropriately scaled. Eventually, the model parameters are obtained by solving equations 4.12, 4.13, 4.14 and 4.15 with 4.10 acting as a constraint on p_{nd}, by minimising the χ^2 function:

$$
\begin{aligned}
&\chi^2(p_{halo}, p_{sd}, p_{nd}, \mu) = \\
&= \left(\frac{e^{-\mu}\cdot\mu\cdot p_{halo} - P_{AFP+0vtx}}{u_{AFP+0vtx}}\right)^2 + \left(\frac{e^{-\mu}\cdot\mu\cdot p_{sd} + e^{-\mu}\cdot\mu^2\cdot p_{halo}\cdot p_{nd} - P_{AFP+1vtx}}{u_{AFP+1vtx}}\right)^2 \\
&+ \left(\frac{e^{-\mu}\cdot\mu^2\cdot p_{sd}\cdot p_{nd} + e^{-\mu}\cdot\mu^3\cdot p_{halo}\cdot p_{nd}^2 - P_{AFP+2vtx}}{u_{AFP+2vtx}}\right)^2 + \left(\frac{\mu(p_{sd}+p_{nd}) - \mu_{MB}}{u_{\mu_{MB}}}\right)^2,
\end{aligned}
\tag{4.16}
$$

where u-symbols denote the statistical uncertainties on given probabilities. The minimisation was performed with Minuit2 [66] and was done for each bunch crossing (BCID) independently. Then, the mean value of each parameter was obtained by fitting a constant. The results of the minimisation with fitted constants are shown in Figure 4.10 and fit results are presented in Table 4.3.

Table 4.3: Parameters of the combinatorial background model.

μ_{mb} source	μ	p_{sd}	p_{nd}	p_{halo}
xAOD	0.04236	0.007265(6)	0.9888	0.003935(4)
Poisson fit	0.03805(14)	0.008309(31)	0.9873	0.004392(16)

The estimation of the combinatorial background is based on Equation 4.13. It consists of two terms: the first corresponds to the signal and the second one to the background. The probability of measuring only the background event is given by:

$$P_{bkg} = e^{-\mu}\cdot\mu^2\cdot p_{halo}\cdot p_{nd}. \tag{4.17}$$

Since the probability of having an event containing only the non-diffractive-like interaction is given by

$$P_{no-AFP} = e^{-\mu}\cdot\mu\cdot p_{nd}, \tag{4.18}$$

then

$$P_{bkg} = (e^{-\mu}\cdot\mu\cdot p_{nd})\cdot\mu\cdot p_{halo} = P_{no-AFP}\cdot\mu\cdot p_{halo}. \tag{4.19}$$

Then the probabilities are transformed into numbers of events. The background distributions are obtained by scaling the distribution of events registered by the MBTS trigger by MBTS trigger prescale P_{MBTS}, μ and p_{halo}:

$$N_{bkg}(n_{trk}) = N_{MBTS}(n_{trk})\cdot P_{MBTS}\cdot\mu\cdot p_{halo}. \tag{4.20}$$

Figure 4.11 shows the comparison of the signal and background distributions of the track multiplicity.

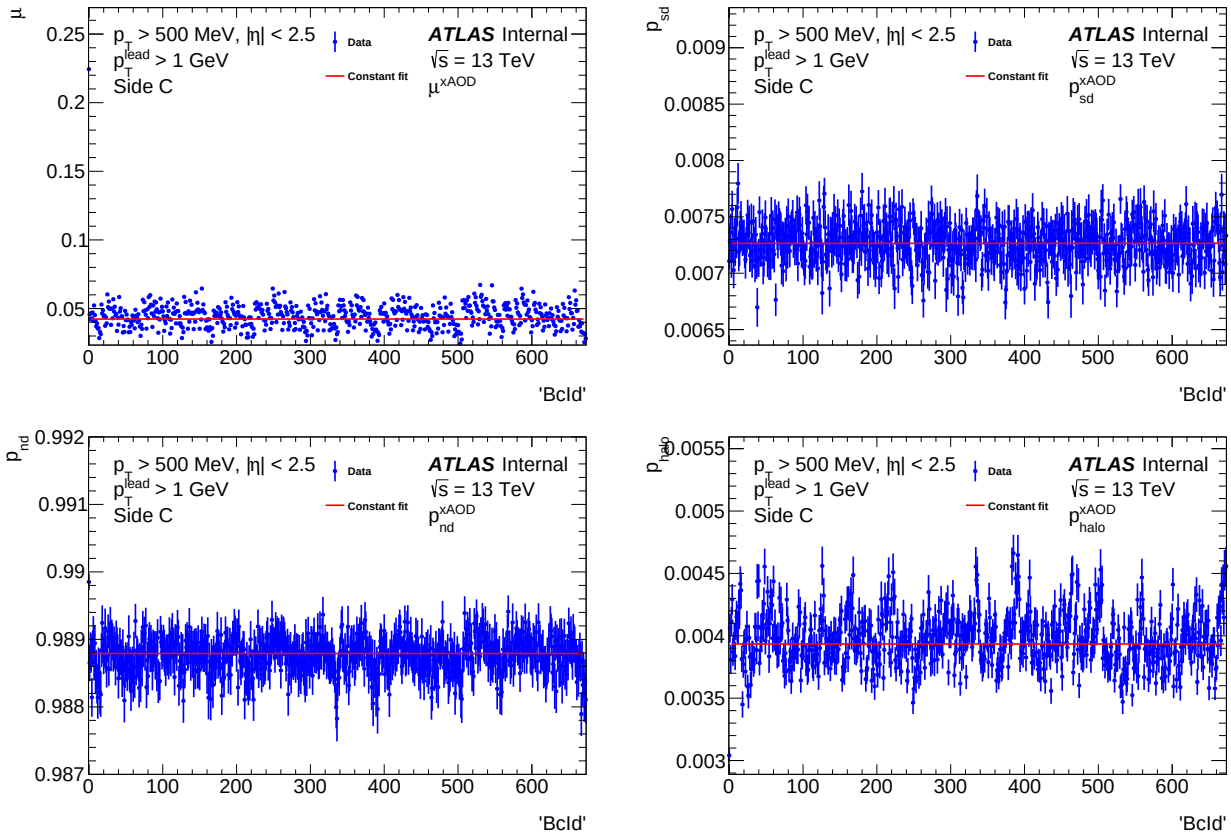

Figure 4.10: Parameters of the combinatorial background parameters: μ (top left), p_{sd} (top right), p_{nd} (bottom left) and p_{halo} (bottom right) as a function of paired bunch crossing number. The values are results of the χ^2 minimisation using the μ_{MB}-value obtained directly from the xAOD file and the experimental data for the side C.

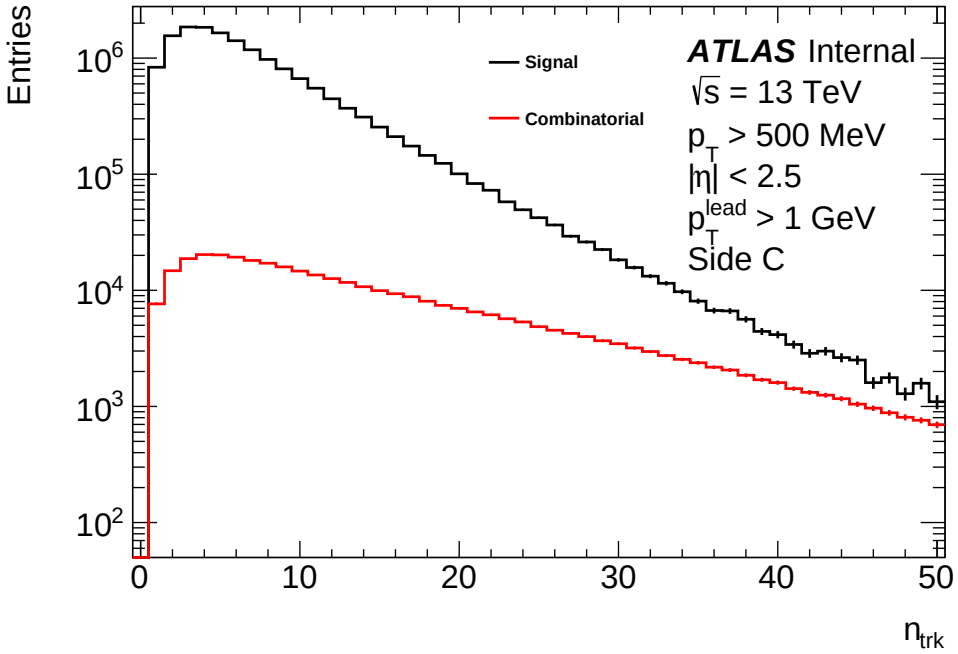

Figure 4.11: Comparison of the signal and background distributions of the track multiplicity.

4.3.2 Combinatorial model uncertainties

There are two sources of uncertainty in the discussed model. The first one is related to the pile-up μ_{MB}-value. It can be obtained either directly from the xAOD file[2] or from a Poisson fit to the vertex multiplicity distribution. An example of such a fit is shown in Figure 4.12. Next, the background model parameters are calculated as described in Section 4.3.1.

The second one is due to the uncertainty on the p_{halo}-value and equation 4.20 becomes:

$$N_{bkg}^{halo}(n_{trk}) = N_{MBTS}(n_{trk}) \cdot \mu^{xAOD} \cdot (p_{halo} + u_{p_{halo}}) \cdot P_{MBTS}, \tag{4.21}$$

where $u_{p_{halo}}$ is the uncertainty on the p_{halo} and follows from p_{halo} spread (cf. Figure 4.10) and is around 5%.

The total uncertainty of the model is calculated as:

$$N_{uncert}^{total}(n_{trk}) = \sqrt{(N_{bkg} - N_{bkg}^{\mu})^2 + (N_{bkg} - N_{bkg}^{halo})^2}. \tag{4.22}$$

4.3.3 Corrections for the MBTS inefficiency

The MBTS trigger inefficiency, especially visible for the low track multiplicity events, implies that the corrections to the background distributions have to be taken into account. The correction is applied to each measured distribution. It is calculated as the ratio of the distributions constructed using samples of events triggered by a probe trigger to those triggered by a coincidence of a probe and the MBTS triggers. The inefficiency of the MBTS trigger, in such a ratio, should be visible as an excess of events triggered only by a probe trigger w.r.t. those selected

[2]Delivered by the ATLAS Luminosity Group.

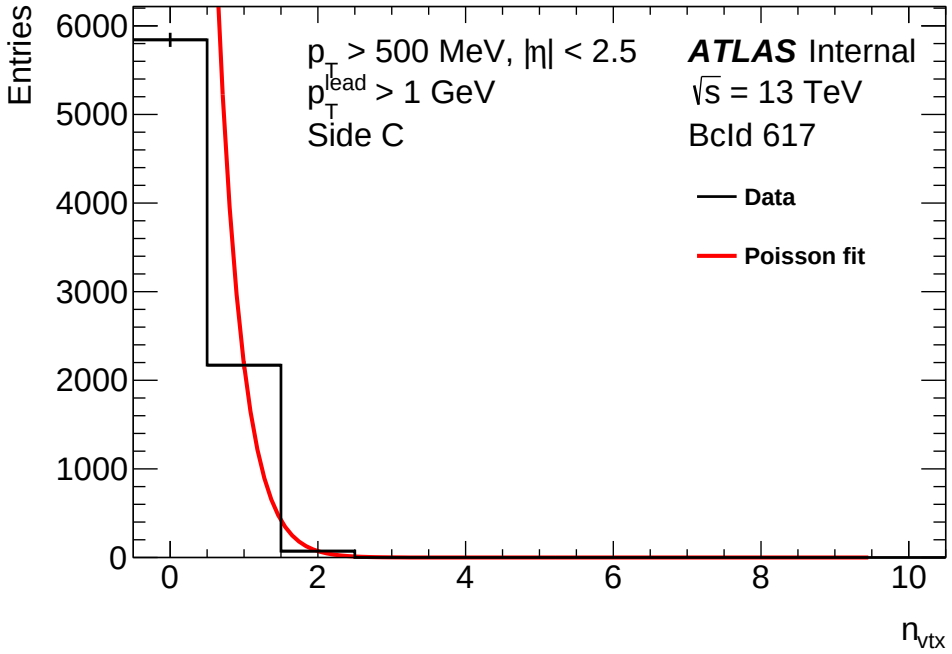

Figure 4.12: Poisson fit to the vertex multiplicity distribution for a single bunch crossing.

requiring both the probe and the MBTS triggers. In this analysis, two probe triggers were considered: the space-track trigger (`HLT_mb_sptrk`), which is the central detector trigger, and the signal triggers (a coincidence of `HLT_noalg_L1AFP_A_OR_C` with `L1_AFP_A` or `L1_AFP_A`. Figure 4.13 (left) compares the distributions obtained using the events triggered with a probe and a probe $\oplus$ MBTS trigger.

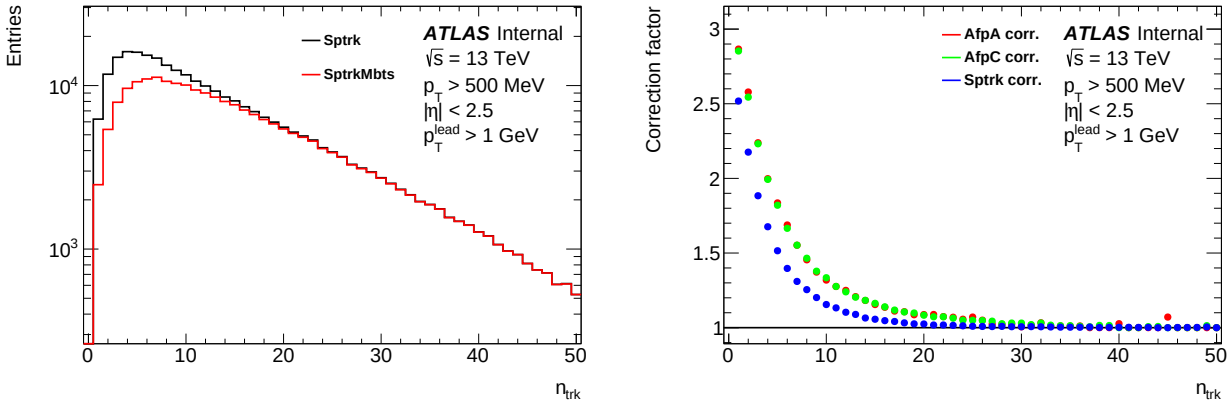

Figure 4.13: Left – comparison of the charged track multiplicity distributions obtained from events triggered by a `HLT_mb_sptrk` (black line) and a coincidence of `HLT_mb_sptrk` and `L1_MBTS_2` (red line). Right – the correction factors for the background for the charged track multiplicity distribution.

The calculated correction factors are shown in Figure 4.13 (right). The background final distributions are calculated by applying these as the multiplicative correction factors. The correction factors obtained using the space-track triggers are taken as the default ones. All others are used in the estimation of the systematic uncertainty of the background model.

4.3.4 Merged vertex background

Another source of background is the vertex reconstruction algorithm. Namely, it is possible that two very close vertices are merged and reconstructed as a single one. Such events pass all other signal selection criteria. Figure **??** shows the distribution of the absolute value of the distance, d, between the vertices in an event with exactly two reconstructed vertices.

A local minimum, close to zero, in the number of events can be observed indicating the merging of the vertices. This shows a migration of two-vertex events into the one-vertex event sample. Such "merged"-vertex events satisfy all the signal selection requirements and it is impossible to distinguish them on the event-by-event basis. Nevertheless, one can approximate the number of migrated events. This can be done by performing a Gaussian fit to the distribution of s (Fig. 4.14). One can integrate the fitted function extrapolated to $d = 0$ obtaining the approximate number of signal-like events with exactly two vertices and subtract from it the actual signal-like events.

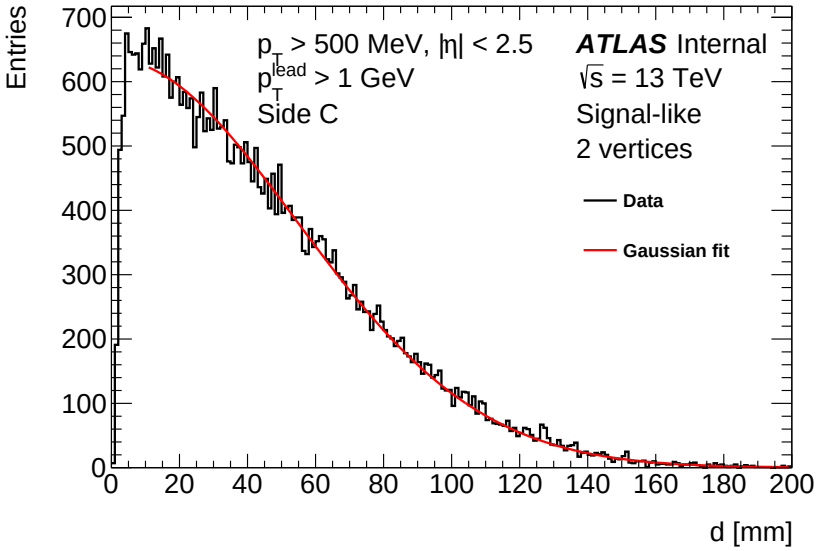

Figure 4.14: The distribution of the distance, d, between a pair of vertices in signal-like events with exactly two vertices. The blue line marks Gaussian fit.

To obtain the merged vertex background distribution one can multiply the signal distribution by a factor equal to the ratio of the approximate number of the migrated events to the measured number of the signal-like events with two vertices reconstructed and then scale it with the AFP triggers' prescale. This is given by:

$$N_{bkg}^{merged}(n_{trk}) = N_{AFP}(n_{trk}) \cdot \frac{N_{migrated}}{N_{actual}} \cdot P_{AFP}. \tag{4.23}$$

In Figure 4.15 the signal and both backgrounds (combinatorial and merged vertex) distributions are compared. One can observe that the amount of the merged vertex background is much smaller than the non-diffractive one.

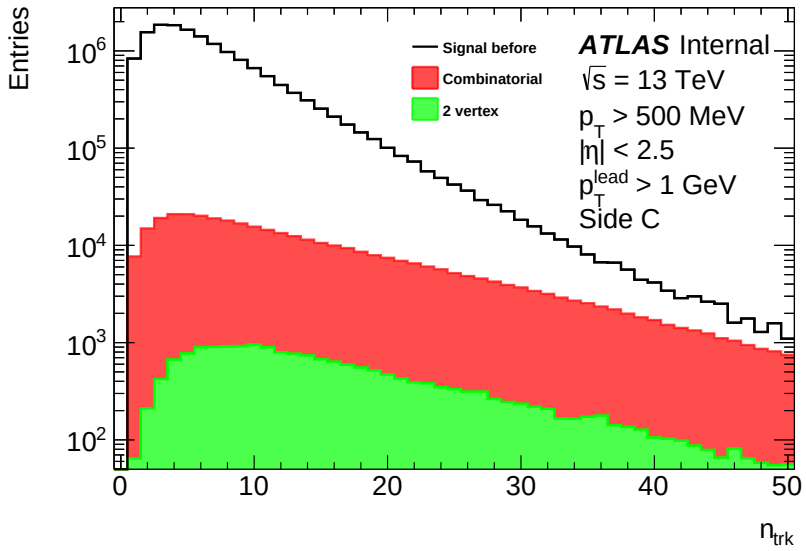

Figure 4.15: Comparison of the signal (black), combinatorial (red) and merged vertex background (green) distributions of the charged track multiplicity.

Chapter 5

Results

This chapter presents the measured distributions of the Underlying Event-sensitive variables. These are: the average number of the charged particle tracks, $\langle n_{trk}/\delta\eta\delta\varphi\rangle$, or the mean value of $\langle \Sigma p_T/\delta\eta\delta\varphi\rangle$ presented as functions of the azimuthal distance from the leading particle, $|\delta\phi|$ or the transverse momentum of the leading particle, p_T^{lead}. They describe the angular distributions of momentum and particle flow w.r.t. the leading track. It has to be stressed that the distributions presented below are for the first time constructed for events containing a forward scattered proton tagged in the AFP. Such events belong to a sample enriched with single diffractive processes. Results of a similar analysis performed without this requirement are described in [63]. Features of the presently measured distributions are discussed below. Predictions of the Monte Carlo single diffractive model of pp interactions are confronted with experimental results.

5.1 Charged particle multiplicity and transverse momentum distributions

At first, general distributions of the charged particle multiplicity and the transverse momentum are shown in Fig. 5.1. These distributions were constructed requiring $p_T^{lead} > 1$ GeV. The presented experimental results were corrected as described in the previous chapter and were unfolded using the Bayesian unfolding method presented in [67]. The charged multiplicity distribution is shown for events with $n_{ch} \leq 50$ since above this value the distribution is dominated by the background [64]. Predictions of Pythia 8 A2 for single diffractive processes (SD) are also shown in the figure.

The experimental charged particle multiplicity distribution raises rapidly and reaches its maximum for $n_{ch} \approx 5$ and then approximately exponentially decreases. The Monte Carlo behaviour is qualitatively similar. However, certain differences are clearly visible. Namely, the maximum is located at $n_{ch} \approx 7$ and the model predicts much more events with $n_{ch} > 12$. Also, the fall of the MC distribution is non-exponential. One may conclude that Pythia 8 A2 SD fails to describe the shape of the charged particle multiplicity distribution.

The charged particle transverse momentum distribution, right panel of Fig. 5.1, is a steeply falling function. Generally, Pythia 8 A2 SD reproduces the experimental distribution quite well. However, it slightly overestimates the high-p_T region, $p_T > 3$ GeV, predicting a bit harder spectrum than that observed in the data. It should be mentioned that this Pythia tune provides

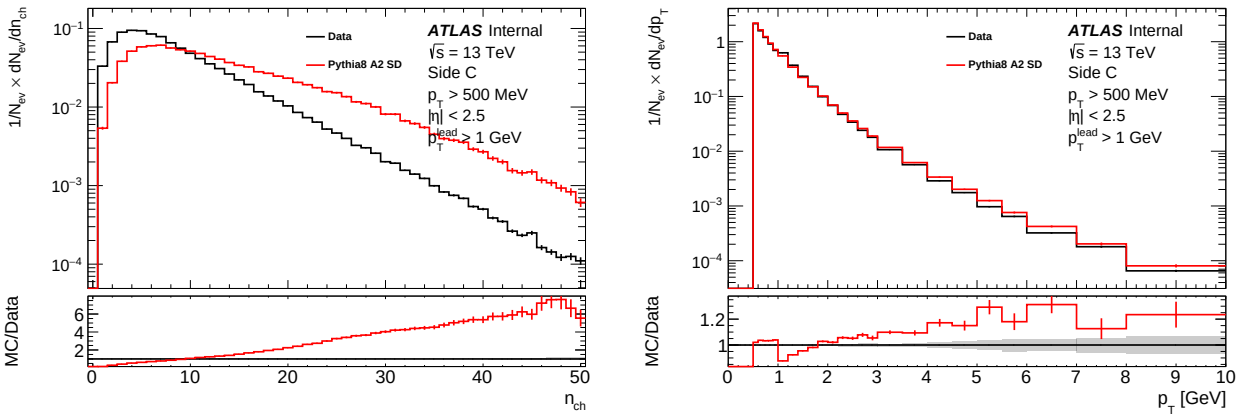

Figure 5.1: The charged particle multiplicity n_{ch} (left) and the charged particle transverse momentum p_T (right) for events with the leading particle of the transverse momentum $p_T^{lead} > 1$ GeV. The ATLAS data - black line, Pythia 8 A2 single diffractive Monte Carlo - red line.

a good description of inclusive data, i.e. without the forward proton requirement.

5.2 Angular distributions of $\langle n_{trk} \rangle$ and $\langle \Sigma p_T \rangle$

The data presented below were selected and corrected as described in chapter 4. The leading particle was used only as a reference and is not included in the distributions presented in the following.

Figure 5.2 shows the mean charged track multiplicity $\langle n_{trk}/\delta\eta\delta\varphi \rangle$, and the mean value of the scalar sum of the charged track transverse momenta, $\langle \Sigma p_T/\delta\eta\delta\varphi \rangle$, as functions of the absolute value of the azimuthal distance from the leading track, $|\Delta\varphi|$, for events with $p_T^{lead} > 1$ GeV. Also, predictions of the Pythia 8 A2 SD Monte Carlo are presented. The three considered angular sectors (c.f. p. 45) are separated by vertical dotted lines.

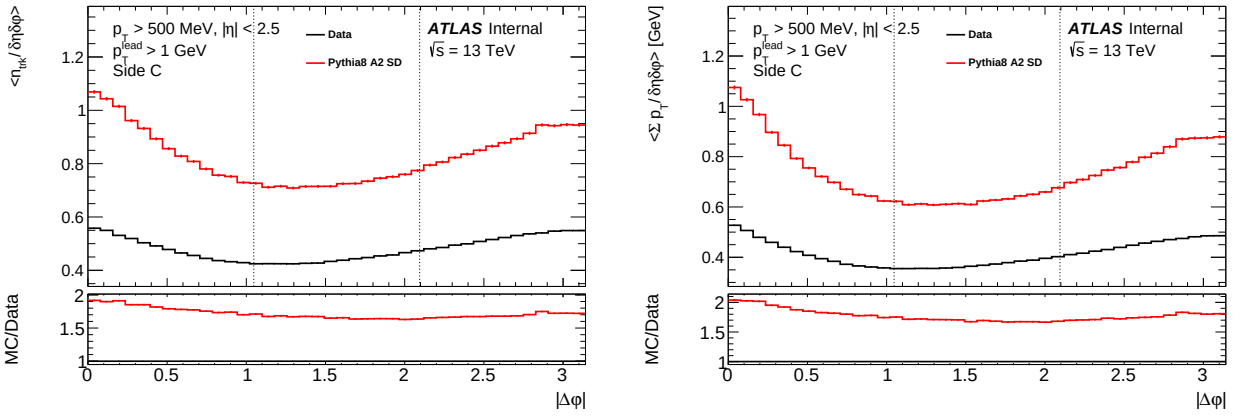

Figure 5.2: The data (black line) and Pythia 8 A2 SD (read line) distributions of mean densities of the charged track multiplicity, $\langle n_{trk}/\delta\eta\delta\varphi \rangle$ (left), and the scalar sum of the transverse momenta, $\langle \Sigma p_T/\delta\eta\delta\varphi \rangle$ (right), as a function of the absolute value of the azimuthal angle difference $|\Delta\varphi|$ for events with the leading particle transverse momentum $p_T^{lead} > 1$ GeV. The vertical dotted lines mark the three considered regions: towards, transverse and away.

The data and Monte Carlo on both plots show the expected behaviour. The highest activity is present in the towards region ($|\Delta\varphi| < \pi/3$) and can be attributed to the (mini) jet associated with the leading particle and in the away region ($|\Delta\varphi| > 2\pi/3$) originating from the recoiling jet. The lowest activity is observed in the transverse region ($\pi/3 < |\Delta\varphi| < 2\pi/3$) and corresponds to the Underlying Event which includes Multi-Parton Interactions.

Despite qualitative similarities, large discrepancies between the data and Monte Carlo are seen. Not only the Monte Carlo predicts much higher values of both $\langle n_{trk} \rangle$ and $\langle \Sigma p_T \rangle$ but also certain differences of the shapes of the distributions are visible. The Monte Carlo predicts a stronger enhancement of the activity in the towards region than experimentally measured.

A deeper insight can be gained by considering the above discussed distributions in different ranges of the leading particle transverse momentum. Results presented in Fig. 5.3 were obtained for three adjacent intervals: $p_T^{lead} \in [1, 2)$, $p_T^{lead} \in [2, 4)$ or $p_T^{lead} \in [4, +\infty)$. These intervals are populated by about 75%, 22.5% and 2.5% of events. The idea behind such a division is related to the development of the jet structure with increasing value of the leading particle transverse momentum.

Qualitatively, the results are similar to those presented in Fig. 5.2. However, with increasing p_T^{lead} value the activity in all azimuthal regions gets larger with a clear domination of the towards region. Moreover, the Monte Carlo predictions approach the experimental distributions from the above.

The p_T^{lead} dependence of the distributions could be attributed to the development and evolution of the jet structure in the event. With increasing transverse momentum the towards (narrow) and recoiling (wide) jets become visible - an increase of the towards and away activities. For even larger p_T^{lead} an additional radiation of a gluon(s) (for example, the third jet) contributing also to the transverse region results in a further increase of the activity.

Concluding, the Pythia 8 A2 SD predictions are only in qualitative agreement with the experimental measurements. They fail to describe accurately both the shapes (20%) and the magnitudes of the distributions. On the other hand the evolution of the shape of the distributions with increasing p_T^{lead} seems to be quite well reproduced by the MC predictions and they gradually approach the data.

5.3 The p_T^{lead} dependence of $\langle n_{trk} \rangle$ and $\langle \Sigma p_T \rangle$

The analysis discussed above can be extended by a study of the p_T^{lead} dependence of $\langle n_{trk}/\delta\eta\delta\varphi \rangle$ and $\langle \Sigma p_T/\delta\eta\delta\varphi \rangle$ in the three discussed regions of $|\delta\varphi|$. The resulting distributions are depicted in Figure 5.4 for the leading track transverse momentum between 1 GeV and 20 GeV.

For $p_T^{lead} < 4$ GeV all distributions show a relatively fast increase which considerably slows down for larger transverse momenta. Both distributions in the transverse region exhibit a sort of a plateau at the level of about 0.5 particle and 0.5 GeV, respectively, per $\eta - \phi$ unit area. The initial increase can be related to the transition from the non-perturbative to the perturbative regime of the interaction. The other two distributions show a nearly linear increase for $p_T^{lead} > 4$ GeV. This increase is a bit faster in the case of the away region distributions. However, one should recall that the leading-p_T particle is excluded from the distributions. Behaviour of the $\langle n_{trk}/\delta\eta\delta\varphi \rangle$ and $\langle \Sigma p_T/\delta\eta\delta\varphi \rangle$ distributions is a manifestation of the growing importance of hard processes with increasing value of the hard scale – the emerging two-jet structure with increasing role of the radiation of additional gluon(s) leading to the three (or

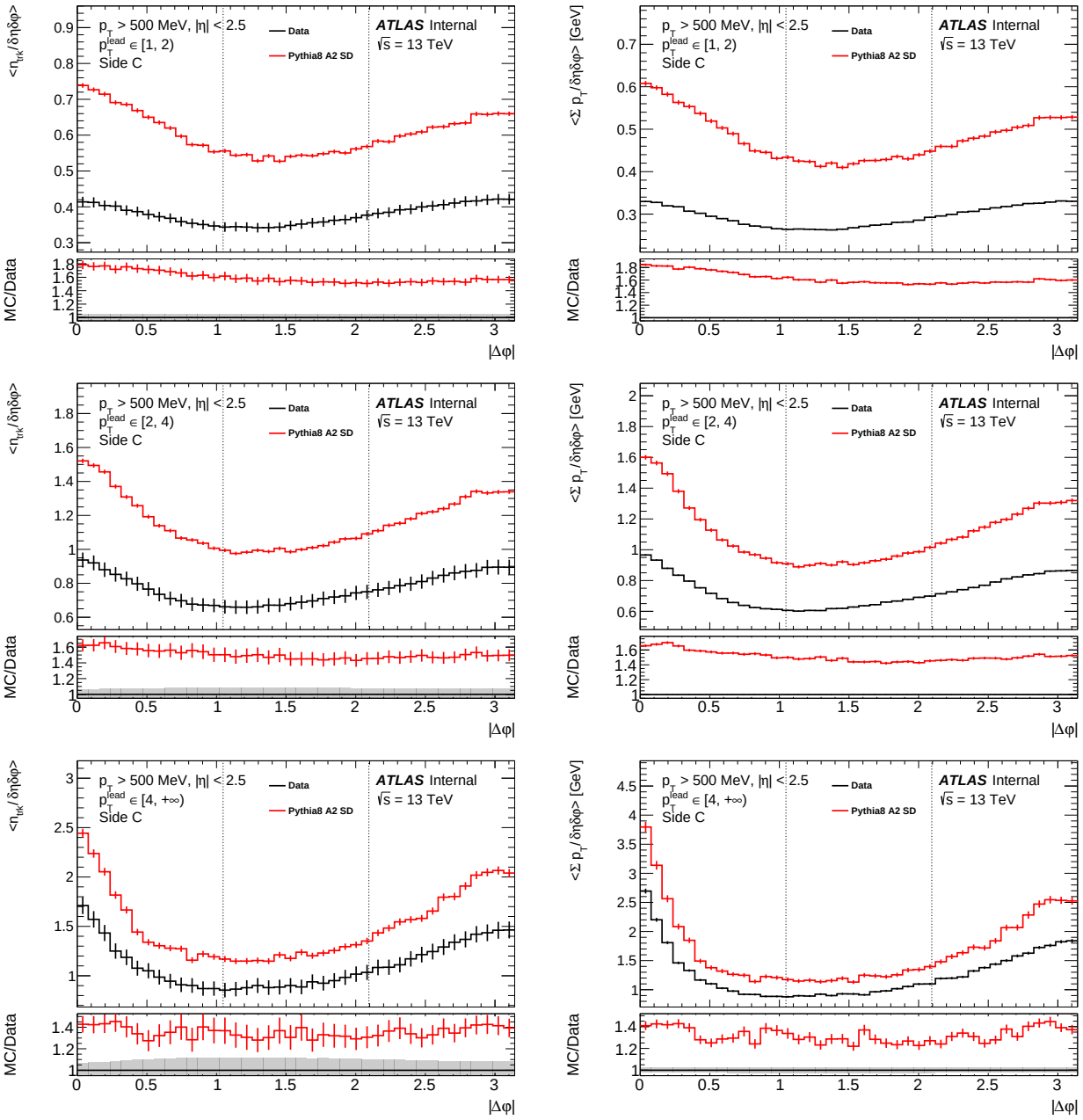

Figure 5.3: The mean charged track multiplicity $\langle n_{trk}/\delta\eta\delta\varphi\rangle$ (left column), and the mean value of the scalar sum of the charged track transverse momenta, $\langle\Sigma p_T/\delta\eta\delta\varphi\rangle$ (right column), as a function of $|\Delta\varphi|$ for three intervals of the leading particle transverse momentum: $p_T^{lead} \in [1, 2)$ (top row), $p_T^{lead} \in [2, 4)$ (middle row) and $p_T^{lead} \in [4, +\infty)$ (bottom row). The ATLAS data - black line, Pythia 8 A2 sigle diffractive Monte Carlo - red line. Vertical dotted lines mark the boundaries between the discussed azimuthal regions: towards, transverse and away.

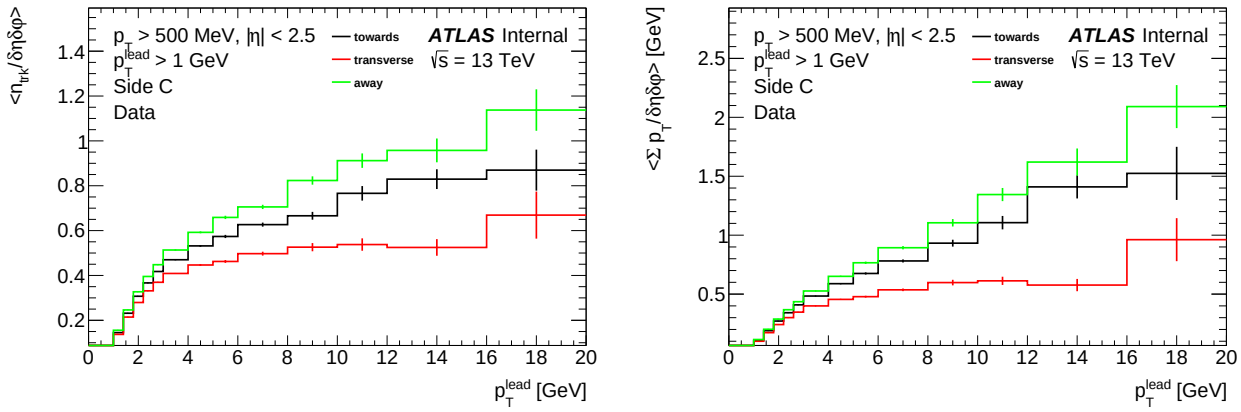

Figure 5.4: Mean $\eta\varphi$ densities of the charged particle track multiplicities n_{trk} (left) and of the sum of the transverse momenta Σp_T (right) as a function of transverse momentum of leading charged track in the towards, transverse and away regions.

more complex) jet configuration of an event. Such a behaviour was already seen in one-photon annihilation events at the e^+e^- machines and delivered experimental evidence for gluons in the three jet, "Mercedes", events, see [68–70]. One should also observe that the reached values of $\langle n_{trk} \rangle$ and $\langle \Sigma p_T \rangle$ per unit $\eta - \phi$ area are about a factor of two smaller than those measured in the inclusive case [63].

The discussed distributions are shown together with the Pythia 8 A2 SD predictions in Figure 5.5. The Monte Carlo follows the behaviour discussed above with a more rapid increase for $p_T^{lead} < 4$ GeV. However, it fails to describe the data overestimating the values of both $\langle n_{trk} \rangle$ and $\langle \Sigma p_T \rangle$ for $p_T^{lead} < 8$ GeV. For larger p_T^{lead} the Monte Carlo predicted values are compatible with the data within large errors.

5.4 n_{trk} and Σp_T densities in transverse min/max/diff regions

The next step of the present analysis is focused on the transverse region which is expected to be most sensitive to the UE effects. This region, on the event-by-event basis, is split into two sides: transMax and transMin. The transMax is sensitive to the MPIs and additional gluon radiation while the transMin sensitivity is nearly solely related to the MPIs. The transDiff measures the difference between of the two.

The measured and Pythia 8 A2 SD simulated distributions of $\langle n_{trk}/\delta\eta\delta\varphi \rangle$ and $\langle \Sigma p_T/\delta\eta\delta\varphi \rangle$ are presented in Figure 5.6 as functions of the leading particle transverse momentum for the three considered regions.

Qualitatively, all distributions follow the same pattern: a rapid initial increase followed by a flattening of the dependence. In the transMax and transMin regions the Monte Carlo predictions overestimate both the initial growth and values up to p_T^{lead} of about 8-10 GeV. For larger p_T^{lead} the MC agrees with the data within the errors. In case of the transDiff distributions Pythia 8 A2 SD reproduces the experimental result relatively well. However, it still overestimates the measurements for $p_T^{lead} < 8$ GeV. The measured values are a factor of about two smaller than in the inclusive case [63].

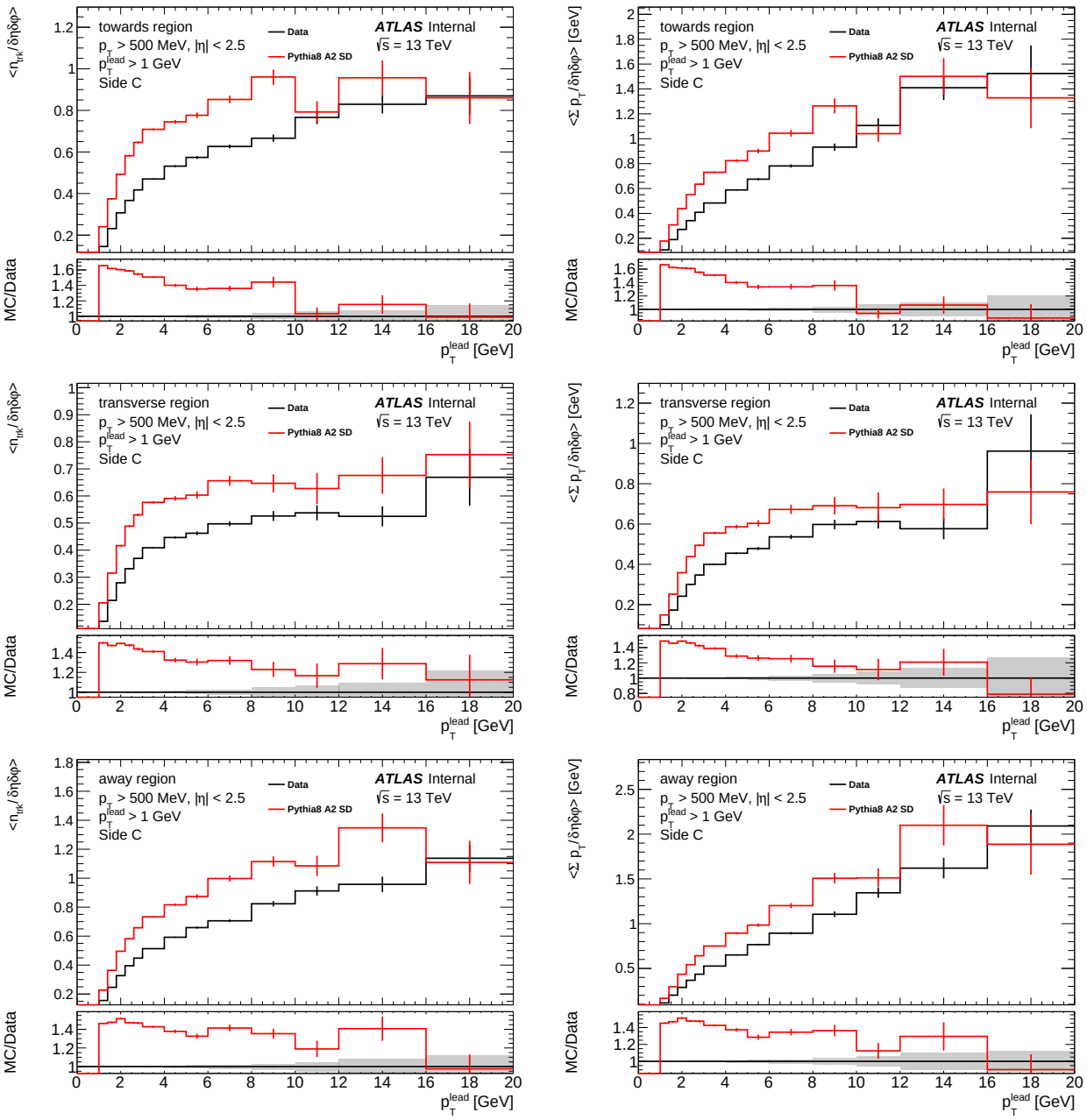

Figure 5.5: Mean $\eta\varphi$ densities of the charged particle track multiplicities n_{trk} (left) and mean $\eta\varphi$ densities of the sum of the charged track transverse momenta Σp_T (right) as a function of the transverse momentum of the leading charged track in the towards (top), transverse (middle) and away (bottom) regions. Predictions of the Pythia 8 A2 single diffractive Monte Carlo is marked with the red line.

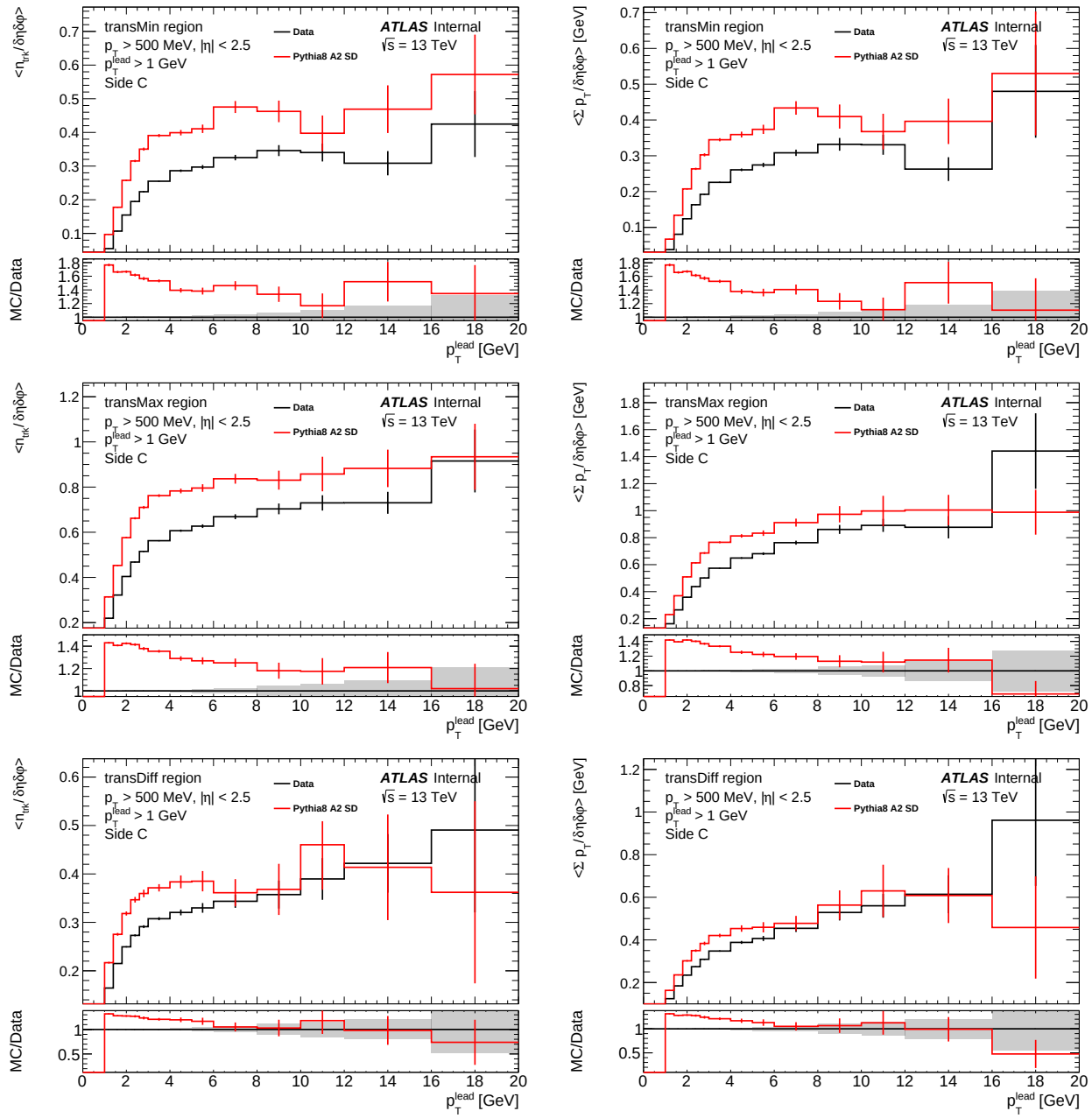

Figure 5.6: Mean $\eta\varphi$ densities of charged track multiplicities n_{trk} (left) and mean $\eta\varphi$ densities of sum of charged track transverse momenta Σp_T (right) as a function of transverse momentum of leading charged track in the transMin (top), transMax (middle) and transDiff (bottom) regions. Predictions of the Pythia 8 A2 single diffractive Monte Carlo is marked with the red line.

5.5 Mean transverse momentum in transverse, transMin and transMax regions

The dependence of the per-event $\langle$mean $p_T\rangle$ value (see eq. 4.9) on the observables related to an event may provide some constrains concerning the colour reconfiguration. The colour-reconnection/-disruption mechanisms reshuffle the colour field leading to the energetically preferred state of the system and typically increase the transverse momentum [63].

The measured relations between the per-event $\langle$mean $p_T\rangle$ as a function of the leading particle transverse momentum are presented in Figure 5.7 (left) for the transverse, transMin, transMax regions together with the single diffractive Pythia 8 A2 predictions.

Again, for low p_T^{lead} values there is a rapid raise of the $\langle$mean $p_T\rangle$ value, and above $p_T^{lead} \approx 4$ GeV the distributions reach a sort of a plateau. Contrary to all previous results, these distributions are relatively well reproduced by the Monte Carlo predictions in all discussed regions.

One may also investigate the dependence of the per-event $\langle$mean $p_T\rangle$ on the charged track multiplicity. Figure 5.7 (right) presents the results of this investigation for the three considered regions. The single diffractive Pythia 8 A2 predictions are represented by the red line.

In all three presented regions, the Monte Carlo nicely reproduces the measured distribution. Value of $\langle$mean $p_T\rangle$ slowly increases from ~ 0.7 GeV to about 1.1 GeV with $n_{trk}^{transverse}$ growing from 1 to 20. For $n_{trk}^{transverse} > 20$, a clear limitation of the available statistics is seen and the MC predictions are compatible with the data within the errors.

The measured values are similar to those reported by the inclusive analysis [63], however, in a narrower multiplicity range. As can be seen from Fig. 5.7 (right) the presently measured multiplicities are limited to 28.

5.6 Summary of measurements

This chapter was focused on the experimental observables sensitive to the Underlying Event phenomena. These results were obtained selecting charged particles within the acceptance of the ATLAS Inner Detector and requesting a forward proton tag in the AFP. The data were corrected for various experimental effects. The selected sample is enriched in the single diffractive dissociation processes.

It was found that the single diffractive Pythia 8 A2 predictions describe the charged particle transverse momentum spectrum, however, they fail to describe the charged multiplicity distribution. The Monte Carlo overestimates the number of high multiplicity events.

Among the distributions sensitive to UE, the distributions of $\langle n_{trk}\rangle$, $\langle \Sigma p_T\rangle$ and $\langle$mean $p_T\rangle$ were investigated in three azimuthal regions (towards, transverse and away) defined with respect to the direction of the leading particle, p_T^{lead}, – the one with the highest value of the transverse momentum. In the case of the analysis performed on the event-by-event basis, the transverse region was divided into two: "Max" – containing higher activity and "Min". The distribution of the observables were studied as functions of p_T^{lead} or the charged particle track multiplicity within a region, n_{trk}.

It was found that the predictions of single diffractive Pythia 8 A2 Monte Carlo are in a qualitative agreement with the data but they fail to reproduced the experimental distributions

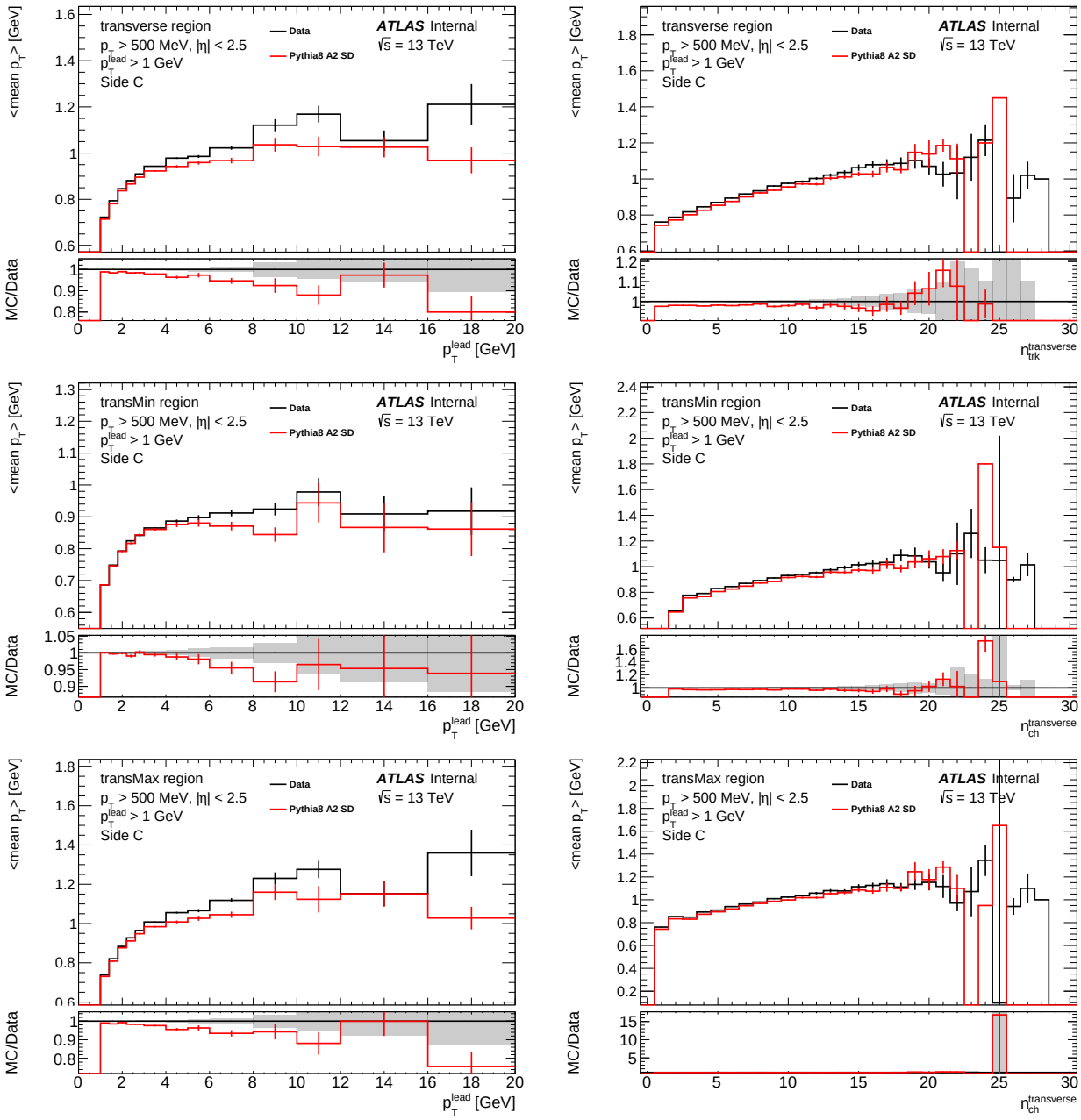

Figure 5.7: The per-event average transverse momentum of charged tracks $\langle \text{mean } p_T \rangle$ as a function of the leading particle transverse momentum (left) and of the charged track multiplicity in transverse region $n_{trk}^{transverse}$ (right) in the transverse (top), transMin (middle) and transMax (bottom) regions. Prediction of the Pythia 8 A2 SD Monte Carlo are marked with red line.

overestimating the values. It should be noted that the description of the $\langle n_{trk} \rangle$ and $\langle \Sigma p_T \rangle$ distributions improves with increasing value of p_T^{lead}. The obtained experimental results are lower by a factor of about two than those measured for inclusive data. The only properly predicted distributions are those of the per-event $\langle$mean $p_T\rangle$ as functions of the p_T^{lead} and n_{trk}.

Behaviour of the $\langle n_{trk} \rangle$ and $\langle \Sigma p_T \rangle$ distributions indicates the growing importance of hard processes with increasing value of the hard scale – the emerging two-jet structure with increasing role of the radiation of additional gluon(s) contributing to more complex structure of an event.

Chapter 6

Monte Carlo tuning

As it was demonstrated in chapter 5, the Monte Carlo predictions do not reproduce majority of the data features. Therefore, the next step is an attempt to tune the Monte Carlo model in such a way that its predictions are as close to the data as possible.

Pythia Monte Carlo generator has many adjustable parameters which impact the delivered predictions. To quantify how well the chosen set of parameters influences the reproduction of the data features, a set of samples with different values of the selected parameters was generated. Each sample contains 1 million single diffractive events. These events were requested to pass the same selection criteria as for an ordinary Monte Carlo sample. The obtained results were then compared to the data and the predictions of the Pythia 8 A2 single diffractive Monte Carlo generated with the default settings. The distributions chosen for the tuning procedure are the mean number of the charged particle tracks as a function of $|\Delta\varphi|$, referred to as "$\Delta\varphi$ plot", in different bins of the leading track transverse momentum.

6.1 Pythia parameters

The considered Pythia 8 flags and parameters are listed in Tables 6.1 and 6.2 and briefly described below:

Table 6.1: Pythia flags.

Group	Name	Tune default
Tune	pp	A2 MSTW2008LO
SigmaDiffractive	PomFlux	1
MultipartonInteractions	bProfile	4
PartonLevel	MPI	on
PartonLevel	ISR	on
PartonLevel	FSR	on

Tune:pp: a set of generation settings known as tune. The Pythia default tune is the 2013 Monash tune [71]. The default in this study is the Pythia 8 A2 tune [60] with the MSTW2008LO PDF set [7]. Yet another tune is the A2 tune using the CTEQ6L1 PDF set.

Table 6.2: Pythia parameters.

Group	Name	Unit	Tune default	Min. value	Max. value
Diffraction	sigmaRefPomP	mb	10	2	40
Diffraction	mPowPomP	-	0	0	0.5
Diffraction	mMinPert	GeV	10	5	-
Diffraction	mRefPomP	GeV	100	1	-
MultipartonInteractions	pT0Ref	GeV	1.9	0.5	10

It is worth mentioning that the choice of the PDFs is not the only difference distinguishing the A2 tunes as they use slightly different values of other parameters.

Figure 6.1 compares the n_{ch} and $< n_{trk} >$ vs. $|\delta\varphi$ distributions obtained using different tunes. As one can observe the MC predicted charged particle multiplicity distributions are practically identical with some differences in the high n_{ch} tail. The difference between the predictions of different tunes shows up in the $\Delta\varphi$ plot. The MC predictions are of nearly the same shape, however, they differ in the average value. The A2 tune with MSTW2008LO PDF predicts the mean multiplicities higher than those delivered by CTEQ6L1 or Monash tunes. All used Monte Carlo models fail to describe the data.

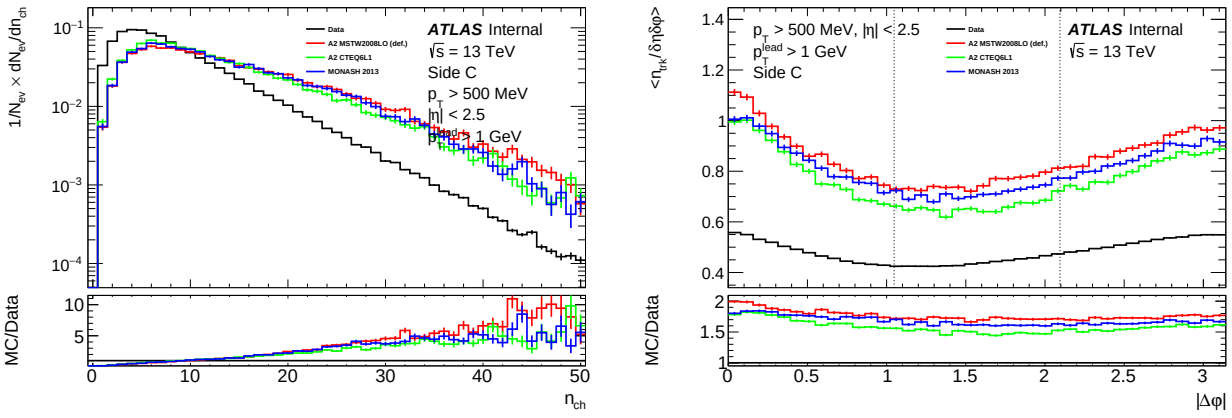

Figure 6.1: Comparison of the charged particle multiplicity (left) and the average number of tracks as a function of $|\Delta\varphi|$ (right) generated using different Pythia 8 tunes to the data.

SigmaDiffractive:PomFlux: governs the choice of the pomeron flux parameterisation. The default setting (*1*) uses a description based on the critical pomeron given by Schuler and Sjöstrand [21] The other settings: *4* uses conventional pomeron description discussed by Donnachie and Landshoff [20], *5* uses the MBR simulation of proton-proton interactions [72] and *6* uses the H1 Fit A parameterisation [73,74]. Figure 6.2 shows the considered distributions generated using these settings compared to the experimental results. This parameter has no effect on both of the.

MultipartonInteractions:bProfile: steers the choice of the impact parameter profile for the incoming hadron beams. The A2 tune settings, marked by *4* in Figures, use Gaussian distribution with a width varying as $1 + a_1 \log(1/x)$, where a_1 is a free parameter and x denotes the Bjorken x of a parton. The Pythia default setting (*1*) uses a simple Gaussian distribution without any free parameters, *2* uses a double Gaussian distribution, with two free parameters and *3* uses an overlap function of the form $e^{-b^{expPow}}$, where *expPow* is an additional free

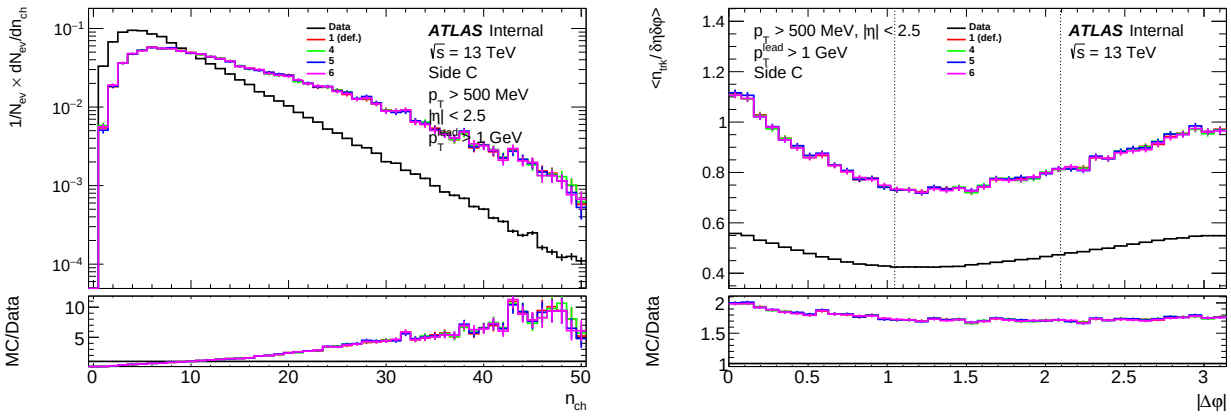

Figure 6.2: Comparison of the charged particle multiplicity (left) and the mean number of tracks as a function of $|\Delta\varphi|$ (right) for various setting of the SigmaDiffractive:PomFlux flag to the data (see text).

parameter. Figure 6.3 shows a comparison of distributions generated using these settings.

The charged particle multiplicity distributions differ slightly in the shapes. The differences become for large n_{ch}. The $\Delta\varphi$ plot shows similarities of both the shapes and normalisations of the predicted dependencies. All MC versions fail to describe the data.

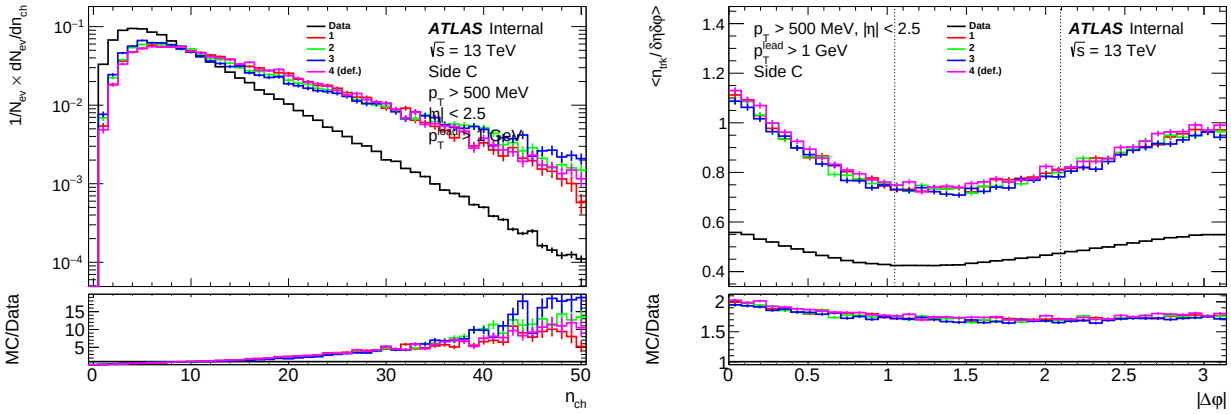

Figure 6.3: Comparison of the charged particle multiplicity (left) and the mean number of tracks as a function of $|\Delta\varphi|$ (right) for the different values of the MultipartonInteractions:bProfile flag to the data (see text).

PartonLevel:MPI, **PartonLevel:ISR**, **PartonLevel:FSR**: provide the largest contributors to the Underlying Event activity. All tunes have these processes turned on. Nevertheless, it is worth to investigate their impact on the predicted distributions. The results are shown in Figure 6.4.

In all cases, switching any component off noticeably impacts the predictions:

- Charged particle multiplicity: the distributions are steeper – with an increased number of low multiplicity events and a less populated high multiplicity region. Turning the ISR flag off gives the multiplicity distribution which is the closest to the measured one. As expected, turning off the MPI flag considerably reduces the number of high multiplicity events.

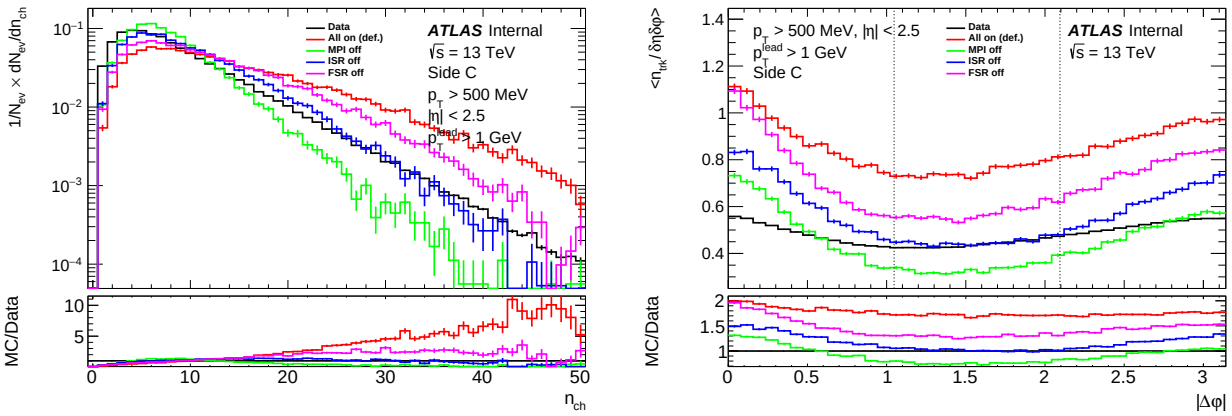

Figure 6.4: Comparison of the charged particle multiplicity (left) and the mean number of tracks as a function of $|\Delta\varphi|$ (right) for all flags turned on (default, red line) and each of the PartonLevel:MPI, PartonLevel:ISR and PartonLevel:FSR flags set off separately to the data.

- Mean number of the charged particle tracks: both the shape and normalisation of the distributions change significantly. This was anticipated since switching off any Underlying Event component lowers the activity in the transverse region.

Diffraction:mMinPert: defines the mass threshold in soft diffraction separating the low- (non-perturbative) and high- (perturbative) mass regimes. The default value for A2 tune is 10 GeV. The parameter value ranges between 5 GeV and infinity. If the used value exceeds the centre-of-mass energy, then no perturbative description will be used. Figure 6.5 shows the MC predictions generated for few values of the Diffraction:mMinPert parameter compared to the data.

This setting dramatically reduces the charged multiplicity and hence the mean number of tracks in all angular regions. Generally speaking, the change of the parameter value up to 1000 GeV has relatively small impact on the distributions. For larger values the distribution of the charged multiplicity and the mean number of tracks change the shape or normalisation and for Diffraction:mMinPert = 3500 GeV the generated distribution of $\langle n_{trk} \rangle$ vs. $|\Delta\varphi|$ is the closest to the experimental one. For the Diffraction:mMinPert values above the CMS energy of pp interaction no events with $n_{ch} > 10$ are predicted.

The next set of parameters belonging to the **Diffraction** group, **sigmaRefPomP**, **mRefPomP** and **mPowPomP**, is related to the high-mass soft diffraction. The standard perturbative MPI framework in Pythia provides the cross-sections for parton-parton interactions. To transform the cross-sections into the probabilities, the ansatz for the proton-promeron cross-section is required. Its dependence on the mass of the diffrective system m is assumed to have the form:

$$\sigma_{PomP}(m) = \sigma_{PomP}^{ref} * (m/m_{ref})^{p}, \tag{6.1}$$

where σ_{PomP}^{ref} (**Diffraction:sigmaRefPomP**) denotes the reference cross-section, m_{ref} (**Diffraction:mRefP**
is the reference mass scale and p (**Diffraction:mPowPomP**) is the mass rescaling pace.

Diffraction:sigmaRefPomP: the parameter default value for the A2 tune is 10 mb, with the range spanned between 2 mb and 40 mb. Figure 6.6 shows the distributions generated assuming Diffraction:sigmaRefPomP of 10 mb, 20 mb and 40 mb compared to the data.

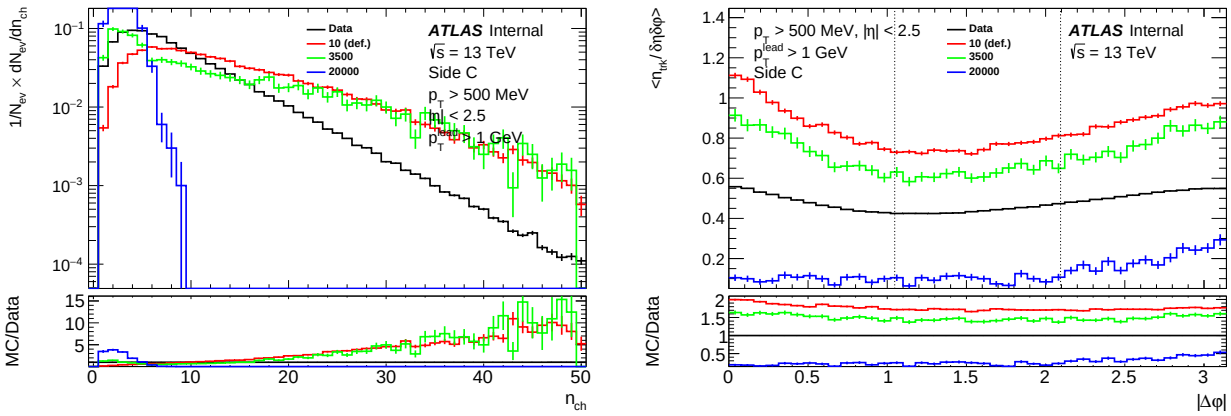

Figure 6.5: Comparison of the charged particle multiplicity (left) and the mean number of tracks as a function of $|\Delta\varphi|$ (right) for different values of the Diffraction:mMinPert parameter to the data.

The distributions generated for Diffraction:sigmaRefPomP = 20 mb are closest to the experimental ones. However, the number of the high multiplicity events is slightly underestimated. The 40 mb sample delivers the multiplicity distribution which is narrower than the experimental one, which underestimates both high and low multiplicities while overestimating the number of events with n_{ch} between 4 and 8. In case of the $\Delta\varphi$ plot, with increasing value of the parameter, the normalisation decreases and the shape of the distribution becomes slightly flatter. The default value of the parameter predicts the highest mean multiplicities. For the 20 mb-sample, the mean number of charged tracks reproduces the measurement in the transverse region, but in towards and away regions the predictions are much higher than the data. Finally, for the 40 mb sample the Monte Carlo prediction matches the measurement for small $|\Delta\varphi|$ values and underestimates the data elsewhere.

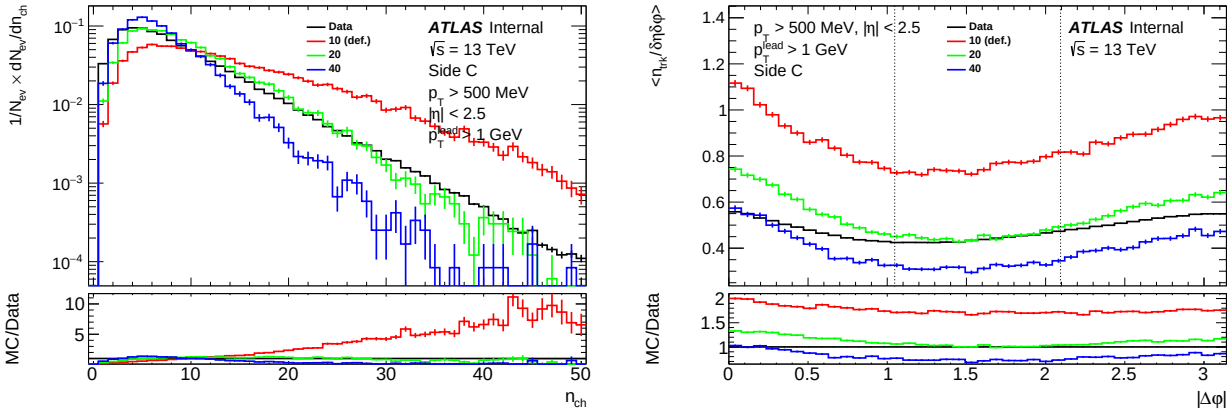

Figure 6.6: Comparison of the charged particle multiplicity (left) and the mean number of tracks as a function of $|\Delta\varphi|$ (right) for different values of the Diffraction:sigmaRefPomP compared to the data.

Diffraction:mRefPomP: the reference mass scale for calculating the effective proton-pomeron cross-section. The default is set to 100 GeV. The parameter ranges between 1 GeV and infinity. The distributions generated for few arbitrary values of this parameter are compared in Figure 6.7 with each other and the data.

As can be observed, the Diffraction:mRefPomP very weakly influences the distributions.

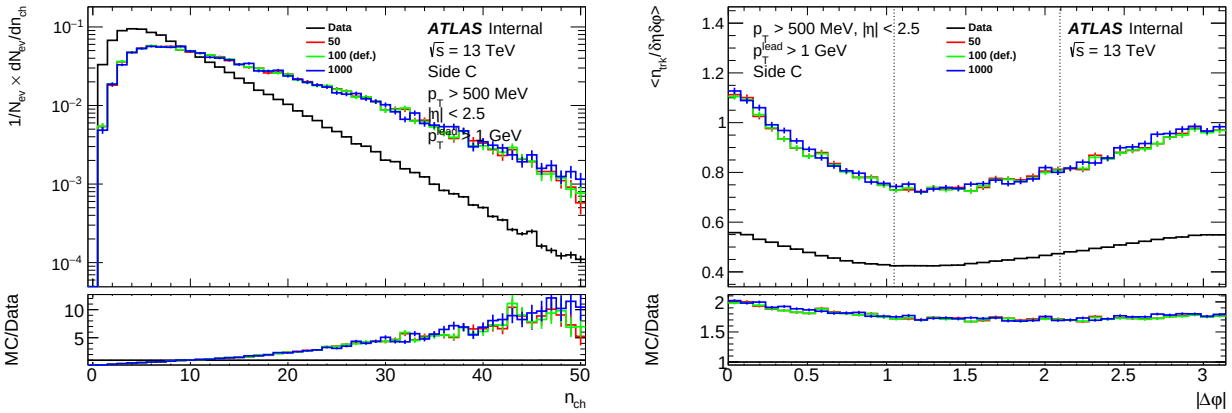

Figure 6.7: Comparison of the charged particle multiplicity (left) and the mean number of tracks as a function of $|\Delta\varphi|$ (right) for different values of the Diffraction:mRefPomP to the data.

Diffraction:mPowPomP: the mass rescaling pace for calculating the effective proton-pomeron cross-section. It is defaulted to zero in A2 tune and potentially ranging between zero and 0.5. In Figure 6.8 the distributions generated with with the parameter value set to 0, 0.2, and 0.5 are compared to the experimental results.

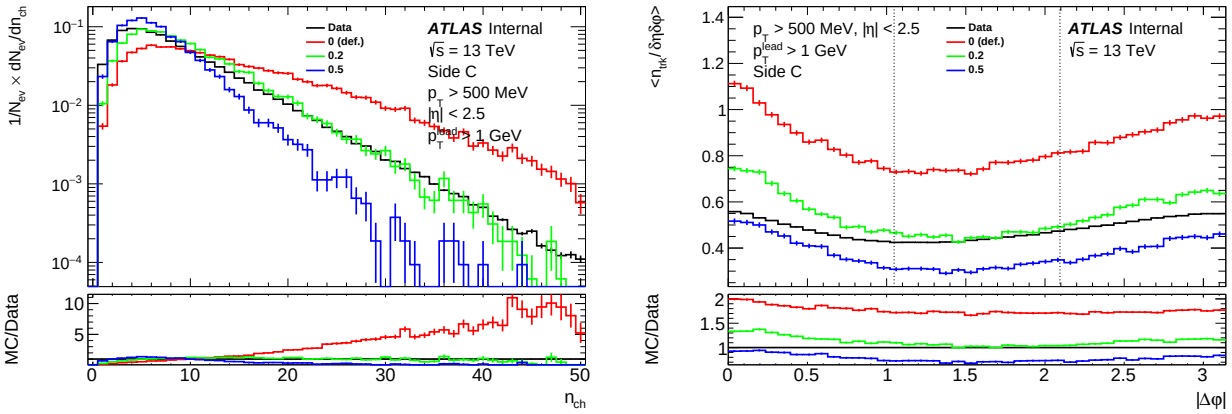

Figure 6.8: Comparison of the charged particle multiplicity (left) and the mean number of tracks as a function of $|\Delta\varphi|$ (right) for different values of the Diffraction:mPowPomP to the data.

The results are similar to those obtained in the **sigmaRefPomP** parameter case. The sample generated with the parameter value set to 0.2 provides the best description of the experimental multiplicity distribution, however the number of low multiplicity events is still underestimated. If Diffraction:mPowPomP = 0.5 then the description of low n_{trk} region improves but high multiplicities are largely underestimated. In case of the $\Delta\varphi$ plot, with increasing value of the parameter, the normalisation decreases and the distribution becomes slightly flatter. The default value of the parameter leads to the highest mean multiplicities. If it is set to 0.2, the mean number of the charged tracks agrees with the data in the transverse region, but in the towards and away regions the Monte Carlo predicts much higher means. Finally, if the parameter is set to 0.5, the Monte Carlo predictions do not reproduce the data underestimating them.

MultipartonInteractions:pT0Ref: the reference scale in the $pT0$ parameterisation formula:

$$pT0 = pT0(ecmNow) = pT0Ref * (ecmNow/ecmRef)^{ecmPow}, \tag{6.2}$$

where $ecmNow$ is the CMS energy, $pT0Ref$ is the pT0 value for the reference CMS energy, $ecmRef$ is the reference energy scale set to 7000 GeV and $ecmPow$ is the energy rescaling pace. It is worth pointing out, as it is stated by the Pythia authors [75], this parameter value is also related to the settings of other parameters. Figure 6.9 shows the distributions generated using few arbitrary chosen values compared to the data.

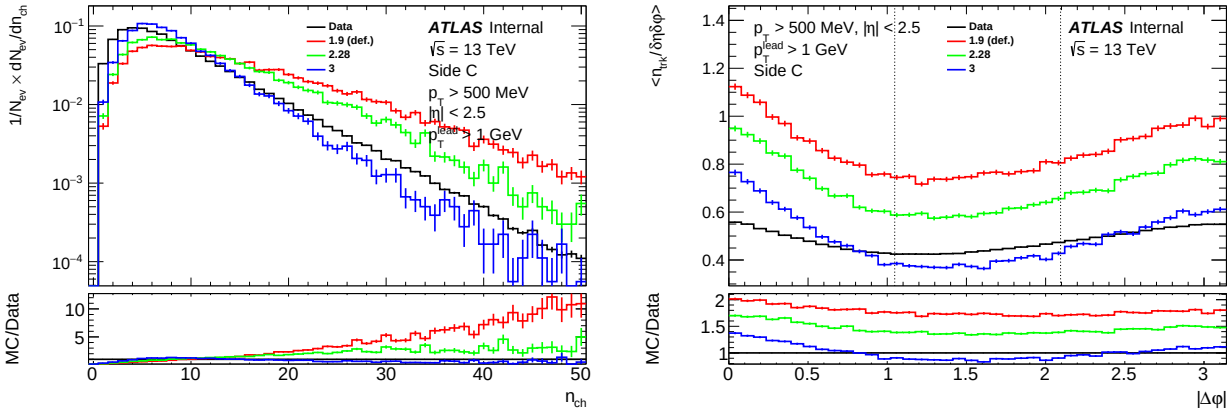

Figure 6.9: Comparison of the charged particle multiplicity (left) and the mean number of tracks as a function of $|\Delta\varphi|$ (right) for different MultipartonInteractions:pT0Ref values to the data.

The Monte Carlo description of the data improves with increasing value of the parameter. For MultipartonInteractions:pT0Ref > 3 GeV the changes seem to be minor. In case of the mean charged track multiplicity, the normalisation decreases with increasing value of the parameter. However, unlike for the previous parameters, the shapes of the distributions remain practically unchanged.

6.2 Parameter minimisation

The analysis described in the previous section suggests the selection of five parameters for the next part of the tuning procedure. These parameters are: **Diffraction:sigmaRefPomP**, **Diffraction:mPowPomP**, **Diffraction:mRefPomP**, **Diffraction:mRefPomP** and **MultipartonInteractions:pT0Ref**.

The first step is to identify the objective function. In the present analysis a χ^2 function was exploited. The $\langle n_{trk} \rangle$ vs $|\Delta\varphi|$ distribiution was taken as an input to the χ^2 calculation. Since it was shown that depending on the leading track transverse momentum, the shapes of the Monte Carlo and the data distributions evolve the minimisation procedure was performed for each of the three p_T^{lead} ranges. The χ^2 function is constructed as a sum over all bins in a given distribution:

$$\chi^2 = \sum_{i=1}^{40} \frac{(x_i^{MC} - x_i^{data})^2}{(e_i^{MC})^2 + (e_i^{data})^2}, \tag{6.3}$$

where x_i^{MC} and x_i^{data} are the i-th bin contents and e_i^{MC} and e_i^{data} are the errors on the i-th bin contents for the Monte Carlo and the data, respectively. Each distribution has 40 bins. The total χ^2 function value was then calculated as:

$$\chi^2_{tot} = \chi^2_{p_T^{lead}\in[1,2)} + \chi^2_{p_T^{lead}\in[2,4)} + \chi^2_{p_T^{lead}\in[4,+\infty)}. \tag{6.4}$$

The minimisation procedure starts with defining a parameter or rather a list of parameters as well as their allowed ranges. Then, each minimisation step is performed as follows:

1. Generate a sample of 100,000 Pythia events for a given set of parameters.
2. Analyse the sample using the common analysis code.
3. Calculate the χ^2 function value.

For each chosen parameter, a scan was performed. A number of samples was generated for the parameter values uniformly distributed within the allowed range, see Table 6.3.

Table 6.3: Parameters chosen in scan procedure.

Group	Name	Unit	Min. value	Max. value	# of samples
Diffraction	sigmaRefPomP	mb	10	40	100
Diffraction	mPowPomP	-	0	0.5	100
Diffraction	mMinPert	GeV	10	4000	160
Diffraction	mRefPomP	GeV	1	1000	100
MultipartonInteractions	pT0Ref	GeV	1.5	5	45

6.2.1 One-dimensional minimisation

This section discusses the scan results presented as plots of the χ^2 function value, divided by the number of the degrees of freedom $NDoF$, as a function of the considered parameter. Such plots are referred to as "χ^2 plots". A more detailed explanation is given in case of the Diffraction:sigmaRefPomP parameter, while for the others, only the final results are presented.

Diffraction:sigmaRefPomP:
Previous section suggests that the best value of Diffraction:sigmaRefPomP is close to 20 mb. It is worth checking if this is also the best choice for each p_T^{lead} ranges. Figure 6.10 shows the χ^2 plots for three p_T^{lead} bins.

For the lowest p_T^{lead} bin there seem to exist two distinct minima: the first one for Diffraction:sigmaRefPomP $\approx$ 26 mb, the second at $\sim$34 mb. For $p_T^{lead} \in [2, 4)$ there is a single minimum for Diffraction:sigmaRefPomP $\approx$ 20 mb. For the highest p_T^{lead} bin the minimum is located at $\sim$15 mb.

Eventually, the combined χ^2 value was obtained as a sum of individual values obtained for each p_T^{lead} bin and is presented in Figure 6.10. A single minimum for Diffraction:sigmaRefPomP $\approx$ 22 mb is observed in this figure. This value is close to the one obtained in the previous section. The hint of a local minimum is still visible for Diffraction:sigmaRefPomP $\approx$ 34 mb.

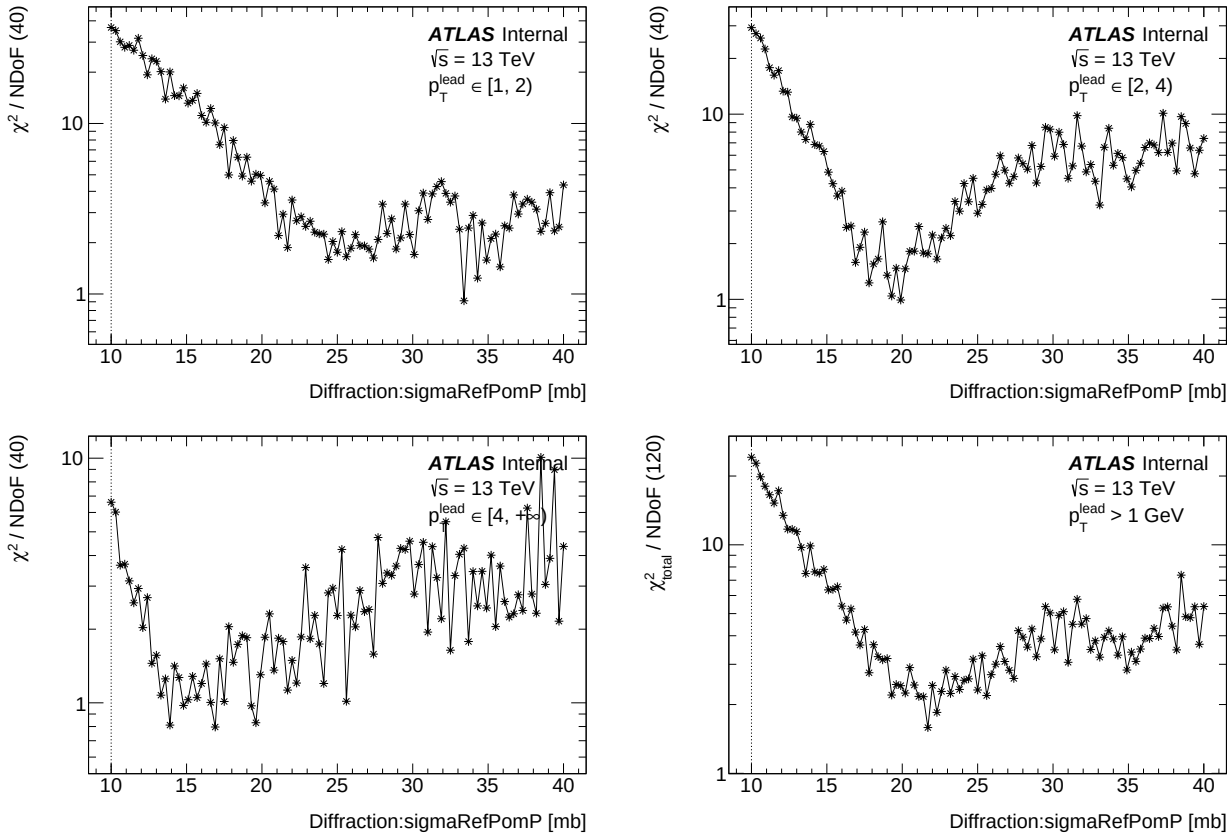

Figure 6.10: The χ^2 function value for different p_T^{lead} bins and the total χ^2 as a function of Diffraction:sigmaRefPomP parameter value. The vertical dotted line marks the parameter default value.

Diffraction:mPowPomP:
The results of the previous section suggests the value of 0.2. Figure 6.11 (left) shows the combined χ^2 plot, with a mimimum Diffraction:mPowPomP at ∼0.21.

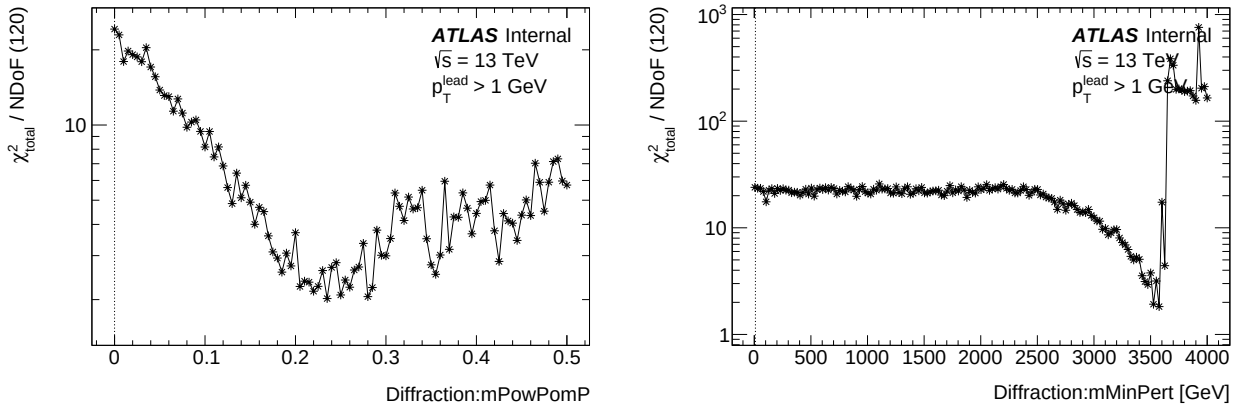

Figure 6.11: The χ^2 function value as a function of Diffraction:mPowPomP (left) and Diffraction:mMinPert (right) parameters value. The vertical dotted line marks the parameter default value.

Diffraction:mMinPert:
Section 6.1 findings suggest the value close to 3.5 TeV. The combined χ^2 is drawn in Figure 6.11 (right). For Diffraction:mMinPert < 2500 GeV the χ^2 does not depend on the parameter value. Above 2500 GeV rapid changes are visible, with the χ^2 minimum located within 3500 GeV–3600 GeV.

Diffraction:mRefPomP:
Figure 6.12 (left) shows the combined χ^2 plot implying the lack of sensitivity to the Diffraction:mRefPomP value. This confirms the observation of the previous section.

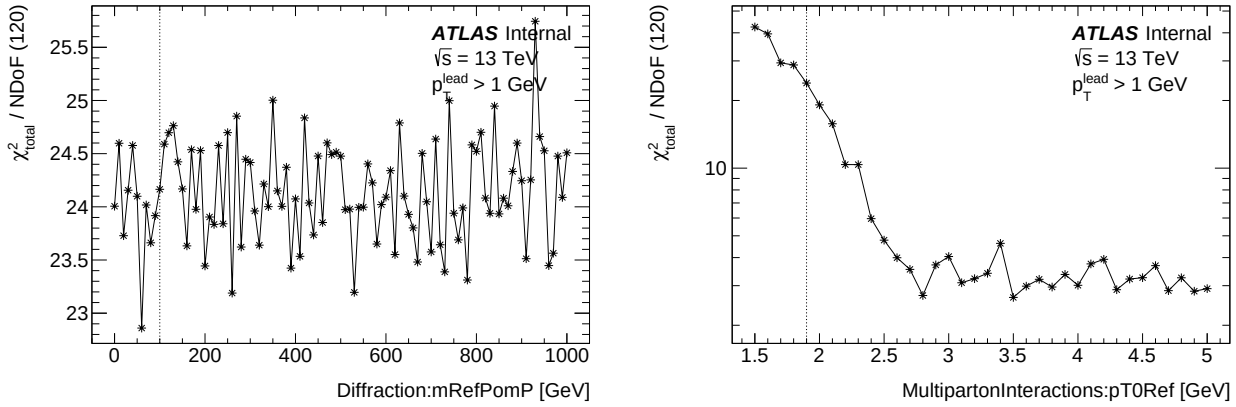

Figure 6.12: The χ^2 function value as a function of Diffraction:mRefPomP (left) and MultipartonInteractions:pT0Ref (right) parameter value. The vertical dotted line marks the parameter default value.

MultipartonInteractions:pT0Ref:
Section 6.1 results point to values between 2.28 and 3. The combined χ^2 plot is presented in Figure 6.12 (right).

For MultipartonInteractions:pT0Ref < 2.8 GeV the χ^2 rapidly decreases. Above, the χ^2 is the parameter value independent. No distinct minimum is observed. The parameter value of MultipartonInteractions:pT0Ref was set to 3.5 GeV, corresponding to the lowest χ^2 value.

Table 6.4 summarises the results of the above discussed scans.

Table 6.4: Values of the parameters obtained in the scan procedure.

Group	Name	Unit	Approx. minimum
Diffraction	sigmaRefPomP	mb	22
Diffraction	mPowPomP	-	0.21
Diffraction	mMinPert	GeV	3500
Diffraction	mRefPomP	GeV	Not found
MultipartonInteractions	pT0Ref	GeV	3.5

6.2.2 Correlations between parameters

In the next step of the minimization procedure, the scan was performed fixing one of the parameters at its minimum while scanning the others. Such a procedure was repeated for each of the considered parameters. Figure 6.13 shows the combined χ^2 plot for Diffraction:sigmaRefPomP parameter as an example.

As can be observed, the scans of the three considered parameters suggest the value of Diffraction:sigmaRefPomP close to $\sim$10 mb, which is close to the Pythia 8 A2 default value. This result and those obtained in Section 6.2.1 demonstrate the importance of the correlations between the parameters and clearly suggest a need for the multi-dimensional χ^2 minimization, i.e. a need of the multidimensional tuning.

6.3 Multi-parmeter fit

In the last step, a global fit using all five parameters was attempted. The minimization was performed using the `hyperopt` package [76] designed to serial and parallel optimization over various search spaces. This includes the ones showing a large variation of the results as a consequence of a small change of the input parameters. Table 6.5 lists the values of the parameters at the χ^2 minimum ($\chi^2/NDoF = 1.093$) and the data together with the fit results are presented in Fig. 6.14.

Table 6.5: Parameter values obtained with the `hyperopt` package.

Group	Name	Unit	Parameter value
Diffraction	sigmaRefPomP	mb	22.026
Diffraction	mPowPomP	-	0.0582
Diffraction	mMinPert	GeV	2876.648
Diffraction	mRefPomP	GeV	9.192
MultipartonInteractions	pT0Ref	GeV	1.533

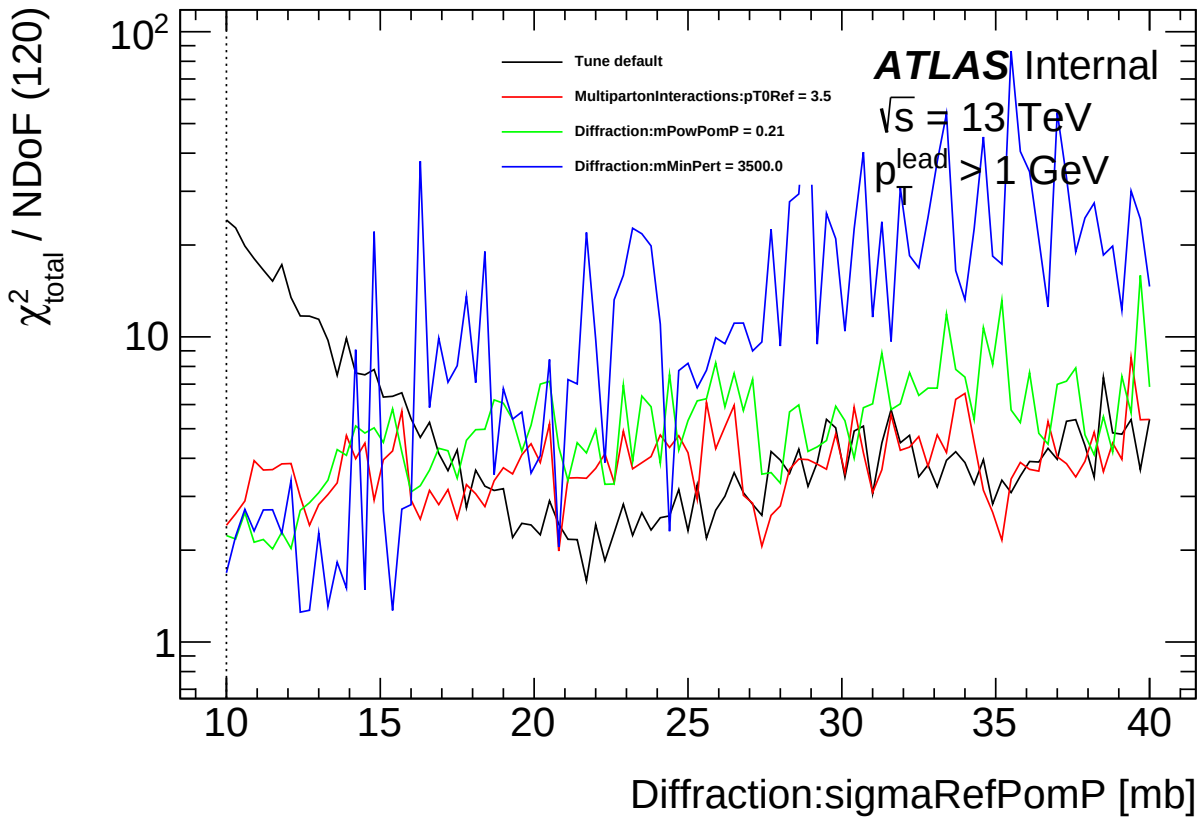

Figure 6.13: The χ^2 function value as a function of Diffraction:sigmaRefPomP parameter value with other parameters set at their respecitve minima. The black line represents the scan performed with other parameters set as in the default tune. The vertical dotted line marks the Diffraction:sigmaRefPomP default value.

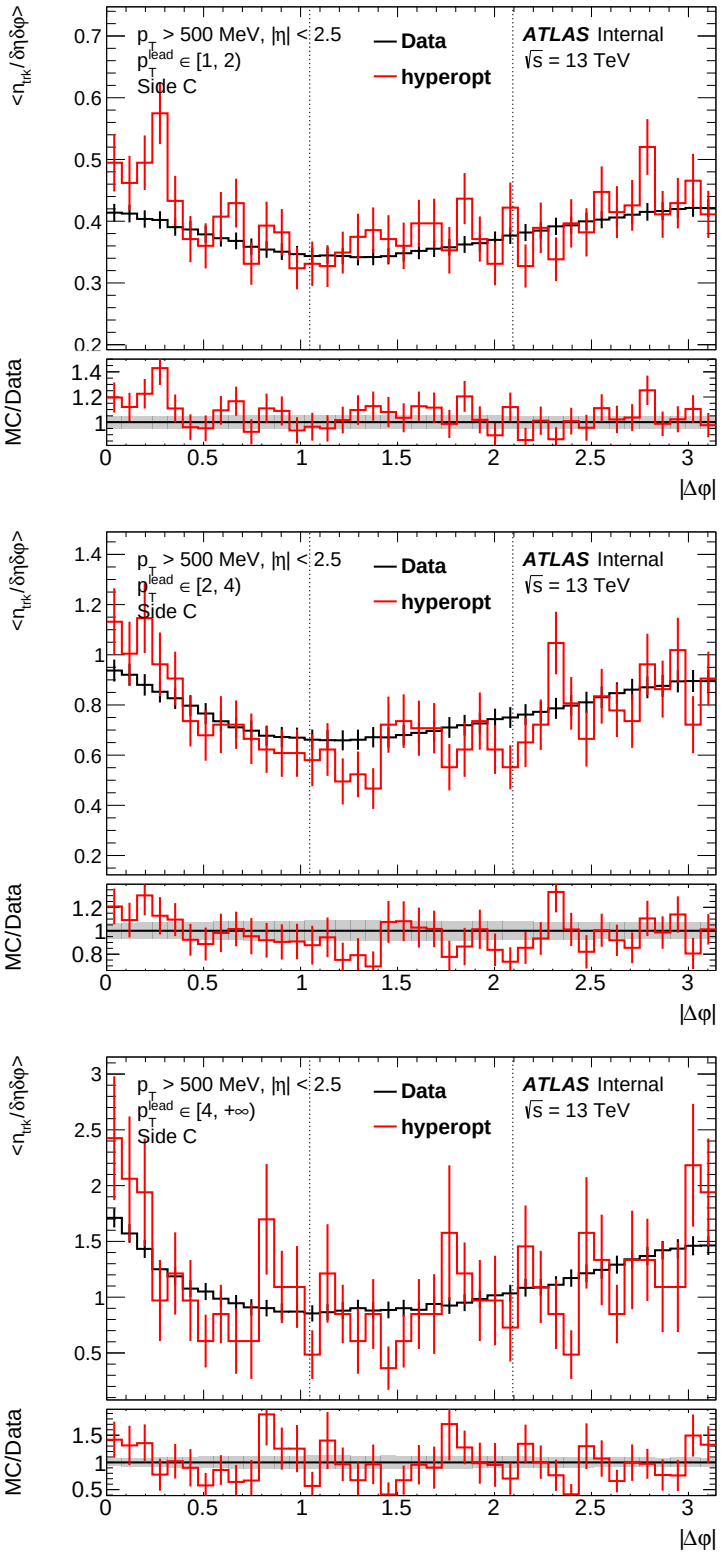

Figure 6.14: The data distributions (the black line) with results of the `hyperopt` fit (the red line) for different bins of p_T^{lead}.

Next, a sample of 2.5 million events was generated (and is referred to as "`hyperopt`"), with the parameters set to the above listed values. Then, the earlier discussed distributions were constructed and compared to the experimental results and Pythia 8 A2 SD predictions. The outcome of this comparison is presented in Figures 6.15 and 6.16.

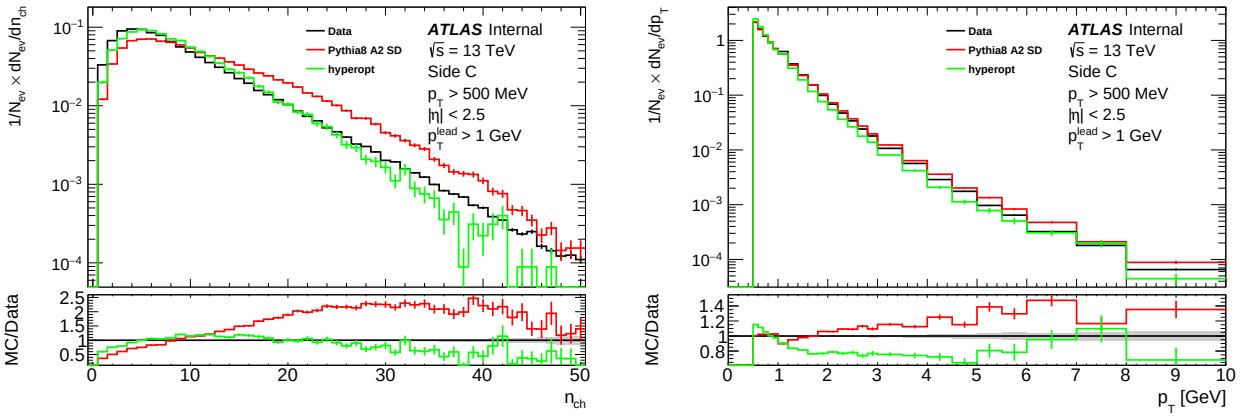

Figure 6.15: Distributions of the charged particle multiplicity n_{ch} (left) and the charged particle transverse momentum p_T (right) for events with the leading particle of the transverse momentum $p_{lead} > 1$ GeV. The black line – the data, the red line – Pythia 8 A2 SD, the green line - results of Pythia 8 SD tuning obtained with `hyperopt`.

In case of the charged particle multiplicity distribution the `hyperopt` predictions describe the experimental distribution much better than those of Pythia 8 A2 SD. Nevertheless, the very low and high multiplicities are still underestimated at the level reaching 50%. The charged particle transverse momentum distributions are shown in Fig. 6.15 right. The p_T distribution was not a part of the minimization procedure. The `hyperopt` spectrum is softer than the data and the Pythia 8 A2 SD predictions. Both the `hyperopt` sample and Pythia 8 A2 SD do not describe the data perfectly. For low p_T Pythia 8 A2 SD seems to describe the data slightly better than the `hyperopt` sample.

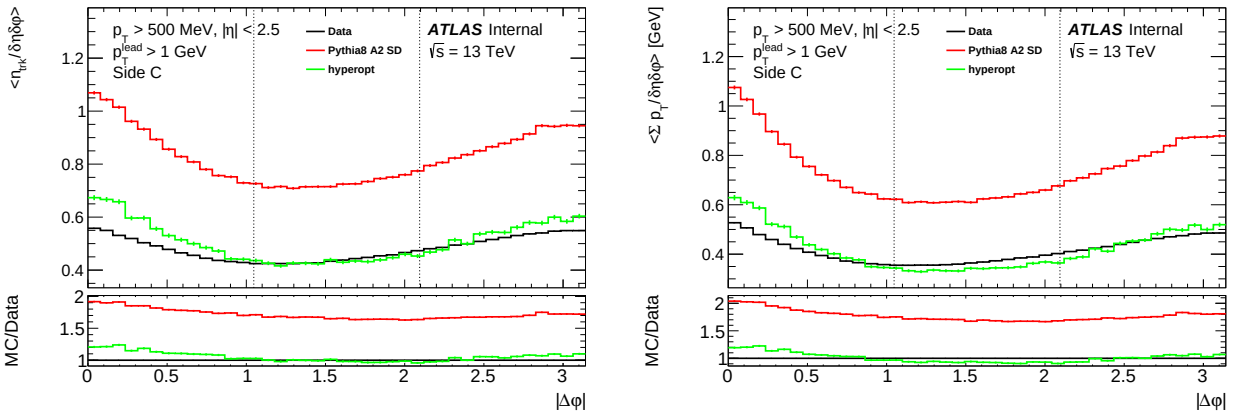

Figure 6.16: Distributions of the mean densities of the charged particle track multiplicity, $\langle n_{trk} \rangle$, (left) and the sum of transverse momenta, $\langle \Sigma p_T \rangle$, (right) as a function of $|\Delta\varphi|$ for events with the leading particle transverse momentum $p_{lead} > 1$ GeV. The vertical dotted lines mark boundaries of the three considered regions: towards, transverse and away. The black line – the data, the red line – Pythia 8 A2 SD, the green line – results of Pythia 8 SD tuning obtained with `hyperopt`.

For both $\langle n_{trk} \rangle$ and $\langle \Sigma p_T \rangle$ the `hyperopt` provides a better description of the measured distribution than Pythia 8 A2 SD. In case of $\langle n_{trk} \rangle$ the transverse region is well described by the `hyperopt` predictions. In the towards and away regions the `hyperopt` overestimates the data by about $\sim$20% and $\sim$10% respectively. In case of $\langle \Sigma p_T \rangle$ the agreement between the `hyperopt` and data is within 10% in the transverse and away regions, and in towards regions the `hyperopt` predictions overshoots the data by about 20%.

Summarising, an attempt of the Pythia 8 A2 SD Monte Carlo tuning was performed. For the first time, the procedure used the ATLAS data selected requesting the AFP proton tag, e.g. a sample enriched with single diffractive dissociation processes. The multidimensional tuning procedure provided a set of parameters resulting in a considerably better agreement of the experimental data and Monte Carlo predictions.

Chapter 7

Summary and conclusions

This thesis presented the study of the Underlying Event sensitive observables. The experimental basis for the work were the ATLAS Collaboration data collected during the dedicated proton-proton LHC run in 2017, which corresponds to the integrated luminosity of 56 nb^{-1}. The data were taken at $\sqrt{s} = 13$ TeV. The selection procedure followed the standard ATLAS one with an additional requirement of a tag of the forward scattered proton delivered by AFP. For the first time, the measurements of the Underlying Event sensitive observables were performed using the data sample enriched with single diffractive dissociation processes.

The studied observables were defined using the charged particle tracks measured in the Inner Detector. The tracks were requested to be within the pseudorapidity interval $|\eta| < 2.5$ and to have the transverse momentum greater than 0.5 GeV. The obtained results were corrected for the background contribution, detector effects and were unfolded to the particle level.

The analysis was performed in three regions of the azimuthal angle defined with respect to the highest transverse momentum particle. These were towards, transverse and away regions. For the study of the per-event observables, the transverse region was further split into transMax defined as the one containing larger activity and the complementary one – transMin. Predictions of the Pythia 8 A2 single diffractive Monte Carlo were confronted with the experimental results.

It was found that Pythia 8 A2 SD MC fails to reproduce the charged particle multiplicity. It predicts too many high multiplicity events and the shape of the MC distribution is much harder than the experimental one, showing approximately exponential decrease. On the other hand the MC predicted transverse momentum distribution of the charged particles quite well matches the measured one with a slight tendency of overestimating the high-p_T region.

The studied UE sensitive observables were the average number of the charged particle tracks, $\langle n_{trk} \rangle$, and the average value of the scalar sum of the transverse momenta, $\langle \Sigma p_T \rangle$. They were analysed as a function of the azimuthal distance from the leading particle, $|\Delta\varphi|$.

The shapes of the measured and predicted distributions qualitatively agree. The towards and away regions show higher activities than that seen in the transverse one. However, Pythia 8 A2 SD Monte Carlo overestimates both distributions in the whole $|\Delta\varphi|$ range. A study of $\langle n_{trk} \rangle$ and $\langle \Sigma p_T \rangle$ in different bins of the leading particle transverse momentum, p_T^{lead}, demonstrates that with increasing value of p_T^{lead}:

- activity in all regions increases,

- growth of the activity in the towards and away regions is faster than in the transverse one,
- the Pythia 8 A2 SD predictions approach the experimental distributions.

Such a behaviour clearly indicates the growing importance of hard processes with increasing value of the hard scale. The increase in the towards and away regions is a consequence of the emerging two-jet structure. The overall growth shows the increasing role of the radiation of additional gluon(s) leading to a more complex partonic structure of the event during the hadronisation processes.

Next step of the analysis was focused on the transverse, UE-dominated region. This region was on the event-by-event basis divided into the transMax and transMin regions, with the former being sensitive to the hard and MPI processes and the latter almost solely sensitive to the MPIs. The $\langle n_{trk} \rangle$ and $\langle \Sigma p_T \rangle$ distributions were measured as functions of p_T^{lead}. They show a characteristic shape with an initial rapid increase followed by a sort of a plateau. These distributions are relatively (within the errors) well reproduced by the used Monte Carlo model in the plateau region and largely overestimated for lower p_T^{lead} values. Such a conclusion can be extended to the transDiff (=transMax-transMin) distributions.

Some constraints on the Underlying Event phenomena can be also derived from a study of the per-event mean transverse momentum of charged particles, $\langle \text{mean } p_T \rangle$, as a function of n_{trk} or p_T^{lead}. Such analysis was performed for the transverse, transMax and transMin and transDiff regions. It has to be stressed that these are the only dependencies properly predicted by the Pythia 8 A2 single diffractive Monte Carlo.

Inadequate description of the measured distributions provided by the Pythia 8 A2 single diffractive Monte Carlo resulted an attempt to tune the model parameters. One should note that the distribution of the charged particle transverse momentum practically remains unchanged vs. the performed variations of the parameters' values. Dramatic effects were seen for distribution of the charged particle multiplicity and $\langle n_{trk} \rangle$. The latter was used in the final tuning fit. These comparisons allowed to select important parameters and to perform the fit. The resulting setting of the Pythia 8 A2 single diffractive model quite well reproduces the discussed experimental results.

The above findings clearly show a need for further analyses and studies concerning the tune of the Pythia 8 single diffractive model. Such investigations should be based on the enlarged data samples and they should include a wider set of observables. Eventually, they should also cover a common tuning of the parameters pertaining to the description of diffractive and non-diffractive processes, and should be based on the diffractive and inclusive data.

Appendix A

Additional information

Table A.1: Number of tracks after each cut and percentage of tracks which passed a given cut compared to previous one from sample triggered by the `HLT_noalg_L1AFP_A_OR_C` trigger.

Cut	# of tracks	% of tracks
All	67 124 984	100%
$p_T > 500\,\text{MeV}$	26 965 260	40.17%
$\lvert\eta\rvert < 2.5$	26 423 334	97.99%
$\lvert d_0\rvert < 1.5\,\text{mm}$	21 067 340	79.73%
Pixel hits ≥ 1	20 775 224	98.61%
SCT hits ≥ 6	19 085 774	91.87%

Table A.2: The number of events after each cut and the percentage of events which passed a given cut with respect to the previous one.

Cut	# of events	% of events
All	6 383 128	100%
`L1_AFP_C`	4 859 382	76.13%
1 vertex	2 693 824	55.44%
1 proton	2 563 717	95.17%
$0.035 < \xi < 0.080$	1 493 512	58.26%
# of tracks > 0	1 362 333	91.22%
# of tracks ≤ 50	1 361 866	99.97%
$p_T^{leading} > 1$ GeV	753 951	55.36%

Table showing number of event passed by each selection step.

Table A.3: The number of tracks after each cut and the percentage of tracks which passed a given cut with respect to the previous one.

Cut name	# of events	% of events
Initial	4859382	100%
1 vertex	2693824	55.44%
1 proton	2563712	95.17%
Proton ξ	1499258	58.48%
Tracks > 0	1367856	91.24%
Leading $p_T > 1$ GeV	758374	55.44%

Bibliography

[1] LHCb Collaboration. Observation of structure in the J/Ψ-pair mass spectrum. *Science Bulletin*, 65(23):1983–1993, 2020.

[2] R. Aaij, C. Abellán Beteta, B. Adeva, M. Adinolfi, C. A. Aidala, Z. Ajaltouni, S. Akar, P. Albicocco, J. Albrecht, F. Alessio, and et al. Observation of a Narrow Pentaquark State, Pc(4312)+, and of the Two-Peak Structure of the Pc(4450)+. *Physical Review Letters*, 122(22), Jun 2019.

[3] https://en.wikipedia.org/wiki/Standard_Model, Access: 02-12-2021.

[4] H. David Politzer. Reliable Perturbative Results for Strong Interactions? *Phys. Rev. Lett.*, 30:1346–1349, 1973.

[5] David J. Gross and Frank Wilczek. Ultraviolet Behavior of Nonabelian Gauge Theories. *Phys. Rev. Lett.*, 30:1343–1346, 1973.

[6] P.A. Zyla et al. Review of Particle Physics. *PTEP*, 2020(8):083C01, 2020.

[7] A. D. Martin, W. J. Stirling, R. S. Thorne, and G. Watt. Parton distributions for the LHC. *Eur. Phys. J. C*, 63:189, 2009.

[8] Torbjörn Sjöstrand, Stefan Ask, Jesper R. Christiansen, Richard Corke, Nishita Desai, Philip Ilten, Stephen Mrenna, Stefan Prestel, Christine O. Rasmussen, and Peter Z. Skands. An introduction to PYTHIA 8.2. *Comput. Phys. Commun.*, 191:159, 2015.

[9] ATLAS Collaboration. Measurement of the $W \to \ell\nu$ and $Z/\gamma^* \to \ell\ell$ production cross sections in proton–proton collisions at $\sqrt{s} = 7\,\text{TeV}$ with the ATLAS detector. *JHEP*, 12:060, 2010.

[10] Andy Buckley, Jonathan Butterworth, Stefan Gieseke, David Grellscheid, Stefan Höche, Hendrik Hoeth, Frank Krauss, Leif Lönnblad, Emily Nurse, Peter Richardson, Steffen Schumann, Michael H. Seymour, Torbjörn Sjöstrand, Peter Skands, and Bryan Webber. General-purpose event generators for lhc physics. *Physics Reports*, 504(5):145–233, 2011.

[11] Torbjörn Sjöstrand and Maria van Zijl. A multiple-interaction model for the event structure in hadron collisions. *Phys. Rev. D*, 36:2019–2041, Oct 1987.

[12] T Sjöstrand and P Skands. Multiple interactions and the structure of beam remnants. *Journal of High Energy Physics*, 2004(03):053–053, mar 2004.

[13] Torbjörn Sjöstrand. *The Development of MPI Modeling in Pythia*, chapter Chapter 10, pages 191–225.

[14] E. Eichten, I. Hinchliffe, K. Lane, and C. Quigg. Supercollider physics. *Rev. Mod. Phys.*, 56:579–707, Oct 1984.

[15] R.K. Ellis and J.C. Sexton. Qcd radiative corrections to parton-parton scattering. *Nuclear Physics B*, 269(2):445–484, 1986.

[16] T. Regge. Introduction to complex orbital momenta. *Nuovo Cim.*, 14:951, 1959.

[17] T. Regge. Bound states, shadow states and Mandelstam representation. *Nuovo Cim.*, 18:947–956, 1960.

[18] P. D. B. Collins. *An Instroduction to Regge Theory & High Energy Physics*. Cambrigde University Press, 1977.

[19] Bo Andersson, G. Gustafson, G. Ingelman, and T. Sjöstrand. Parton fragmentation and string dynamics. *Phys. Rept.*, 97:31–145, 1983.

[20] A. Donnachie and P. V. Landshoff. Elastic Scattering and Diffraction Dissociation. *Nucl. Phys. B*, 244:322, 1984.

[21] Gerhard A. Schuler and Torbjorn Sjostrand. Hadronic diffractive cross-sections and the rise of the total cross-section. *Phys. Rev. D*, 49:2257–2267, 1994.

[22] Lyndon Evans and Philip Bryant. LHC Machine. *JINST*, 3:S08001, 2008.

[23] Esma Mobs. The CERN accelerator complex - 2019. Complexe des accélérateurs du CERN - 2019. Jul 2019. General Photo.

[24] ATLAS Collaboration. The ATLAS Experiment at the CERN Large Hadron Collider. *JINST*, 3:S08003, 2008.

[25] CMS Collaboration. The CMS experiment at the CERN LHC. *JINST*, 3:S08004, 2008.

[26] The ALICE Collaboration. The ALICE experiment at the CERN LHC. *Journal of Instrumentation*, 3(08):S08002–S08002, aug 2008.

[27] The LHCb Collaboration. The LHCb detector at the LHC. *Journal of Instrumentation*, 3(08):S08005–S08005, aug 2008.

[28] Joao Pequenao. Computer generated image of the whole ATLAS detector. Mar 2008.

[29] ATLAS Collaboration. ATLAS Inner Detector: Technical Design Report, Volume 1. ATLAS-TDR-4; CERN-LHCC-97-016, 1997.

[30] ATLAS Collaboration. ATLAS Calorimeter Performance: Technical Design Report. ATLAS-TDR-1; CERN-LHCC-96-040, 1996.

[31] ATLAS Collaboration. ATLAS Tile Calorimeter: Technical Design Report. ATLAS-TDR-3; CERN-LHCC-96-042, 1996.

[32] ATLAS Collaboration. ATLAS Liquid Argon Calorimeter: Technical Design Report. ATLAS-TDR-2; CERN-LHCC-96-041, 1996.

[33] ATLAS Collaboration. ATLAS Muon Spectrometer: Technical Design Report. ATLAS-TDR-10; CERN-LHCC-97-022, CERN, 1997.

[34] ATLAS Collaboration. ATLAS Magnet System: Magnet Project Technical Design Report, Volume 1. ATLAS-TDR-6; CERN-LHCC-97-018, 1997.

[35] ATLAS Collaboration. ATLAS Central Solenoid: Magnet Project Technical Design Report, Volume 4. ATLAS-TDR-9; CERN-LHCC-97-021, CERN, 1997.

[36] ATLAS Collaboration. ATLAS Barrel Toroid: Magnet Project Technical Design Report, Volume 2. ATLAS-TDR-7; CERN-LHCC-97-019, 1997.

[37] ATLAS Collaboration. ATLAS Level-1 Trigger: Technical Design Report. ATLAS-TDR-12; CERN-LHCC-98-014, 1998.

[38] ATLAS Collaboration. ATLAS High-Level Trigger, Data Acquisition and Controls: Technical Design Report. ATLAS-TDR-16; CERN-LHCC-2003-022, 2003.

[39] https://tikz.net/wp-content/uploads/2021/09/axis3D_CMS-003.png, Access: 23-11-2021.

[40] Joao Pequenao. Computer generated image of the ATLAS inner detector. Mar 2008.

[41] ATLAS Collaboration. ATLAS Pixel Detector: Technical Design Report. ATLAS-TDR-11; CERN-LHCC-98-013, 1998.

[42] A. Abdesselam et al. The barrel modules of the atlas semiconductor tracker. *Nuclear Instruments and Methods in Physics Research Section A: Accelerators, Spectrometers, Detectors and Associated Equipment*, 568(2):642–671, 2006.

[43] A. Abdesselam et al. The atlas semiconductor tracker end-cap module. *Nuclear Instruments and Methods in Physics Research Section A: Accelerators, Spectrometers, Detectors and Associated Equipment*, 575(3):353–389, 2007.

[44] A. Ahmad et al. The silicon microstrip sensors of the atlas semiconductor tracker. *Nuclear Instruments and Methods in Physics Research Section A: Accelerators, Spectrometers, Detectors and Associated Equipment*, 578(1):98–118, 2007.

[45] The ATLAS TRT Collaboration. The ATLAS TRT Barrel Detector. *Journal of Instrumentation*, 3(02):P02014–P02014, feb 2008.

[46] The ATLAS TRT Collaboration. The ATLAS TRT end-cap detectors. *Journal of Instrumentation*, 3(10):P10003–P10003, oct 2008.

[47] A. Sidoti. Minimum Bias Trigger Scintillators in ATLAS Run II. Technical report, CERN, Geneva, Jun 2014.

[48] ATLAS Collaboration. ATLAS Forward Proton Phase-I Upgrade: Technical Design Report. ATLAS-TDR-024; CERN-LHCC-2015-009, 2015.

[49] J. Lange, L. Adamczyk, G. Avoni, E. Banas, A. Brandt, M. Bruschi, P. Buglewicz, E. Cavallaro, D. Caforio, G. Chiodini, L. Chytka, K. Cieśla, P.M. Davis, M. Dyndal, S. Grinstein, K. Janas, K. Jirakova, M. Kocian, K. Korcyl, I. Lopez Paz, D. Northacker, L. Nozka, M. Rijssenbeek, L. Seabra, R. Staszewski, P. Świerska, and T. Sykora. Beam tests of an integrated prototype of the ATLAS forward proton detector. *Journal of Instrumentation*, 11(09):P09005–P09005, sep 2016.

[50] K. Cerny. Performance of the AFP Time-of-Flight detector in 2017 LHC data. Aug 2020.

[51] M. Kocian. Readout and trigger for the afp detector at atlas experiment. *Journal of Instrumentation*, 12(1), 1 2017.

[52] D.A. Scannicchio. Atlas trigger and data acquisition: Capabilities and commissioning. *Nuclear Instruments and Methods in Physics Research Section A: Accelerators, Spectrometers, Detectors and Associated Equipment*, 617(1):306–309, 2010. 11th Pisa Meeting on Advanced Detectors.

[53] A. Kazarov. The ATLAS Data Flow System for LHC Run II. Technical report, CERN, Geneva, Dec 2015.

[54] ATLAS Collaboration. ATLAS Computing: Technical Design Report. ATLAS-TDR-17; CERN-LHCC-2005-022, 2005.

[55] B. Dehning. Beam Loss Monitors at LHC. In *2014 Joint International Accelerator School: Beam Loss and Accelerator Protection*, pages 303–318, 2016.

[56] ATLAS Collaboration. Observation and Measurement of Forward Proton Scattering in Association with Lepton Pairs Produced via the Photon Fusion Mechanism at ATLAS. *Phys. Rev. Lett.*, 125:261801, 2020.

[57] R. Staszewski and J. Chwastowski. Transport Simulation and Diffractive Event Reconstruction at the LHC. *Nucl. Instrum. Meth. A*, 609:136–141, 2009.

[58] L. Deniau (editor), H. Grote, G. Roy and F. Schmidt. Mad-X User's Guide.

[59] M. Trzebiński. Machine Optics Studies for the LHC Measurements. *Proc. SPIE Int. Soc. Opt. Eng.*, 9290:929026, 2014.

[60] ATLAS Collaboration. Further ATLAS tunes of Pythia 6 and Pythia 8. ATL-PHYS-PUB-2011-014, 2011.

[61] ATLAS Collaboration. Athena, May 2021.

[62] Rene Brun and Fons Rademakers. Root – an object oriented data analysis framework. *Nucl. Instrum. Meth. A*, 389(1):81 – 86, 1997.

[63] ATLAS Collaboration. Measurement of charged-particle distributions sensitive to the underlying event in $\sqrt{s} = 13$ TeV proton-proton collisions with the ATLAS detector at the LHC. *JHEP*, 03:157, 2017.

[64] S. Czekierda. *Hadronic final states in diffractive pp scattering at* $\sqrt{s} = 13$ *TeV using the ATLAS detector*. PhD thesis, IFJ PAN, http://rifj.ifj.edu.pl/handle/item/299, 2019.

[65] ATLAS Collaboration. Charged-particle distributions in $\sqrt{s} = 13\,\text{TeV}$ pp interactions measured with the ATLAS detector at the LHC. *Phys. Lett. B*, 758:67, 2016.

[66] F. James and M. Roos. Minuit: A System for Function Minimization and Analysis of the Parameter Errors and Correlations. *Comput. Phys. Commun.*, 10:343–367, 1975.

[67] Giulio D'Agostini. A multidimensional unfolding method based on Bayes' theorem. *Nucl. Instrum. Meth. A*, 362(2):487 – 498, 1995.

[68] R. Brandelik et al. Evidence for Planar Events in e^+e^- Annihilation at High-Energies. *Phys. Lett. B*, 86:243–249, 1979.

[69] C. Berger et al. Evidence for Gluon Bremsstrahlung in e^+e^- Annihilations at High-Energies. *Phys. Lett. B*, 86:418–425, 1979.

[70] W. Bartel et al. Observation of Planar Three Jet Events in e^+e^- Annihilation and Evidence for Gluon Bremsstrahlung. *Phys. Lett. B*, 91:142–147, 1980.

[71] Peter Skands, Stefano Carrazza, and Juan Rojo. Tuning PYTHIA 8.1: the Monash 2013 Tune. *Eur. Phys. J. C*, 74(8):3024, 2014.

[72] R. Ciesielski and K. Goulianos. MBR Monte Carlo Simulation in PYTHIA8, 2012.

[73] A. Aktas, V. Andreev, T. Anthonis, B. Antunovic, S. Aplin, A. Asmone, A. Astvatsatourov, A. Babaev, S. Backovic, and et al. Measurement and qcd analysis of the diffractive deep-inelastic scattering cross section at hera. *The European Physical Journal C*, 48(3):715–748, Oct 2006.

[74] A. Aktas, V. Andreev, T. Anthonis, B. Antunovic, S. Aplin, A. Asmone, A. Astvatsatourov, A. Babaev, S. Backovic, and et al. Diffractive deep-inelastic scattering with a leading proton at hera. *The European Physical Journal C*, 48(3):749–766, Oct 2006.

[75] https://pythia.org/manuals/pythia8306/Welcome.html, Access: 02-12-2021.

[76] James Bergstra, Daniel Yamins, and David Cox. Making a science of model search: Hyperparameter optimization in hundreds of dimensions for vision architectures. In Sanjoy Dasgupta and David McAllester, editors, *Proceedings of the 30th International Conference on Machine Learning*, volume 28 of *Proceedings of Machine Learning Research*, pages 115–123, Atlanta, Georgia, USA, 17–19 Jun 2013. PMLR.